VIBRATION REDUCTION OF HELICOPTER TAIL SHAFT BY USING DRY FRICTION DAMPERS

A THESIS SUBMITED TO
THE GRADUATE SCHOOL OF NATURAL AND APPLIED SCIENCES
OF
MIDDLE EAST TECHNICAL UNIVERSITY

BY

ONUR ÖZAYDIN

IN PARTIAL FULFILLMENT OF THE REQUIREMENTS
FOR
THE DEGREE OF MASTER OF SCIENCE
IN
MECHANICAL ENGINEERING

SEPTEMBER 2017

Approval of the thesis

VIBRATION REDUCTION OF HELICOPTER TAIL SHAFT BY USING DRY FRICTION DAMPERS

submitted by **ONUR ÖZAYDIN** in partial fulfillment of the requirements for the degree of **Master of Science in Mechanical Engineering Department, Middle East Technical University** by,

Prof. Dr. Gülbin Dural Ünver
Dean, Graduate School of **Natural and Applied Sciences** _____

Prof. Dr. M. A. Sahir Arıkan
Head of Department, **Mechanical Engineering** _____

Assoc. Prof. Dr. Ender Ciğeroğlu
Supervisor, **Mechanical Engineering Dept., METU** _____

Examining Committee Members:

Prof. Dr. F. Suat Kadıoğlu
Mechanical Engineering Dept., METU _____

Assoc. Prof. Dr. Ender Ciğeroğlu
Mechanical Engineering Dept., METU _____

Assoc. Prof. Dr. Yiğit Yazıcıoğlu
Mechanical Engineering Dept., METU _____

Assoc. Prof. Dr. S. Çağlar Başlamışlı
Mechanical Engineering Dept., Hacettepe University _____

Assist. Prof. Dr. Gökhan O. Özgen
Mechanical Engineering Dept., METU _____

Date: 27.09.2017

I hereby declare that all information in this document has been obtained and presented in accordance with academic rules and ethical conduct. I also declare that, as required by these rules and conduct, I have fully cited and referenced all material and results that are not original to this work.

Name, Last name : Onur ÖZAYDIN

Signature :

ABSTRACT

VIBRATION REDUCTION OF HELICOPTER TAIL SHAFT BY USING DRY FRICTION DAMPERS

Özaydın, Onur
M.S., Department of Mechanical Engineering
Supervisor: Assoc. Prof. Dr. Ender Ciğeroğlu

September 2017, 108 pages

Tail Drive Shaft is a power transmission component of a helicopter which constructs the link between the main gearbox and the tail rotor. In many helicopter designs, tail shafts are working in supercritical speeds. In order to limit resonance vibrations of tail drive shaft occurring as a drawback of a supercritical design, dry friction dampers are used by helicopter manufacturers. In this study, vibration reduction of supercritical helicopter tail drive shaft by utilizing dry friction dampers is studied. Euler-Bernoulli beam theory is used to model the tail drive shaft supported by springs at both ends which represent the bearings and couplings used. Equation of motion is obtained by using Hamilton's Principle. Obtained partial differential equation of motion is discretized by using Galerkin's Method, and Harmonic Balance Method utilizing single harmonic is used in order to convert the resulting nonlinear ordinary differential equations into a set of nonlinear algebraic equations. These set of equations are solved by using Newton's Method and Newton's Method with Arc-Length Continuation. In order to model the dry friction dampers

mathematically, two different friction models are taken from the literature. However, in the literature there is no mathematical model for dry friction element with gap. Therefore, in this study as an addition to the models taken from the literature a one-dimensional macroslip dry friction model with gap is developed. Several case studies are performed in order to study the effect of design parameters on the vibration amplitude of the tail drive shaft.

Keywords: Helicopter tail drive shaft, dry friction damper, macroslip friction model, nonlinear vibrations, harmonic balance method

ÖZ

HELİKOPTER KUYRUK ŞAFTI TİTREŞİMLERİNİN KURU SÜRTÜNMELİ SÖNÜMLEYİCİLER KULLANARAK AZALTILMASI

Özaydın, Onur
Yüksek Lisans, Makina Mühendisliği Bölümü
Tez Yöneticisi: Doç. Dr. Ender Ciğeroğlu

Eylül 2017, 108 sayfa

Kuyruk şaftı helikopterlerde ana dişli kutusu ile kuyruk rotoru arasındaki bağlantıyı sağlayan güç aktarım organıdır. Birçok helikopter tasarımında ,kuyruk şaftları kritik hızın üzerindeki hızlarda çalışmaktadır. Kritik hızın üzerinde çalışmaktan kaynaklı oluşan rezonans titreşimlerini sınırlayabilmek için helikopter üreticileri kuru sürtünmeli sönümleyicileri kullanmaktadır. Bu çalışmada, kuru sürtünmeli sönümleyiciler kullanarak kritik hızın üzerinde çalışan kuyruk şaftlarının titreşimlerinin azaltılması çalışılmıştır. Rulmanları ve kaplinleri temsil eden yaylar tarafından iki ucundan desteklenen kuyruk şaftı Euler-Bernoulli kiriş teorisi kullanılarak modellenmiştir. Hareket denklemi Hamilton Prensibi kullanılarak elde edilmiştir. Elde edilen kısmi diferansiyel hareket denklemi Galerkin Metodu vasıtası ile ayrıklaştırılmıştır ve ortaya çıkan doğrusal olmayan adi diferansiyel denklemler tek harmonikli Harmonik Denge Metodu vasıtası ile doğrusal olmayan cebirsel denklem setine dönüştürülmüştür. Elde edilen doğrusal olmayan cebirsel denklem seti Newton Metodu ve Yay Uzunluğu Sürekliliği kullanan Newton Metodu vasıtası

ile çözülmüştür. Kuru sürtünmeli sönümleyicileri matematiksel olarak modelleyebilmek için literatiürden iki farklı model alınmıştır. Ancak literatürde boşluk içeren kuru sürtünme elemanları için herhangi bir matematiksel model bulunmamaktadır. Bu yüzden bu çalışmada literatürden alınan modellere ek olarak tek boyutlu boşluklu makro kayma sürtünme modeli geliştirilmiştir. Tasarım parametrelerinin kuyruk şaftı titreşimi üzerindeki etkisini görmek için çeşitli vaka incelemeleri yapılmıştır.

Anahtar Kelimeler: Helikopter kuyruk şaftı, kuru sürtünmeli sönümleyici, makro kayma sürtünme modeli, doğrusal olmayan titreşimler, harmonik denge metodu

To My Parents Ünal and Seher

And

My Sister Ceren

To My Grandpa

ACKNOWLEDGEMENTS

I would like to send my thanks to my supervisor Assoc. Prof. Dr. Ender CİĞEROĞLU for his support throughout my graduate years in METU.

I want to express my gratitude to my parents Ünal and Seher ÖZAYDIN for their endless support and continuous encouragement. They devote their lives to their kids.

I want to thank to my sister Ceren ÖZAYDIN who follows a similar path with his brother for her endless support.

Finally, I want to thank to my manager Dr. Zihni Burçay Sarıbay in TAI and my colleagues Mustafa Özgür Aydoğan and Şiar Deniz Yavuz for their support.

TABLE OF CONTENTS

LIST OF TABLES

TABLES

LIST OF FIGURES

FIGURES

CHAPTER 1

INTRODUCTION AND LITERATURE SURVEY

1.1 Introduction

Helicopter tail drive shaft is an important power transmission component, excessive vibrations of which may lead to catastrophic failures. In helicopter industry, two different designs for tail drive shafts are used: subcritical design (operating below the first natural frequency) and supercritical design (operating above the first natural frequency). Instead of using many short shafts working at subcritical speed, using minimum number of long shafts working at supercritical speed is more advantageous. However, in the supercritical design, during startup and shutdown shafts pass through at least one critical frequency. This may cause failure of the shaft due to excessive vibrations caused by the resonance phenomenon as a result of unbalance present in the system. This type of failure can be avoided by using proper dry friction dampers (Dzygadlo & Perkowski, 2002; Ozaydin & Cigeroglu, 2017; Prasue et al., 1967).

In the studies aiming to examine the dynamic response of structures including dry friction, two main approaches are used, the macroslip and the microslip methods. Macroslip method in which the interface is modeled as rigid body, is used for the friction interfaces which are assumed to have point contact. In this method only stick, slip and separation states are observed. It is impossible to have partial slip. This method can only be used for interfaces having small normal load acting on it because it is the only way where gross-slip occurs at the friction interface. Unlike the macroslip method, in microslip method, friction interface is modeled as elastic

body and if the normal load acting on the interface is high enough, it is possible to observe partial slip. Macroslip method is studied in large scale because it is mathematically simple. Unlike the macroslip method, microslip methods are not covered much, because of their complex mathematical structure.

Although there are many studies in the literature that considers the application of dry friction dampers as a vibration reduction device, studies on the reduction of helicopter tail shaft vibration are very limited. Due to this lack of information in the helicopter industry, data used in the selection of the dry friction dampers are obtained from the experimental studies which are expensive. Therefore in this study, a continuous dynamic model of a helicopter tail drive shaft with dry friction damper attached on it is developed. Euler-Bernoulli beam model is used in order to model the shaft because of the long and slender structure of the helicopter tail shaft. Equation of motion is derived by using Hamilton's Principle. Galerkin's Method with multiple trial functions is used to be able to discretize the partial differential equation of motion. It is complicated to analyze the systems including dry friction because of the nonlinear behavior of the dry friction. Harmonic Balance Method (HBM) which is a frequency domain based solution method and in which Fourier series approximation is used in order to represent the nonlinear forces, is a widely used method in the literature instead of direct time integration, which costs high computational effort and computation time. Therefore, in this study, the resulting nonlinear ordinary differential equations are converted into a set of nonlinear algebraic equations by using HBM. Newton's Method and Newton's Method with Arc-Length Continuation are used to be able to solve the resulting nonlinear equations. In order to model the dry friction dampers mathematically, two different friction models, one dimensional macroslip friction model with constant normal load and two dimensional macroslip friction model with constant normal load, are taken from the literature. However, in the literature there is no mathematical model for the friction interfaces with gap. Therefore, in this study as an addition to the models taken from the literature a one-dimensional macroslip friction model with gap is developed. General conditions for stick, slip and contact and no contact states

are developed and transition angles for simple harmonic motion are obtained analytically. In order to see the effects of dry friction damper on the response of tail drive shaft system, several case studies are performed.

1.2 Literature Survey

Supercritical shafts are used in different applications, especially having long drivelines like tilt rotors and helicopters. In his study (Prasue et al., 1967) shows the advantageous of using supercritical shafts in helicopter drivelines. (Ozaydin & Cigeroglu, 2017) developed a mathematical model of the helicopter tail shaft and examine the vibrations by adding dry friction damper. Additional studies are performed on the dynamics of supercritical shafts by many researchers (Darlow & Zorzi, 1978; Desmidt, 2009; Dzygadlo & Perkowski, 2000; Montagnier & Hochard, 2007).

Excessive vibration is an important problem for rotating shafts. Reduction of these vibrations can be achieved by using external damping elements. Effect of external damping on the vibration of flexible shafts are studied by (Dostal et al., 1977). Squeeze film dampers and hydrodynamic bearings are widely used in turbines but they are complex and costly. Rotating systems on viscoelastic supports are studied by (Dutt & Nakra, 1996; Lee et al., 2004; Montagnier & Hochard, 2014). Damping of rotor conical whirl by using dry friction is studied by (Sorge, 2009). (Peng et al., 2017) attached smart spring supports to shafts to suppress the bending vibrations by using dry friction. (Bradfield et al., 2016) used electromagnetic bearing in order to control the vibrations of a supercritical shaft. (Dzygadlo & Perkowski, 2002; Ozaydin & Cigeroglu, 2017) studied the usage of dry friction dampers on supercritical helicopter tail shafts.

Dry friction dampers are chosen as a solution to resonant vibrations and they are widely used in different applications such as turbomachinery (Yang & Menq, 1998b, 1998c), turbine or compressor blades (Cigeroglu et al., 2007; Cigeroglu & Ozguven, 2006; Ferri et al., 1998; Koh et al., 2005; Sanliturk et al., 2001), buildings under seismic excitation (Belash, 2015; Erisen & Cigeroglu, 2012; Mualla & Belev, 2002; Tabeshpour & Ebrahimmian, 2010), and railway bogies (Kaiser et al., 2002; Taylor et al., 2014; True & Asmund, 2002). Successful results of the studies (Srinivasan & Cutts, 1983) on effectiveness of dry friction dampers draw attention of the researchers.

Simple macroslip models are studied by many researchers in which normal load is assumed to be constant and relative motion is one-dimensional (Al Sayed et al., 2011; Andersson et al., 2007; Cameron et al., 1990; Den Hartog, 1930; Ding & Chen, 2008; Dowell & Schwartz, 1983; Ferri, 1995; Griffin, 1980; Liao et al., 2014; Menq & Griffin, 1985; Srinivasan & Cutts, 1983; Wang & Chen, 1993). In order to solve the forced response of the friction interfaces having two-dimensional relative motion with constant normal load, two dimensional friction models were developed. (Griffin & Menq, 1991; Menq et al., 1991; Menq & Yang, 1998; Sanliturk & Ewins, 1996). Apart from the systems with constant normal load, there is a possibility of normal load variation and separation if there is a normal component of the relative motion to the contact plane. In order to study these kind of systems, new models are developed. One-dimensional friction model with variable normal load is studied by (Cigeroglu et al., 2009; Menq et al., 1986; Petrov & Ewins, 2004; Siewert et al., 2009; B. Yang et al., 1998; Yang & Menq, 1998b, 1998c; Zucca et al., 2012).

Three-dimensional contact motion is studied by (Chen & Menq, 2001; Yang & Menq, 1998a). Apart from the macroslip models, because of the complex mathematical structure limited number of studies are done about the microslip models (Cigeroglu et al., 2007; Cigeroglu et al., 2006, 2007; Csaba, 1998; Filippi et al., 2004; He et al., 2010; Koh et al., 2005; Menq et al., 1986a, 1986b, 1986c; Putignano et al., 2011; Quinn & Segalman, 2005).

Harmonic Balance Method is a widely used method in order to convert nonlinear ordinary differential equation set into a set of nonlinear algebraic equations. In HBM method both single harmonic (Ferri & Bindemann, 1992; Liao et al., 2014; Ostachowicz, 1990; Sanliturk et al., 1997, 2001; Whiteman & Ferri, 1996) and multi harmonic representation are used (Chen et al., 2000; Ferri & Dowell, 1988; Kuran & Özgüven, 1996; Petrov & Ewins, 2003; Pierre et al., 1985; Von Groll & Ewins, 2001) in the literature.

CHAPTER 2

MATHEMATICAL MODEL

The tail drive shaft system shown in Fig.1 consists of a shaft supported by two bearings at both ends and connected to two couplings. A dry friction damper is used on the shaft in order to decrease vibration amplitudes. Spring elements are used to represent the bearings and couplings.

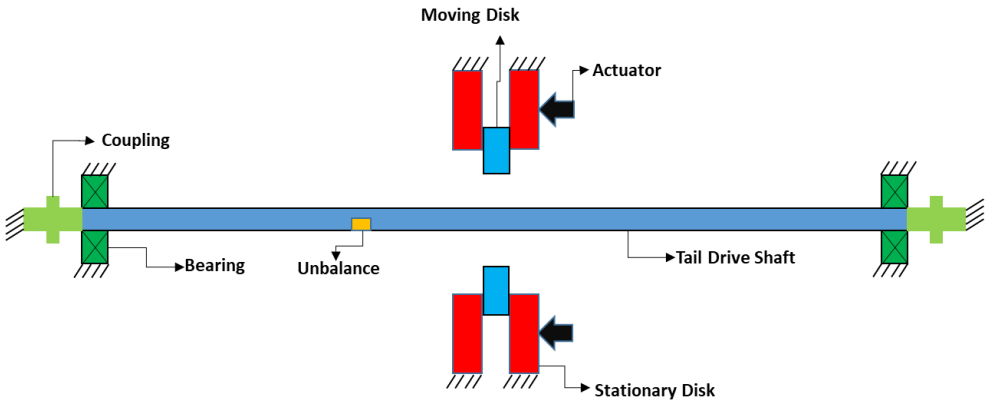

Fig.1 Tail drive shaft system

Modelling of a helicopter tail shaft starts with the selection of proper beam model. Because of the long and slender structure of the tail shafts Euler-Bernoulli beam theory is chosen. It is assumed that the cross-section of the beam is symmetric and bending takes place in plane of symmetry (Bauchau & Craig, 2009). In order to find the equation of motion (EOM) of the beam, Hamilton's Principle, which is an energy based method, is used. This method can be formulated as;

$$\int_{t_1}^{t_2}\left(\delta T-\delta U+\delta W_v\right)\mathrm{d}t=0\,, \tag{2.1}$$

where T is kinetic energy, U is the potential energy and W_v is virtual work done by non-conservative forces, δ is the symbol of variation.

$$\delta T=\frac{\rho A_c}{2}\int_0^L\delta\left(\left(\frac{\partial w_z}{\partial t}\right)^2+\left(\frac{\partial w_y}{\partial t}\right)^2\right)dx\,, \tag{2.2}$$

$$\delta U=\frac{EI}{2}\int_0^L\delta\left(\left(\frac{\partial^2 w_z}{\partial x^2}\right)^2+\left(\frac{\partial^2 w_y}{\partial x^2}\right)^2\right)dx\,, \tag{2.3}$$

$$\begin{aligned}\delta W_v=&\int_0^L\left(c\frac{\partial w_z(x,t)}{\partial t}\delta w_z(x,t)+c\frac{\partial w_y(x,t)}{\partial t}\delta w_y(x,t)\right)dx\\&+\int_0^L\left(f_{nz}\left(w_z(x,t)\right)\delta w_z(x,t)+f_{ny}\left(w_y(x,t)\right)\delta w_y(x,t)\right)\delta_{kd}\left(x-L_d\right)dx\,,\\&-\int_0^L\left(f_z(\mathrm{t})\delta w_z(x,t)+f_y(\mathrm{t})\delta w_y(x,t)\right)\delta_{kd}\left(x-L_f\right)dx\end{aligned} \tag{2.4}$$

where w_z and w_y are transverse displacements, ρ is density, A_c is cross sectional area, E is Young's Modulus, I is moment of inertia, c is viscous damping coefficient, $f_{nz}\left(w_z(x,t)\right)$ and $f_{ny}\left(w_y(x,t)\right)$ are the nonlinear friction forces, $f_z(t)$ and $f_y(t)$ are external forcings, L_d is the location of dry friction damper, L_f is the location of external forcing and δ_{kd} is Kronecker Delta.

Insert Eq.(2.2), Eq.(2.3) and Eq.(2.4) into Eq.(2.1);

$$\frac{\rho A_c}{2}\int_{t_1}^{t_2}\int_0^L \delta\left(\left(\frac{\partial w_z}{\partial t}\right)^2+\left(\frac{\partial w_y}{\partial t}\right)^2\right)dxdt-\frac{EI}{2}\int_{t_1}^{t_2}\int_0^L \delta\left(\left(\frac{\partial^2 w_z}{\partial x^2}\right)^2+\left(\frac{\partial^2 w_y}{\partial x^2}\right)^2\right)dxdt$$
$$+\int_{t_1}^{t_2}\int_0^L\left(c\frac{\partial w_z(x,t)}{\partial t}\delta w_z(x,t)+c\frac{\partial w_y(x,t)}{\partial t}\delta w_y(x,t)\right)dxdt$$
$$+\int_{t_1}^{t_2}\int_0^L\left(f_{nz}\left(w_z(x,t)\right)\delta w_z(x,t)+f_{ny}\left(w_y(x,t)\right)\delta w_y(x,t)\right)\delta_{kd}\left(x-L_d\right)dxdt \quad . (2.5)$$
$$-\int_{t_1}^{t_2}\int_0^L\left(f_z(\mathrm{t})\delta w_z(x,t)+f_y(\mathrm{t})\delta w_y(x,t)\right)\delta_{kd}\left(x-L_f\right)dxdt=0$$

Kinetic energy part of the Eq.(2.5) can be written as;

$$\rho A_c\int_{t_1}^{t_2}\int_0^L\left(\frac{\partial w_z}{\partial t}\right)\left(\frac{\partial \delta w_z}{\partial t}\right)dxdt+\rho A_c\int_{t_1}^{t_2}\int_0^L\left(\frac{\partial w_y}{\partial t}\right)\left(\frac{\partial \delta w_y}{\partial t}\right)dxdt\,. \qquad (2.6)$$

After applying integration by parts (IBP) to Eq.(2.6), it can be written as;

$$\rho A_c\int_0^L\left(\left(\frac{\partial w_z}{\partial t}\delta w_z\right)_{t_1}^{t_2}-\int_{t_1}^{t_2}\delta w_z\frac{\partial^2 w_z}{\partial t^2}dt\right)dx+\rho A_c\int_0^L\left(\left(\frac{\partial w_y}{\partial t}\delta w_y\right)_{t_1}^{t_2}-\int_{t_1}^{t_2}\delta w_y\frac{\partial^2 w_y}{\partial t^2}dt\right)dx, \quad (2.7)$$

where

$$\left(\frac{\partial w_z}{\partial t}\delta w_z\right)_{t_1}^{t_2}=0, \qquad (2.8)$$

$$\left(\frac{\partial w_y}{\partial t}\delta w_y\right)_{t_1}^{t_2}=0\,. \qquad (2.9)$$

Eq.(2.7) can be simplified as;

$$-\rho A_c\int_0^L\int_{t_1}^{t_2}\delta w_z\frac{\partial^2 w_z}{\partial t^2}dtdx-\rho A_c\int_0^L\int_{t_1}^{t_2}\delta w_y\frac{\partial^2 w_y}{\partial t^2}dtdx\,. \qquad (2.10)$$

Potential energy part of the Eq.(2.5) can be written as;

$$EI\int_{t_1}^{t_2}\int_0^L\left(\frac{\partial^2 w_z}{\partial x^2}\right)\left(\frac{\partial^2 \delta w_z}{\partial x^2}\right)dxdt+EI\int_{t_1}^{t_2}\int_0^L\left(\frac{\partial^2 w_y}{\partial x^2}\right)\left(\frac{\partial^2 \delta w_y}{\partial x^2}\right)dxdt\,. \qquad (2.11)$$

After applying integration by parts to Eq.(2.11), it can be written as;

$$\begin{aligned}&\int_{t_1}^{t_2}\left(\left(\frac{\partial^2 w_z}{\partial x^2}\frac{\partial \delta w_z}{\partial x}\right)_0^L-\int_0^L\frac{\partial \delta w_z}{\partial x}\frac{\partial^3 w_z}{\partial x^3}dx\right)dt\\&+EI\int_{t_1}^{t_2}\left(\left(\frac{\partial^2 w_y}{\partial x^2}\frac{\partial \delta w_y}{\partial x}\right)_0^L-\int_0^L\frac{\partial \delta w_y}{\partial x}\frac{\partial^3 w_y}{\partial x^3}dx\right)dt\end{aligned}. \tag{2.12}$$

Apply integration by parts once more to Eq.(2.12) and it can be written as;

$$\begin{aligned}&EI\int_{t_1}^{t_2}\left(\left(\frac{\partial^2 w_z}{\partial x^2}\frac{\partial \delta w_z}{\partial x}\right)_0^L-\left(\frac{\partial^3 w_z}{\partial x^3}\delta w_z\right)_0^L+\int_0^L\delta w_z\frac{\partial^4 w_z}{\partial x^4}dx\right)dt\\&+EI\int_{t_1}^{t_2}\left(\left(\frac{\partial^2 w_y}{\partial x^2}\frac{\partial \delta w_y}{\partial x}\right)_0^L-\left(\frac{\partial^3 w_y}{\partial x^3}\delta w_y\right)_0^L+\int_0^L\delta w_y\frac{\partial^4 w_y}{\partial x^4}dx\right)dt\end{aligned}. \tag{2.13}$$

EOM is finalized by combining the Eq.(2.10) and Eq.(2.13) and virtual work part of Eq.(2.5).

$$\begin{aligned}&-\rho A_c\int_{t_1}^{t_2}\int_0^L\delta w_z\frac{\partial^2 w_z}{\partial t^2}dxdt-\rho A_c\int_{t_1}^{t_2}\int_0^L\delta w_y\frac{\partial^2 w_y}{\partial t^2}dxdt\\&-EI\int_{t_1}^{t_2}\left(\left(\frac{\partial^2 w_z}{\partial x^2}\frac{\partial \delta w_z}{\partial x}\right)_0^L-\left(\frac{\partial^3 w_z}{\partial x^3}\delta w_z\right)_0^L+\int_0^L\delta w_z\frac{\partial^4 w_z}{\partial x^4}dx\right)dt\\&-EI\int_{t_1}^{t_2}\left(\left(\frac{\partial^2 w_y}{\partial x^2}\frac{\partial \delta w_y}{\partial x}\right)_0^L-\left(\frac{\partial^3 w_y}{\partial x^3}\delta w_y\right)_0^L+\int_0^L\delta w_y\frac{\partial^4 w_y}{\partial x^4}dx\right)dt\\&+\int_{t_1}^{t_2}\int_0^L\left(c\frac{\partial w_z(x,t)}{\partial t}\delta w_z(x,t)+c\frac{\partial w_y(x,t)}{\partial t}\delta w_y(x,t)\right)dxdt\\&+\int_{t_1}^{t_2}\int_0^L\left(f_{nz}\left(w_z(x,t)\right)\delta w_z(x,t)+f_{ny}\left(w_y(x,t)\right)\delta w_y(x,t)\right)\delta_{kd}(x-L_d)dxdt\\&-\int_{t_1}^{t_2}\int_0^L\left(f_z(\mathrm{t})\delta w_z(x,t)+f_y(\mathrm{t})\delta w_y(x,t)\right)\delta_{kd}(x-L_f)dxdt=0\end{aligned}. \tag{2.14}$$

Below four equations are the boundary conditions;

$$EI\left(\frac{\partial^3 w_z}{\partial x^3}\delta w_z\right)_0^L = 0\,, \tag{2.15}$$

$$EI\left(\frac{\partial^3 w_y}{\partial x^3}\delta w_y\right)_0^L = 0\,, \tag{2.16}$$

$$EI\left(\frac{\partial^2 w_z}{\partial x^2}\frac{\partial \delta w_z}{\partial x}\right)_0^L = 0\,, \tag{2.17}$$

$$EI\left(\frac{\partial^2 w_y}{\partial x^2}\frac{\partial \delta w_y}{\partial x}\right)_0^L = 0\,. \tag{2.18}$$

Eq.(2.15) and Eq.(2.16) states that either shear force or displacement is zero. Eq.(2.17) and Eq.(2.18) states that either moment or slope is zero. These are the four boundary conditions of free-free Euler Bernoulli beam. Finally Eq.(2.14) is simplified to;

$$\begin{aligned}&\rho A_c \frac{\partial^2 w_z(x,t)}{\partial t^2} + EI\frac{\partial^4 w_z(x,t)}{\partial x^4} + c\frac{\partial w_z(x,t)}{\partial t}\\ &= f_z(\mathrm{t})\delta_{kd}\left(x-L_f\right) - f_{nz}\left(w_z(x,t)\right)\delta_{kd}\left(x-L_d\right)\end{aligned}\,, \tag{2.19}$$

$$\begin{aligned}&\rho A_c \frac{\partial^2 w_y(x,t)}{\partial t^2} + EI\frac{\partial^4 w_y(x,t)}{\partial x^4} + c\frac{\partial w_y(x,t)}{\partial t}\\ &= f_y(\mathrm{t})\delta_{kd}\left(x-L_f\right) - f_{ny}\left(w_y(x,t)\right)\delta_{kd}\left(x-L_d\right)\end{aligned}\,. \tag{2.20}$$

These equation of motions do not contain the linear and torsional springs attached on the shaft. They will be added to the solution by using trial functions.

For the solution of the partial differential equation of motions given in Eq.(2.19) and Eq.(2.20) Galerkin's Method is used. Utilizing expansion theorem, transverse displacements of the shaft can be expressed as given below;

$$w_z(x,t) = \sum_{j=1}^{n_m} q_j(t)\phi_j(x), \tag{2.21}$$

$$w_y(x,t)=\sum_{j=1}^{n_m} r_j(t)\phi_j(x), \tag{2.22}$$

where $q_j(t)$ and $r_j(t)$ are the j^{th} generalized coordinates and ϕ_j(x) is mass normalized eigenfunction of a beam supported by springs at both ends and n_m is the number of eigenfunctions used in the expansion. Before proceeding forward, eigenfunctions are found by using the procedure given below.

Eq.(2.19) excluding damping and forcing terms and transverse displacement $w(x,t)$ are written as;

$$EI\frac{\partial^4 w_z}{\partial y^4}=-\rho A_c\frac{\partial^2 w_z}{\partial t^2}, \tag{2.23}$$

$$w_z(\mathrm{x},\mathrm{t})=W(\mathrm{x})\mathrm{F}(\mathrm{t}). \tag{2.24}$$

Insert Eq.(2.24) into Eq.(2.23);

$$EI\frac{\partial^4 W(x)\mathrm{F}(\mathrm{t})}{\partial x^4}=-\rho A_c\frac{\partial^2 W(x)\mathrm{F}(\mathrm{t})}{\partial t^2}, \tag{2.25}$$

$$\frac{EI}{\rho A_c W(\mathrm{x})}\frac{\partial^4 W(\mathrm{x})}{\partial x^4}=-\frac{\partial^2 \mathrm{F}(t)}{\partial t^2}\frac{1}{\mathrm{F}(t)}=-\lambda, \tag{2.26}$$

$$EI\frac{\partial^4 W(\mathrm{x})}{\partial x^4}-\omega^2\rho A_c W(\mathrm{x})=0. \tag{2.27}$$

Solution of the this kind of ordinary differential equation (ODE) is;

$$W(\mathrm{x})=\mathrm{C}_1\sin(\beta x)+\mathrm{C}_2\cos(\beta x)+\mathrm{C}_3\sinh(\beta x)+\mathrm{C}_4\cosh(\beta x). \tag{2.28}$$

Four boundary conditions of beam with linear and torsional springs on the corners are;

$$-EI\frac{d^3W(x)}{dx^3}\Big|_{x=0}-kW(x)\Big|_{x=0}=0, \tag{2.29}$$

$$EI\frac{d^2W(x)}{dx^2}\Big|_{x=0} - k_t\frac{dW(x)}{dx}\Big|_{x=0} = 0, \tag{2.30}$$

$$EI\frac{d^3W(x)}{dx^3}\Big|_{x=L} - kW(x)\Big|_{x=L} = 0, \tag{2.31}$$

$$EI\frac{d^2W(x)}{dx^2}\Big|_{x=L} + k_t\frac{dW(x)}{dx}\Big|_{x=L} = 0, \tag{2.32}$$

where k and k_t are the linear and torsional stiffness values of the springs attached on the corners. After inserting Eq.(2.28) into Eq.(2.29), Eq.(2.30), Eq.(2.31) and Eq.(2.32) ,four equations are obtained;

$$EI\beta^3C_1 - kC_2 - EI\beta^3C_3 - kC_4 = 0, \tag{2.33}$$

$$-k_t\beta C_1 - EI\beta^2C_2 - k_t\beta C_3 + EI\beta^2C_4 = 0, \tag{2.34}$$

$$\begin{aligned}&\left(\mathrm{k}\sin(\beta L) + \mathrm{EI}\,\beta^3\cos(\beta L)\right)C_1\\ &+\left(\mathrm{k}\cos(\beta L) - \mathrm{EI}\,\beta^3\sin(\beta L)\right)C_2\\ &+\left(\mathrm{k}\sinh(\beta L) - \mathrm{EI}\,\beta^3\cosh(\beta L)\right)C_3\\ &+\left(\mathrm{k}\cosh(\beta L) - \mathrm{EI}\,\beta^3\sinh(\beta L)\right)C_4 = 0\end{aligned}, \tag{2.35}$$

$$\begin{aligned}&\left(\mathrm{k}_t\,\beta\cos(\beta L) - \mathrm{EI}\,\beta^2\sin(\beta L)\right)C_1\\ &+\left(-\mathrm{k}_t\,\beta\sin(\beta L) - \mathrm{EI}\,\beta^2\cos(\beta L)\right)C_2\\ &+\left(\mathrm{k}_t\,\beta\cosh(\beta L) + \mathrm{EI}\,\beta^2\sinh(\beta L)\right)C_3\\ &+\left(\mathrm{k}_t\,\beta\sinh(\beta L) + \mathrm{EI}\,\beta^2\cosh(\beta L)\right)C_4 = 0\end{aligned}. \tag{2.36}$$

Eq.(2.33), Eq.(2.34), Eq.(2.35) and Eq.(2.36) can be written in matrix format as;

$$\begin{bmatrix} D_1 & D_2 \\ D_3 & D_4 \end{bmatrix}\begin{Bmatrix} C_1 \\ C_2 \\ C_3 \\ C_4 \end{Bmatrix} = 0, \tag{2.37}$$

where

$$D_1 = \begin{bmatrix} EI\beta^3 & -k \\ -k_t\beta & -EI\beta^2 \end{bmatrix}, \tag{2.38}$$

$$D_2 = \begin{bmatrix} -EI\beta^3 & -k \\ -k_t\beta & EI\beta^2 \end{bmatrix}, \tag{2.39}$$

$$D_3 = \begin{bmatrix} (\mathrm{ksin}(\beta L) + \mathrm{EI}\,\beta^3\cos(\beta L)) & (\mathrm{kcos}(\beta L) - \mathrm{EI}\,\beta^3\sin(\beta L)) \\ (\mathrm{k}_t\,\beta\cos(\beta L) - \mathrm{EI}\,\beta^2\sin(\beta L)) & (-\mathrm{k}_t\,\beta\sin(\beta L) - \mathrm{EI}\,\beta^2\cos(\beta L)) \end{bmatrix}, \tag{2.40}$$

$$D_4 = \begin{bmatrix} (\mathrm{ksinh}(\beta L) - \mathrm{EI}\,\beta^3\cosh(\beta L)) & (\mathrm{kcosh}(\beta L) - \mathrm{EI}\,\beta^3\sinh(\beta L)) \\ (\mathrm{k}_t\,\beta\cosh(\beta L) + \mathrm{EI}\,\beta^2\sinh(\beta L)) & (\mathrm{k}_t\,\beta\sinh(\beta L) + \mathrm{EI}\,\beta^2\cosh(\beta L)) \end{bmatrix}. \tag{2.41}$$

β values are found by making the determinant of the Eq.(2.37) zero as given below;

$$\left\| \begin{bmatrix} D_1 & D_2 \\ D_3 & D_4 \end{bmatrix} \right\| = 0\,. \tag{2.42}$$

After finding β values by using Eq.(2.37) $C_1, C_2,$ C_3 and C_4 are found. It is important to note that rank of the matrix in Eq.(2.37) is three not four and because of that three constants are found in terms of the remaining constant.

After finding trial functions Eq.(2.21) and Eq.(2.22) are inserted into Eq.(2.19) and Eq.(2.20), in order to discretize the system.

$$\begin{aligned} &\rho A_c \sum_{j=1}^{n_m} \frac{d^2 q_j(t)}{dt^2}\phi_j(x) + EI\sum_{j=1}^{n_m} q_j \frac{d^4\phi_j(x)}{dx^4}(t) + c\sum_{j=1}^{n_m}\frac{dq_j(t)}{dt}\phi_j(x) \\ &+ f_{nz}(t)\delta(x - L_d) = f_z(t)\delta(x - L_f) \end{aligned}, \tag{2.43}$$

$$\begin{aligned} &\rho A_c \sum_{j=1}^{n_m} \frac{d^2 r_j(t)}{dt^2}\phi_j(x) + EI\sum_{j=1}^{n_m} r_j(t) \frac{d^4\phi_j(x)}{dx^4} + c\sum_{j=1}^{n_m}\frac{dr_j(t)}{dt}\phi_j(x) \\ &+ f_{ny}(t)\delta(x - L_d) = f_y(t)\delta(x - L_f) \end{aligned}. \tag{2.44}$$

Multiply both sides of the Eq.(2.43) and Eq.(2.44) by $\phi_i(\mathrm{x})$ and integrate over the spatial domain.

$$\int_0^L \left(\begin{array}{l} \rho A_c \sum_{j=1}^{n_m} \frac{d^2 q_j(t)}{dt^2} \phi_j(x)\phi_i(x) + EI \sum_{j=1}^{n_m} q_j(t) \frac{d^4 \phi_j(x)}{dx^4} \phi_i(x) \\ + c \sum_{j=1}^{n_m} \frac{dq_j(t)}{dt} \phi_j(x)\phi_i(x) + f_{nz}(t)\delta(x - L_d)\phi_i(x) \end{array} \right) dx \quad , \quad (2.45)$$
$$= \int_0^L \left(f_z(t)\delta(x - L_f)\phi_i(x) \right) dx$$

$$\int_0^L \left(\begin{array}{l} \rho A_c \sum_{j=1}^{n_m} \frac{d^2 r_j(t)}{dt^2} \phi_j(x)\phi_i(x) + EI \sum_{j=1}^{n_m} r_j(t) \frac{d^4 \phi_j(x)}{dx^4} \phi_i(x) \\ + c \sum_{j=1}^{n_m} \frac{dr_j(t)}{dt} \phi_j(x)\phi_i(x) + f_{ny}(t)\delta(x - L_d)\phi_i(x) \end{array} \right) dx \quad . \quad (2.46)$$
$$= \int_0^L \left(f_y(t)\delta(x - L_f)\phi_i(x) \right) dx$$

Eq.(2.45) and Eq.(2.46) can be written in matrix format as;

$$[I]\{\ddot{q}\} + [C_r]\{\dot{q}\} + [\Omega]\{q\} + \{F_{nz}(\{q\})\} = \{F_z(t)\}, \quad (2.47)$$

$$[I]\{\ddot{r}\} + [C_r]\{\dot{r}\} + [\Omega]\{r\} + \{F_{ny}(\{r\})\} = \{F_y(t)\}. \quad (2.48)$$

Eq.(2.47) and Eq.(2.48) can be combined as follows;

$$\begin{bmatrix} [I] & 0 \\ 0 & [I] \end{bmatrix} \begin{Bmatrix} \{\ddot{q}\} \\ \{\ddot{r}\} \end{Bmatrix} + \begin{bmatrix} [C_r] & 0 \\ 0 & [C_r] \end{bmatrix} \begin{Bmatrix} \{\dot{q}\} \\ \{\dot{r}\} \end{Bmatrix} + \begin{bmatrix} [\Omega] & 0 \\ 0 & [\Omega] \end{bmatrix} \begin{Bmatrix} \{q\} \\ \{r\} \end{Bmatrix}$$
$$+ \begin{Bmatrix} \{F_{nz}(\{q\})\} \\ \{F_{ny}(\{r\})\} \end{Bmatrix} = \begin{Bmatrix} \{F_z(t)\} \\ \{F_y(t)\} \end{Bmatrix} \quad . \quad (2.49)$$

Since mass normalized eigenfunctions are used in the expansion, $[I]$, $[C_r]$ and $[\Omega]$ are $n_m \times n_m$ identity matrix, diagonal damping matrix, diagonal matrix of squares of natural frequencies, respectively. $\{F_{nz}\}$, $\{F_{ny}\}$ are nonlinear modal forcing vectors and $\{F_z\}$, $\{F_y\}$ are external modal forcing vectors. Elements of these matrices and vectors can be calculated as follows;

$$\Omega_{ii} = \omega_i^2 = \int_0^L EI \frac{d^4\phi_i(x)}{dx^4}\phi_i(x)\,dx\,, \tag{2.50}$$

$$C_{r_{ii}} = \int_0^L c\phi_i(x)^2 dx = 2\zeta_i\omega_i, \tag{2.51}$$

$$F_{nz_i}(\{q\},t) = f_{nz}(\{q\},t)\phi_i(L_d), \tag{2.52}$$

$$F_{ny_i}(\{r\},t) = f_{ny}(\{r\},t)\phi_i(L_d), \tag{2.53}$$

$$F_{z_i}(t) = f_z(t)\phi_i(L_f), \tag{2.54}$$

$$F_{y_i}(t) = f_y(t)\phi_i(L_f), \tag{2.55}$$

where ω_i and ζ_i are the natural frequency and damping ratio of the i^{th} mode.

CHAPTER 3

DRY FRICTION MODELS

3.1 One Dimensional Macroslip Friction Model with Constant Normal Load

In this part a simple macroslip model in which normal load is assumed to be constant and relative motion is one dimensional, is studied. Illustration of the studied model is given Fig. 2.

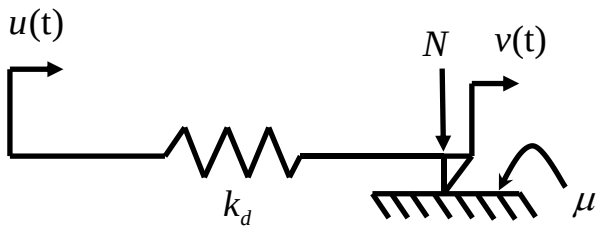

Fig. 2 Dry friction element

Here, k_d is the tangential contact stiffness, N is the normal load, μ is coefficient of friction, $u(t)$ is the tangential input motion and $v(t)$ is the slip motion.

Interfaces represented by using one dimensional macroslip friction model can be in two different states; stick and slip. When the interface is in stick state, the force on the spring can be represented as;

$$f_n = k_d(\mathrm{u}-\mathrm{v}). \tag{3.1}$$

If the interface is in slip state, the force on the spring is constant and it is represented as;

$$f_n = \pm \mu N \,. \tag{3.2}$$

When the interface comes to the instant of slip to stick transition, both Eq.(3.1) and Eq.(3.2) are satisfied. Differentiating these two equations

$$\frac{df_n}{dt} = k_d \left(\frac{du}{dt} - \frac{dv}{dt} \right),$$

(3.3)

$$\frac{df_n}{dt} = 0 \,. \tag{3.4}$$

Inserting Eq.(3.4) into Eq.(3.3)

$$k_d \left(\dot{u} - \dot{v} \right) = 0 \,, \tag{3.5}$$

$$\dot{u} = \dot{v} \,. \tag{3.6}$$

From Eq.(3.6) it can be stated that for one dimensional macroslip friction model, slip-to-stick transition occurs when the input motion reverses its direction.

Whenever the friction force reaches to its limiting values, stick-to-slip transition occurs. In slip state $u - v$ is constant and the friction interface moves with $\dot{u}$. By using Eq.(3.1) and Eq.(3.2) the relation can be written as

$$f_n = k_d \left(u - v \right) = \pm \mu N \,, \tag{3.7}$$

$$f_n = k_d \left(u - u_0 \right) + f_0 = \pm \mu N \,, \tag{3.8}$$

where u_0 and f_0 are the displacement and friction force at the beginning of stick state.

For single harmonic relative motion, input motion $u(t)$ can be written as

$$u(t) = A\sin(\theta), \tag{3.9}$$

In order to find the slip-to-stick transition angles, differentiate Eq.(3.9)

$$\dot{u} = A\omega\cos(\theta) = 0. \tag{3.10}$$

From Eq.(3.10) two different angles, $\theta = \frac{\pi}{2}$ and $\theta = \frac{3\pi}{2}$, where relative input motion changes its sign and slip-to-stick transition occurs are found.

For stick to negative slip transition;

$$u_0 = u\left(\frac{\pi}{2}\right) = A, \tag{3.11}$$

$$f_0 = \mu N. \tag{3.12}$$

Insert Eq.(3.11) and Eq.(3.12) into Eq.(3.8);

$$k_d\left(A\sin\theta^* - A\right) + \mu N = -\mu N, \tag{3.13}$$

$$\theta^* = \pi - a\sin\left(1 - \frac{2\mu N}{k_d A}\right). \tag{3.14}$$

For stick to positive slip transition;

$$u_0 = u\left(\frac{3\pi}{2}\right) = -A, \tag{3.15}$$

$$f_0 = -\mu N. \tag{3.16}$$

Insert Eq.(3.15) and Eq.(3.16) into Eq.(3.8)

$$k_d\left(A\sin\theta^{**} + A\right) - \mu N = +\mu N, \tag{3.17}$$

$$\theta^{**} = 2\pi - a\sin\left(1 - \frac{2\mu N}{k_d A}\right) = \theta^* + \pi. \tag{3.18}$$

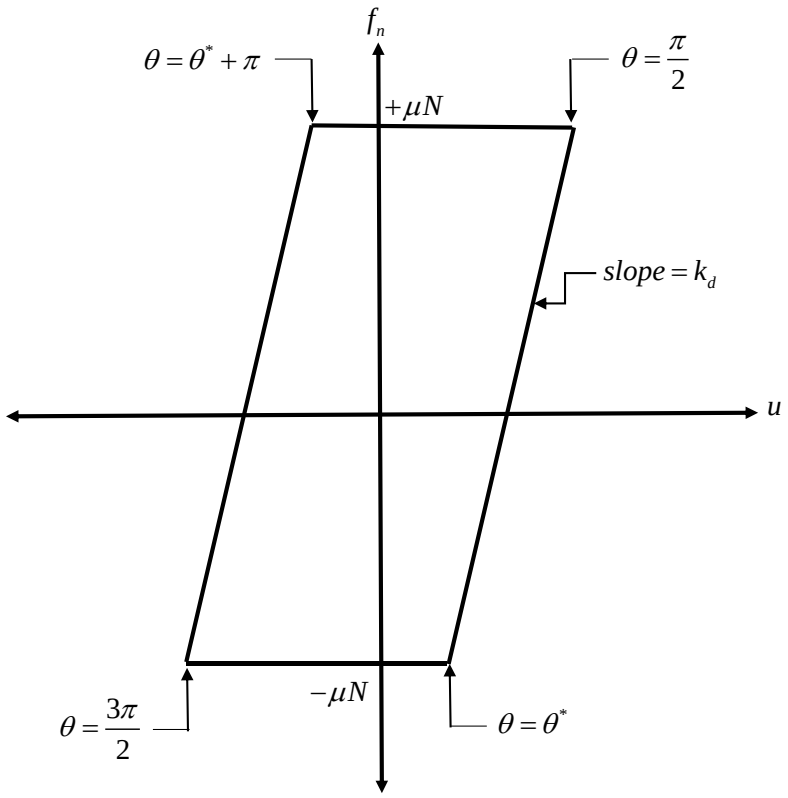

Fig. 3 Hysteresis curve for single harmonic motion

By using the obtained data hysteresis curve given in Fig. 3 can be drawn and it can be represented mathematically as given below;

$$f_n = \begin{cases} k_d\left(A\sin\left(\theta\right) - A\right) + \mu N \text{ when } \dfrac{\pi}{2} \le \theta \le \theta^* \\ -\mu N \text{ when } \theta^* \le \theta \le \dfrac{3\pi}{2} \\ k_d\left(A\sin(\theta) + A\right) - \mu N \text{ when } \dfrac{3\pi}{2} \le \theta \le \theta^* + \pi \\ \mu N \text{ when } \theta^* + \pi \le \theta \le \dfrac{5\pi}{2} \end{cases} . \qquad (3.19)$$

In the steady-state hysteresis curve given in Fig. 3, horizontal lines are representing the slip state, while lines with non-zero slope are representing the stick state. First

motion of the dry friction interface starts with stick state and continue in this state until the point where the friction force reaches to its limiting value and stick to slip transition occurs. Slip state continues with constant friction force and the state of friction changes from slip to stick when the relative input motion changes its direction. As experienced before, stick state continues until the friction force reaches to its limiting value and interface follows this pattern until reaching to steady-state. Two main parameters affecting the amount of stick and slip states are μ and N. In Fig. 4 three different hysteresis curves are given with small, average and high μN (slip force) values. It can be said that for the curve with high μN stick state is dominant and for the curve with small μN slip state is dominant. The effect of these states are examined in case studies.

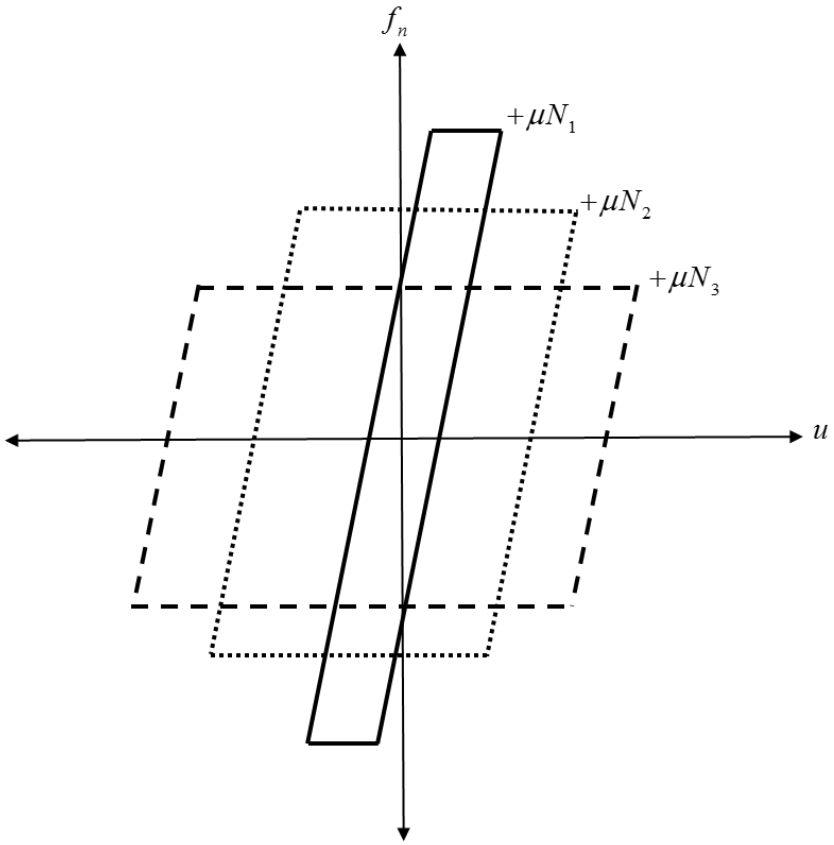

Fig. 4 Hysteresis curves with different slip force values where $\mu N_1 > \mu N_2 > \mu N_3$

The nonlinear dry friction force can be represented by using a single harmonic as

$$f_n(t) = f_{ns}\sin(\theta) + f_{nc}\cos(\theta), \tag{3.20}$$

$$f_{ns} = \frac{2}{\pi}\int_{\frac{\pi}{2}}^{\frac{3\pi}{2}} f_n(t)\sin(\theta)\,d\theta, \tag{3.21}$$

$$f_{nc} = \frac{2}{\pi}\int_{\frac{\pi}{2}}^{\frac{3\pi}{2}} f_n(t)\cos(\theta)\,d\theta. \tag{3.22}$$

By using Eq.(3.19),

$$f_{ns} = \frac{2}{\pi}\int_{\frac{\pi}{2}}^{\theta^*}\left(k_d\left(A\sin(\theta)-A\right)+\mu N\right)\sin(\theta)\,d\theta + \frac{2}{\pi}\int_{\theta^*}^{\frac{3\pi}{2}}(-\mu N)\sin(\theta)\,d\theta, \tag{3.23}$$

$$f_{nc} = \frac{2}{\pi}\int_{\frac{\pi}{2}}^{\theta^*}\left(k_d\left(A\sin(\theta)-A\right)+\mu N\right)\cos(\theta)\,d\theta + \frac{2}{\pi}\int_{\theta^*}^{\frac{3\pi}{2}}(-\mu N)\cos(\theta)\,d\theta, \tag{3.24}$$

which can be simplified as;

$$f_{ns} = \left(-\frac{4\mu N}{\pi}+\frac{2Ak_d}{\pi}\right)\cos(\theta^*) - \frac{Ak_d}{2\pi}\sin(2\theta^*) + \frac{Ak_d}{\pi}\theta^* - \frac{Ak_d}{2}, \tag{3.25}$$

$$f_{nc} = \left(\frac{4\mu N - 2Ak_d}{\pi}\right)\sin(\theta^*) + \frac{Ak_d}{\pi}\sin(\theta^*)^2 + \frac{Ak_d}{\pi}. \tag{3.26}$$

For the condition $Ak_d < \mu N$ friction interface does not experience stick-slip transition and it stays in stick state. This condition is represented as fully-stuck case and the friction force in this case can be represented as;

$$f_{ns} = \frac{1}{\pi}\int_0^{2\pi} Ak_d\sin(\theta)\sin(\theta)\,d\theta, \tag{3.27}$$

$$f_{ns} = Ak_d, \tag{3.28}$$

$$f_{nc} = \frac{1}{\pi}\int_0^{2\pi} Ak_d \sin(\theta)\cos(\theta)\,d\theta, \tag{3.29}$$

$$f_{nc} = 0. \tag{3.30}$$

If the input motion has phase angle it can be handled by assuming $\theta = \omega t + \psi$ using the obtained Fourier coefficients as follows;

$$f_n(t) = f_{ns}\sin(\omega t + \psi) + f_{nc}\cos(\omega t + \psi), \tag{3.31}$$

$$\begin{aligned} f_n(t) = {} & f_{ns}\left(\sin(\omega t)\cos(\psi) + \sin(\psi)\cos(\omega t)\right) \\ & + f_{nc}\left(\cos(\psi)\cos(\omega t) - \sin(\omega t)\sin(\psi)\right) \end{aligned}, \tag{3.32}$$

$$\begin{aligned} f_n(t) = {} & \left(f_{ns}\cos(\psi) - f_{nc}\sin(\psi)\right)\sin(\omega t) \\ & + \left(f_{ns}\sin(\psi) + f_{nc}\cos(\psi)\right)\cos(\omega t) \end{aligned}, \tag{3.33}$$

3.2 One-Dimensional Macroslip Friction Model with Gap

In this part a simple macroslip model with gap in which normal load is assumed to be constant and relative motion is one dimensional is studied. Illustration of the studied model is given in Fig. 5.

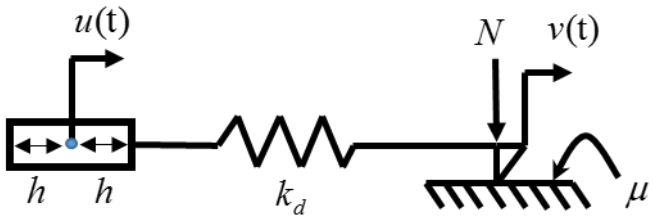

Fig. 5 Dry friction element for model with gap

Here, k_d is the tangential contact stiffness, N is the normal load, μ is coefficient of friction, h is the amount of gap, $u(t)$ is the tangential input motion and $v(t)$ is the slip motion.

Gapped interfaces represented by using one dimensional macroslip friction model can be in three different states; stick, slip and no contact. When the interface is in stick state, the force on the spring can be represented as;

$$f_n = k_d(\mathrm{u}-\mathrm{v}). \tag{3.34}$$

If the interface is in slip state, the force on the spring is constant and it is represented as;

$$f_n = \pm\mu N. \tag{3.35}$$

When the interface comes to the instant of slip to stick transition, both Eq.(3.34) and Eq.(3.35) are satisfied. Differentiating these two equations

$$\frac{df_n}{dt} = k_d\left(\frac{du}{dt}-\frac{dv}{dt}\right), \tag{3.36}$$

$$\frac{df_n}{dt} = 0. \tag{3.37}$$

Inserting Eq.(3.37) into Eq.(3.36)

$$k_d(\dot{u}-\dot{v}) = 0, \tag{3.38}$$

$$\dot{u} = \dot{v}. \tag{3.39}$$

From Eq.(3.39) it can be said that for one-dimensional motion with constant normal load, when the direction of input motion reverses slip-to-stick transition occurs.

Whenever the friction force reaches to its limiting values, stick-to-slip transition occurs. In slip state $u-v$ is constant and the friction interface moves with $\dot{u}$. By using Eq.(3.34) and Eq.(3.35) the relation can be written as;

$$f_n = k_d\left(u - v\right) = \pm\mu N\,, \tag{3.40}$$

$$f_n = k_d\left(u - u_0\right) + f_0 = \pm\mu N\,, \tag{3.41}$$

where u_0 and f_0 are the displacement and friction force at the beginning of stick state.

For one-dimensional friction model without a gap, stick state continues until the friction force reaches its limiting value which results in slip again. However, in one-dimensional fiction model with a gap, stick state continues until the friction force becomes zero and input motion loses its contact due the gap present in the model. The point where the contact loss occurs can be found by equating the stick force to zero as given in below;

$$f_n = k_d\left(u - u_0\right) + f_0 = 0 \tag{3.42}$$

After losing contact, system moves freely until passing through $2h$ gap distance and catch contact again. If the system moves in the direction of positive to negative slip, transition from the no contact to contact case which follows positive and negative slip-to-sick can be found by using the relations given below;

$$u(\mathrm{t}) = \mathrm{u}_{0c} - 2h \tag{3.43}$$

$$u(\mathrm{t}) = \mathrm{u}_{0c} + 2h \tag{3.44}$$

where u_{0c} is the displacement when the friction force becomes zero.

For single harmonic relative motion, input motion $u\left(t\right)$ can be written as

$$u\left(t\right) = A\sin\left(\theta\right). \tag{3.45}$$

Here, A is the amplitude of the relative motion and $\theta = \omega t$. Substituting Eq.(3.45) in Eq.(3.39), the following equation is obtained

$$\dot{u} = A\omega\cos\left(\theta\right) = 0\,. \tag{3.46}$$

Solution of Eq.(3.46) gives positive slip-to-stick and negative slip-to-stick transition angles as

$$\theta_{PSt} = \pi/2,\ \theta_{NSt} = 3\pi/2, \tag{3.47}$$

respectively, which correspond to the time when the relative input motion reverses its direction.

In order to determine transition angles of no contact, input motion and the friction force at the instant of slip-to-stick transition is required. Utilizing slip-to-stick transition angles given by Eq.(3.47), displacement and the friction force at the instant of slip-to-stick transition can be obtained as

$$u_0 = \mathrm{A},\ f_0 = \mu N \tag{3.48}$$

$$u_0 = -\mathrm{A},\ f_0 = -\mu N \tag{3.49}$$

Substituting Eqs.(3.45) and (3.48) in Eq.(3.42) transition angle for no contact following positive slip-to-stick can be obtained as follows

$$\theta_{PNC} = \pi - a\sin\left(1 - \frac{\mu N}{k_d A}\right) \tag{3.50}$$

Similarly, substituting Eqs.(3.45) and (3.49) in Eq.(3.42) transition angle for no contact following negative slip-to-stick can be obtained as follows

$$\theta_{NNC} = 2\pi - a\sin\left(1 - \frac{\mu N}{k_d A}\right) = \theta_{PNC} + \pi \tag{3.51}$$

After losing contact, no friction force is generated till the $2h$ gap is closed. Therefore, transition angles for contact following positive and negative slip-to-stick can be obtained by using Eq.(3.43) and Eq.(3.44) as

$$\theta_{PC} = \pi - a\sin\left(\sin\left(\theta_{PNC}\right) - \frac{2h}{A}\right) \tag{3.52}$$

$$\theta_{NC} = 2\pi - a\sin\left(\sin\left(\theta_{PNC}\right) - \frac{2h}{A}\right) \tag{3.53}$$

respectively, where

$$\theta_{NC} = \theta_{PC} + \pi \tag{3.54}$$

Substituting Eq.(3.53) into Eq.(3.41), transition angle for stick to positive slip can be obtained as

$$\theta_{PSl} = 2\pi - a\sin\left(\frac{-\mu N}{k_d A} + \sin\left(\theta_{PNC}\right) - \frac{2h}{A}\right) \tag{3.55}$$

Similarly, substituting Eq.(3.52) into Eq.(3.41), transition angle for stick to negative slip can be obtained as

$$\theta_{NSl} = \pi - a\sin\left(\frac{-\mu N}{k_d A} + \sin\left(\theta_{PNC}\right) - \frac{2h}{A}\right) \tag{3.56}$$

$$\theta_{PSl} = \theta_{NSl} + \pi \tag{3.57}$$

If the amplitude of relative motion is less than the gap, i.e. $A < h$, friction interface does not experience any contact and nonlinear contact force is given as

$$f_{n,1}\left(\theta\right) = 0 \tag{3.58}$$

If the maximum spring force is less than the slip load, i.e. $k_d\left(A - h\right) < \mu N$, friction interface does not experience slip state and it behaves a like a symmetric gap element which results in the following nonlinear force

$$f_{n,2}(\theta)=\begin{cases} k_d\left(A\sin(\theta)-h\right) & \text{if } \dfrac{\pi}{2}\le\theta<\theta_1 \\ 0 & \text{if } \theta_1\le\theta<\theta_2 \\ k_d\left(A\sin(\theta)+h\right) & \text{if } \theta_2\le\theta<\dfrac{3\pi}{2} \\ k_d\left(A\sin(\theta)+h\right) & \text{if } \dfrac{3\pi}{2}\le\theta<\pi+\theta_1 \\ 0 & \text{if } \pi+\theta_1\le\theta<\pi+\theta_2 \\ k_d\left(A\sin(\theta)-h\right) & \text{if } \pi+\theta_2\le\theta<\dfrac{5\pi}{2} \end{cases}, \tag{3.59}$$

where

$$\theta_1=\pi-a\sin\left(\frac{h}{A}\right) \tag{3.60}$$

$$\theta_2=\pi-a\sin\left(-\frac{h}{A}\right) \tag{3.61}$$

If the maximum spring force is greater than the slip load the friction interface experiences stick, slip, no contact states. Using the transition angles, friction force as a function of displacement, i.e. hysteresis curve, can be written as follows

$$f_{n,3}(\theta)=\begin{cases} k_d(\mathrm{Asin}(\theta)-\mathrm{A})+\mu\,\mathrm{N} & \text{if } \dfrac{\pi}{2}\le\theta<\theta_{PNC} \\ 0 & \text{if } \theta_{PNC}\le\theta<\theta_{PC} \\ k(\mathrm{Asin}(\theta)-(\mathrm{Asin}(\theta_{PNC})-2h)) & \text{if } \theta_{PC}\le\theta<\theta_{NSl} \\ -\mu N & \text{if } \theta_{NSl}\le\theta<\dfrac{3\pi}{2} \\ k_d(\mathrm{Asin}(\theta)+\mathrm{A})-\mu\,\mathrm{N} & \text{if } \dfrac{3\pi}{2}\le\theta<\theta_{PNC}+\pi \\ 0 & \text{if } \theta_{PNC}+\pi\le\theta<\theta_{PC}+\pi \\ k(\mathrm{Asin}(\theta)-\mathrm{Asin}(\theta_{PC}+\pi)) & \text{if } \theta_{PC}+\pi\le\theta<\theta_{NSl}+\pi \\ \mu N & \text{if } \theta_{NSl}+\pi\le\theta<\dfrac{5\pi}{2} \end{cases}. \tag{3.62}$$

A general hysteresis curve and a flow chart where the transition angles are shown is given in Fig. 6 and Fig. 7 for single harmonic motion. Depending on the parameters

of one-dimensional friction model with gap hysteresis curve for harmonic motion can take different shapes which shown in Fig. 8 and Fig. 9 as an example.

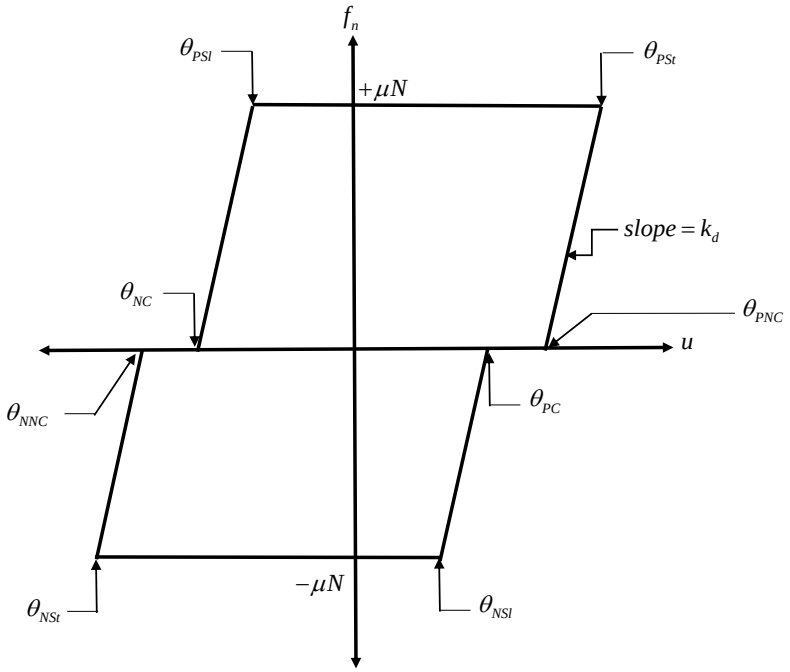

Fig. 6 Hysteresis Curve for Single Harmonic Motion

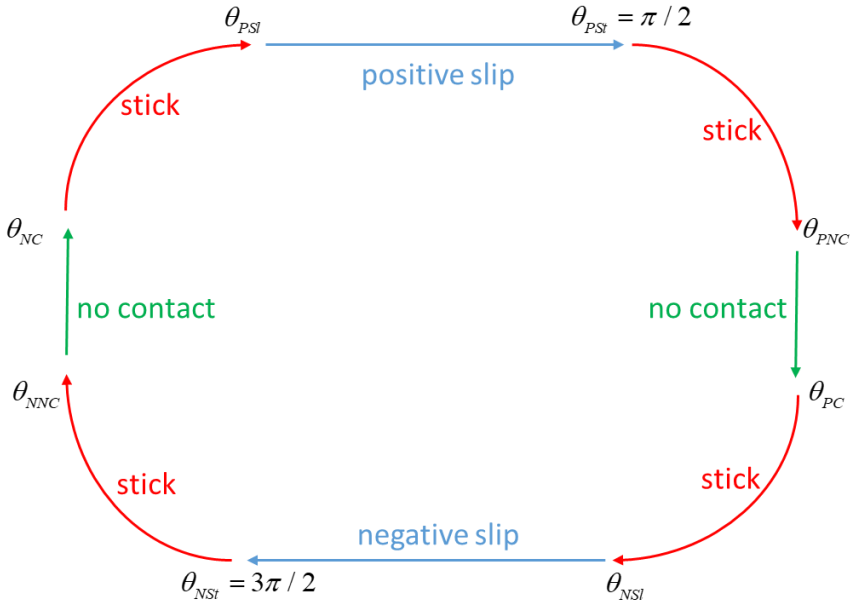

Fig. 7 Flow Chart for Single Harmonic Motion

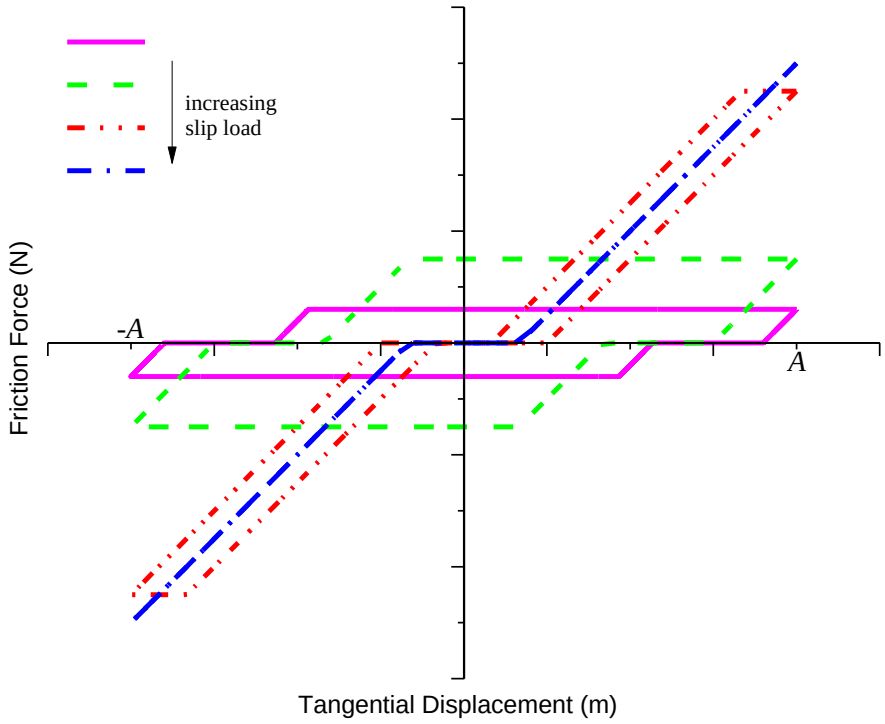

Fig. 8 Example hysteresis curves

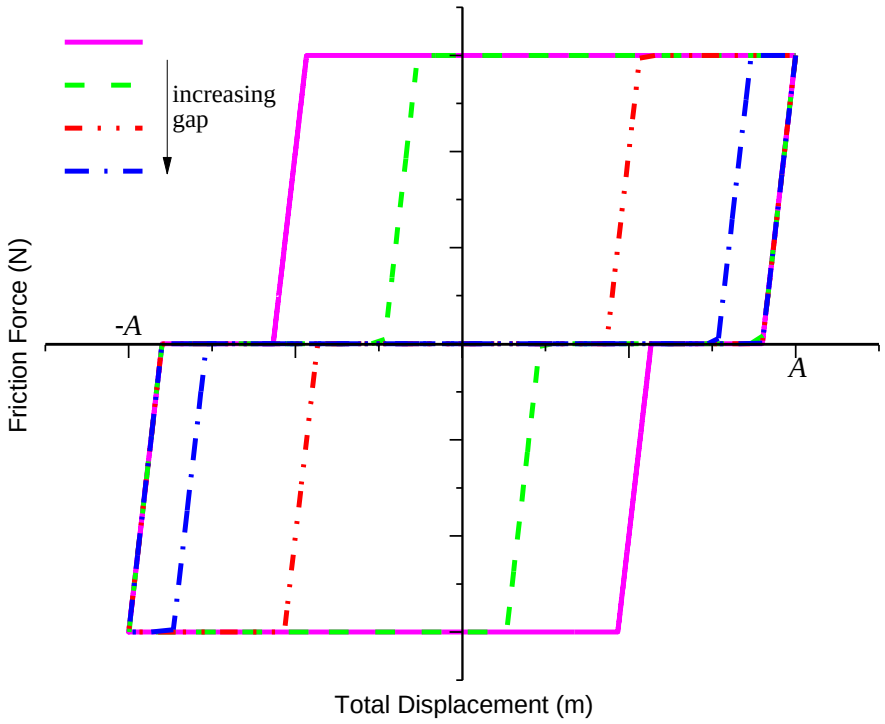

Fig. 9 Effect of Amount of Gap on Hysteresis Curve

The nonlinear contact force for one-dimensional dry friction element with gap can be expressed as

$$f_n(\theta)=\begin{cases} f_{n,1}(\theta) & \text{for } A<h \\ f_{n,2}(\theta) & \text{for } A>h \ \ \& \ \ k_d(A-h)<\mu N \\ f_{n,3}(\theta) & \text{for } k_d(A-h)>\mu N \end{cases}. \tag{3.63}$$

Utilizing a single harmonic Fourier series representation, the nonlinear contact force can be written as follows

$$f_n(t)=f_{ns}\sin(\theta)+f_{nc}\cos(\theta), \tag{3.64}$$

Considering the odd symmetric property of the nonlinearity Fourier coefficients f_{ns} and f_{nc} can be calculated as follows

$$f_{ns}=\frac{2}{\pi}\int_{\frac{\pi}{2}}^{\frac{3\pi}{2}} f_n(t)\sin(\theta)\,\mathrm{d}\theta, \tag{3.65}$$

$$f_{nc}=\frac{2}{\pi}\int_{\frac{\pi}{2}}^{\frac{3\pi}{2}} f_n(t)\cos(\theta)\,\mathrm{d}\theta. \tag{3.66}$$

Fourier coefficients of $f_{n,1}(\theta)$ are;

$$f_{n,1s}=0, \tag{3.67}$$

$$f_{n,1c}=0. \tag{3.68}$$

Fourier coefficients of $f_{n,2}(\theta)$ are;

$$f_{n,2s}=\frac{2}{\pi}k_d\left(\int_{\frac{\pi}{2}}^{\theta_1}\left(A\sin(\theta)-h\right)\sin(\theta)\,d\theta+\int_{\theta_2}^{\frac{3\pi}{2}}\left(A\sin(\theta)+h\right)\sin(\theta)\,d\theta\right), \tag{3.69}$$

$$f_{n,2s} = \left(-\frac{2hk_d}{\pi} \right) \sqrt{1 - \frac{h^2}{A^2}} + Ak_d \left(\frac{\theta_1 - \theta_2}{\pi} + 1 \right), \tag{3.70}$$

$$f_{n,2c} = \frac{2}{\pi} k_d \left(\int_{\frac{\pi}{2}}^{\theta_1} \left(A\sin(\theta) - h \right) \cos(\theta)\, d\theta + \int_{\theta_2}^{\frac{3\pi}{2}} \left(A\sin(\theta) + h \right) \cos(\theta)\, d\theta \right), \tag{3.71}$$

$$f_{n,2c} = 0\,. \tag{3.72}$$

Fourier coefficients of $f_{n,3}(\theta)$ are;

$$\begin{aligned} f_{n,3s} &= \frac{2}{\pi} \int_{\frac{\pi}{2}}^{\theta_{PNC}} \left(k_d (\mathrm{A}\sin(\theta) - \mathrm{A}) + \mu\, \mathrm{N} \right) \sin(\theta)\, \mathrm{d}\theta \\ &+ \frac{2}{\pi} \int_{\theta_{PC}}^{\theta_{NSl}} \left(k_d \left(\mathrm{A}\sin(\theta) - \left(\mathrm{A}\sin(\theta_{PNC}) - 2h \right) \right) \right) \sin(\theta)\, \mathrm{d}\theta\,, \\ &+ \frac{2}{\pi} \int_{\theta_{NSl}}^{\frac{3\pi}{2}} -\mu N \sin(\theta)\, \mathrm{d}\theta \end{aligned} \tag{3.73}$$

$$\begin{aligned} f_{n,3s} &= \frac{1}{2} k_d A - \frac{1}{\pi} \sqrt{\mu N \left(2k_d A - \mu N \right)} \left(1 - \frac{\mu N}{k_d A} \right) \\ &+ \frac{1}{\pi} \sqrt{\left(\mu N + 2hk_d \right) \left(2k_d A - \mu N - 2k_d h \right)} \left(1 - \frac{\mu N}{k_d A} - \frac{2h}{A} \right), \\ &- \frac{2}{\pi} \sqrt{\left(\mu N + hk_d \right) \left(k_d A - \mu N - k_d h \right)} \left(1 - \frac{2\mu N}{k_d A} - \frac{2h}{A} \right) \\ &+ \frac{1}{\pi} k_d A \left(\theta_{PNC} + \theta_{NSL} - \theta_{PC} - \pi \right) \end{aligned} \tag{3.74}$$

$$f_{n,3c} = \frac{2}{\pi}\int_{\frac{\pi}{2}}^{\theta_{PNC}} \left(k_d\left(\mathrm{Asin}\left(\theta\right)-\mathrm{A}\right)+\mu\,\mathrm{N}\right)\cos\left(\theta\right)\mathrm{d}\,\theta$$
$$+\frac{2}{\pi}\int_{\theta_{PC}}^{\theta_{NSl}} \left(k_d\left(\mathrm{Asin}\left(\theta\right)-\left(\mathrm{Asin}\left(\theta_{PNC}\right)-2h\right)\right)\right)\cos\left(\theta\right)\mathrm{d}\,\theta\,, \qquad (3.75)$$
$$+\frac{2}{\pi}\int_{\theta_{NSl}}^{\frac{3\pi}{2}} -\mu N\cos\left(\theta\right)\mathrm{d}\,\theta$$

$$f_{n,3c} = \frac{4\mu N\left(-\mu N + k_d A - hk_d\right)}{\pi k_d A}. \qquad (3.76)$$

3.3 Two-Dimensional Macroslip Friction Model with Constant Load

In this part, a macroslip model in which normal load is assumed to be constant and relative motion is two dimensional, is studied. Studied model is developed by (Menq & Yang, 1998). This model is used for the mechanical interfaces with friction constraint experiencing two-dimensional relative motion. It can be used for both elliptical and circular motion which is a special case of elliptical motion. For the calculation of the contact kinematics of friction interfaces experiencing elliptical motion, major and minor principals of elliptical motion shown in Fig. 10 is used. First, coordinate transformation given in the study of (Menq et al., 1991) is described.

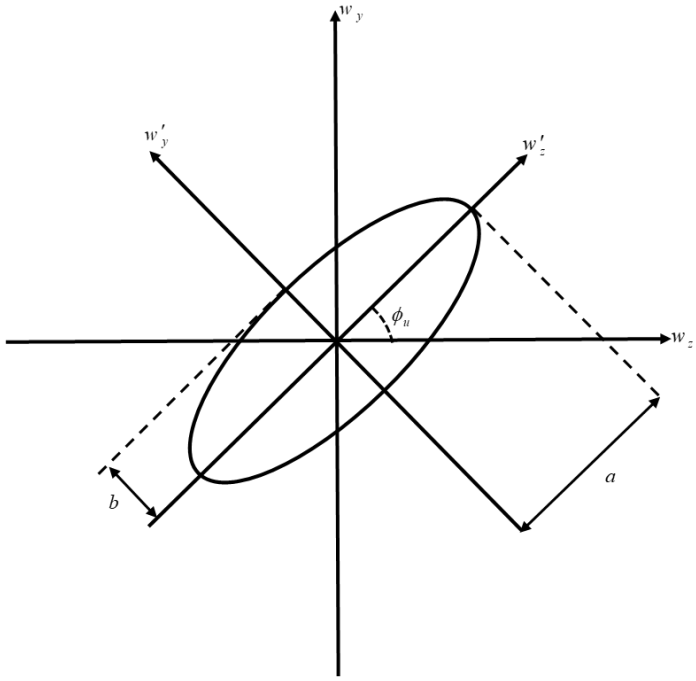

Fig. 10 Coordinate transformation

Input motions are defined previously in Eq.(2.21) and Eq.(2.22). Assume these input motions as;

$$w_z(t) = a_{11}\cos(\omega t) + a_{12}\sin(\omega t), \tag{3.77}$$

$$w_y(t) = a_{21}\cos(\omega t) + a_{22}\sin(\omega t), \tag{3.78}$$

Two equations defined above can be written in matrix form as;

$$\begin{bmatrix} w_z \\ w_y \end{bmatrix} = \begin{bmatrix} a_{11} & a_{12} \\ a_{21} & a_{22} \end{bmatrix} \begin{bmatrix} \cos(\omega t) \\ \sin(\omega t) \end{bmatrix}, \tag{3.79}$$

Let,

$$\begin{bmatrix} a_{11} & a_{12} \\ a_{21} & a_{22} \end{bmatrix} = \begin{bmatrix} \cos(\phi_u) & -\sin(\phi_u) \\ \sin(\phi_u) & \cos(\phi_u) \end{bmatrix} \begin{bmatrix} a & 0 \\ 0 & b \end{bmatrix} \begin{bmatrix} \cos(\phi_u) & \sin(\phi_u) \\ -\sin(\phi_u) & \cos(\phi_u) \end{bmatrix}, \tag{3.80}$$

where ϕ_u is the inclination of the major axis to the x axis and ϕ_v is the initial phase of the motion . As explained in (Menq et al., 1991), four simultaneous non-linear

equations coming from Eq.(3.80) can be solved and following expressions are obtained;

$$a = \frac{1}{2}\left[\sqrt{\left(a_{11}+a_{22}\right)^2+\left(a_{21}-a_{12}\right)^2}+\sqrt{\left(a_{11}-a_{22}\right)^2+\left(a_{12}+a_{21}\right)^2}\right], \quad (3.81)$$

$$b = \frac{1}{2}\left[\sqrt{\left(a_{11}+a_{22}\right)^2+\left(a_{21}-a_{12}\right)^2}-\sqrt{\left(a_{11}-a_{22}\right)^2+\left(a_{12}+a_{21}\right)^2}\right], \quad (3.82)$$

$$\phi_u = \frac{1}{2}\left[\tan^{-1}\left(\frac{a_{12}+a_{21}}{a_{11}-a_{22}}\right)+\tan^{-1}\left(\frac{a_{21}-a_{12}}{a_{11}+a_{22}}\right)\right], \quad (3.83)$$

$$\phi_v = \frac{1}{2}\left[\tan^{-1}\left(\frac{a_{12}+a_{21}}{a_{11}-a_{22}}\right)-\tan^{-1}\left(\frac{a_{21}-a_{12}}{a_{11}+a_{22}}\right)\right]. \quad (3.84)$$

Eq.(3.77) and Eq.(3.78) can be written as;

$$w_z = a\cos(\theta), \quad (3.85)$$

$$w_y = b\sin(\theta), \quad (3.86)$$

$$\theta = \omega t - \phi_v. \quad (3.87)$$

Back transformation formulation can be written as;

$$\begin{bmatrix} f_x \\ f_y \end{bmatrix} = \begin{bmatrix} \cos(\phi_u) & -\sin(\phi_u) \\ \sin(\phi_u) & \cos(\phi_u) \end{bmatrix} \begin{bmatrix} f_x' \\ f_y' \end{bmatrix}. \quad (3.88)$$

As mentioned before, this model is used for the mechanical interfaces with friction constraint experiencing two-dimensional relative motion. Fig. 11 shows such a model with defined contact plane and invariant orientation. One of the contacting surfaces assumed as ground and contact normal load is assumed as constant. Friction element which obeys the Coulomb friction law and massless elastic element which represents the frictional interface are the two main aspects of the model. Here u denotes the input relative motion, v is the slip motion of the contact point, f is the

induced friction force, k_d is the tangential contact stiffness, N is the normal load, μ is coefficient of friction.

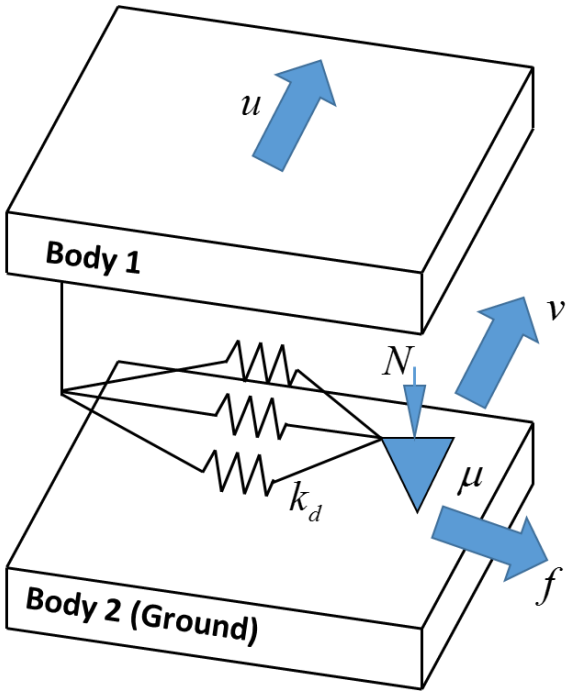

Fig. 11 Two-dimensional dry friction element

For simplicity parameters given below are defined.

$$\bar{u} = \frac{k_d u}{\mu N}, \tag{3.89}$$

$$\bar{v} = \frac{k_d v}{\mu N}, \tag{3.90}$$

$$\bar{f} = \frac{f}{\mu N}. \tag{3.91}$$

The dimensionless force acting on the ground is expressed as;

$$\bar{f} = \bar{u} - \bar{v}. \tag{3.92}$$

Under the effect of small vibrations, contact point stays in stick state with the friction force proportional to input motion and with zero slip velocity. According to

Coulomb friction law friction force is limited to slip force μN. At some point friction force on the interface reaches to value of slip force and at that point interface enters to slip state in which the friction force remains constant. Stick condition can be expressed as;

$$\left| \bar{f} = \bar{u} - \bar{u}_0 + \bar{f}_0 \right| < 1, \tag{3.93}$$

$$\dot{\bar{v}} = 0. \tag{3.94}$$

Slip condition can be expressed as;

$$\bar{f} = \frac{\dot{\bar{v}}}{\left|\dot{\bar{v}}\right|}, \tag{3.95}$$

$$\dot{\bar{v}} \neq 0, \tag{3.96}$$

where $\bar{u}_0$ and $\bar{f}_0$ are the initial values of $\bar{u}$ and $\bar{f}$ at the beginning of the stick state.

In order to evaluate the frictional behavior of the interface with elliptical motion, it is very important to find the two possible transition points, stick-to-slip and slip-to-stick, very accurately. As mentioned before stick-to-slip transition, when the amplitude of the friction force tends to exceed the slip load, can be determined easily like done in the one-dimensional case. However, it is not possible to find the slip-to-stick transition like done in one-dimensional case where transition occurs when the direction of relative input motion reverses. Because in elliptical case, input motion never reverses its direction. For that reason, slip velocity can be used to find the slip-to-stick transition point. Transition occurs when the slip velocity becomes zero.

Stick-to-slip transition occurs when the amplitude of the friction force tends to exceed the slip load and can be shown mathematically as;

$$\left| \bar{f} = \bar{u} - \bar{u}_0 + \bar{f}_0 \right| = 1, \tag{3.97}$$

$$\left| \dot{\bar{f}} \right| > 0. \tag{3.98}$$

Given condition for the stick-to-slip can be transformed into a quartic equation and can be solved analytically. Relative input motion can be assumed as;

$$\bar{u} = \begin{bmatrix} a\cos(\theta) & b\sin(\theta) \end{bmatrix}^T . \tag{3.99}$$

Eq.(3.97) can be written as;

$$\left|\bar{f}\right| = \begin{vmatrix} a\cos(\theta) + C_1 \\ b\sin(\theta) + C_2 \end{vmatrix} = 1, \tag{3.100}$$

$$\sqrt{\left(a\cos(\theta) + C_1\right)^2 + \left(b\sin(\theta) + C_2\right)^2} = 1 . \tag{3.101}$$

Take square of the both sides of Eq.(3.101)

$$C_1^{\,2} + 2C_1 a\cos(\theta) + C_2^{\,2} + 2C_2 b\sin(\theta) + a^2\cos(\theta)^2 + b^2\sin(\theta)^2 = 1 . \tag{3.102}$$

It is known that;

$$\cos(\theta)^2 = 1 - \sin(\theta)^2 . \tag{3.103}$$

Insert Eq.(3.103) into Eq.(3.102) and rearrange it.

$$\left(b^2 - a^2\right)\sin(\theta)^2 + 2bC_2\sin(\theta) + a^2 + C_1^{\,2} + C_2^{\,2} = 1 - 2\cos(\theta)C_1 a . \tag{3.104}$$

Take the square of the both sides of the Eq.(3.104), insert Eq.(3.103) into the new equation and arrange it.

$$\begin{aligned} &\left(a^2 - b^2\right)^2 \sin(\theta)^4 - 4C_2 b\left(a^2 - b^2\right)\sin(\theta)^3 \\ &+\left[4C_1^{\,2}a^2 - 2\left(a^2 - b^2\right)\left(C_1^{\,2} + C_2^{\,2} + a^2 - 1\right) + 4C_2^{\,2}b^2\right]\sin(\theta)^2 \\ &4C_2 b\left(C_1^{\,2} + C_2^{\,2} + a^2 - 1\right)\sin(\theta) + \left(C_1^{\,2} + C_2^{\,2} + a^2 - 1\right)^2 - 4C_1^{\,2}a^2 = 0 \end{aligned} . \tag{3.105}$$

Eq.(3.105) can be written as;

$$A_4\sin(\theta)^4 + A_3\sin(\theta)^3 + A_2\sin(\theta)^2 + A_1\sin(\theta) + A_0 = 0 , \tag{3.106}$$

where

$$A_4 = \left(a^2 - b^2\right)^2, \tag{3.107}$$

$$A_3 = -4C_2 b\left(a^2 - b^2\right), \tag{3.108}$$

$$A_2 = \left[4C_1{}^2 a^2 - 2\left(a^2 - b^2\right)\left(C_1{}^2 + C_2{}^2 + a^2 - 1\right) + 4C_2{}^2 b^2\right], \tag{3.109}$$

$$A_1 = 4C_2 b\left(C_1{}^2 + C_2{}^2 + a^2 - 1\right), \tag{3.110}$$

$$A_0 = \left(C_1{}^2 + C_2{}^2 + a^2 - 1\right)^2 - 4C_1{}^2 a^2. \tag{3.111}$$

Eq.(3.106) can be solved analytically by using the method given in Appendix A.

As described above it is harder to find the slip-to-stick transition. It can be found by using the conditions given in Eq.(3.94) and Eq.(3.96). For the slip state, slip motion which is along the friction force direction is written as;

$$\dot{\bar{v}} = c\bar{f}, \tag{3.112}$$

where $c > 0$.

Friction force has a constant magnitude so;

$$\bar{f}^T \dot{\bar{f}} = 0. \tag{3.113}$$

Differentiate Eq.(3.92) and insert Eq.(3.112) into it;

$$\bar{f}^T \dot{\bar{u}} - c\bar{f}^T \bar{f} = 0. \tag{3.114}$$

It is known that $\bar{f}^T \bar{f} = 1$, c can be found as follows;

$$c = \bar{f}^T \dot{\bar{u}}. \tag{3.115}$$

Insert Eq.(3.115) into Eq.(3.112)

$$\dot{\bar{v}} = \bar{f}^T \dot{\bar{u}} \bar{f}. \tag{3.116}$$

Insert Eq.(3.116) into the differentiation of Eq.(3.92)

$$\dot{\bar{f}} = \dot{\bar{u}} - \bar{f}^T \dot{\bar{u}} \bar{f} \ . \tag{3.117}$$

From Eq.(3.116), $\dot{\bar{v}} = 0$ implies;

$$\bar{f}^T \dot{\bar{u}} = 0 \, . \tag{3.118}$$

During the slip motion friction force can be expressed as;

$$\bar{f} = \left[\cos(\varphi) \quad \sin(\varphi) \right]^T . \tag{3.119}$$

Insert Eq.(3.99) and Eq.(3.119) into Eq.(3.117);

$$\frac{d\varphi}{d\theta} = \frac{a+b}{2} \cos(\theta - \varphi) - \frac{a-b}{2} \cos(\theta + \varphi) . \tag{3.120}$$

Similarly from Eq.(3.115);

$$c = \omega \left[-\frac{a+b}{2} \sin(\theta - \varphi) - \frac{a-b}{2} \sin(\theta + \varphi) \right] . \tag{3.121}$$

Eq.(3.120) can not be solved analytically, so it is solved numerically. By solving Eq.(3.120), induced friction force for the slip state and the result of Eq.(3.121) can be found. It is known that during the slip state c has to be positive, so it can be said that when the c constant changes its sign, slip-to-stick transition occurs. After finding the transition points, stick-slip hysteresis diagram given in Fig. 12 can be drawn.

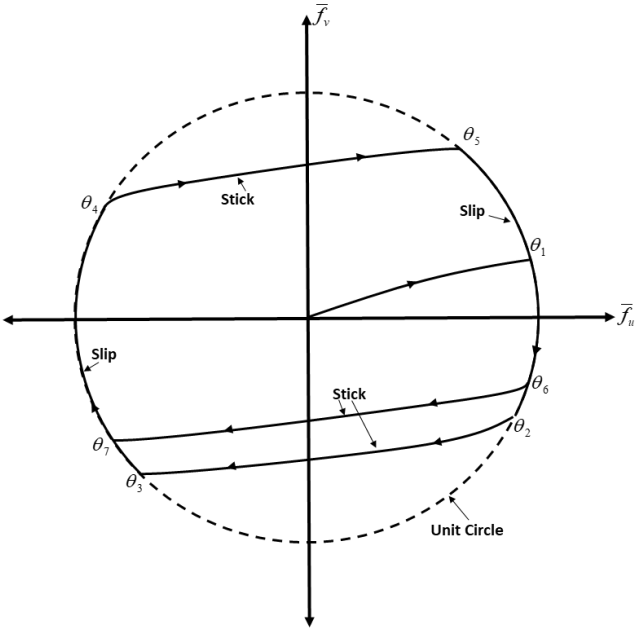

Fig. 12 Friction force trajectory

In the diagram, while trajectories inside the unit circle represent the stick state, trajectories following the unit circle represent the slip state. When the motion starts, friction interface starts form the stick state with zero friction force. Stick state continues until the friction force tends to pass the slip force which is stated mathematically in Eq.(3.97), in other words, until the stick trajectory meets unit circle. By solving Eq.(3.97) transition angle θ_1 can be found. After the transition to slip state, Eq.(3.120) and Eq.(3.121) can be solved to find the φ and c values. c value is used to find the slip-to-stick transition angle θ_2 because it is known that slip-to-stick transition occurs when c crosses zero. This continues with the same pattern until the friction force reaches to steady state.

For the mechanical interfaces with friction constraint experiencing two-dimensional elliptical motion, there are three possible friction force trajectories. If the amplitude of input relative motion is small, the friction interface remains stuck and friction trajectory becomes an ellipse like shown in Fig. 13 and it is called fully-stuck state. When the amplitude of input relative motion increases, friction interface enters to

slip state and followed an alternating stick and slip motion with the resulting trajectory given in Fig. 14. This trajectory is the steady state version of the one given in Fig. 12. After amplitude of input relative motion passes the certain amount, it enters to fully-slip state and the resulting trajectory becomes circle which is shown in Fig. 15.

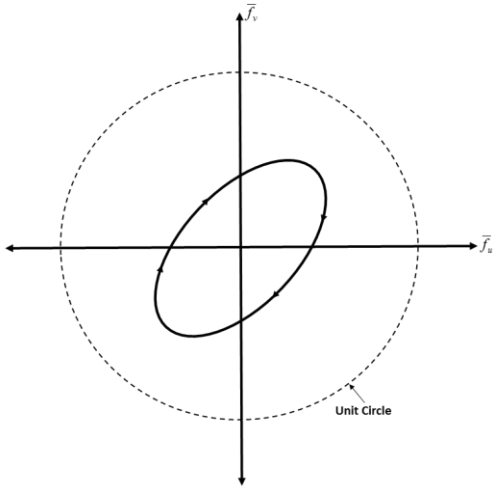

Fig. 13 Fully-stuck trajectory

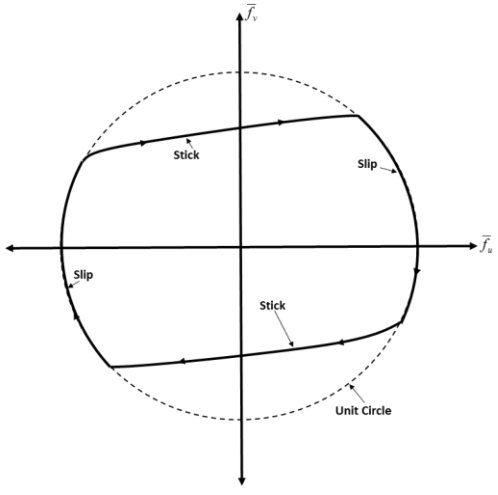

Fig. 14 Stick-slip state trajectory

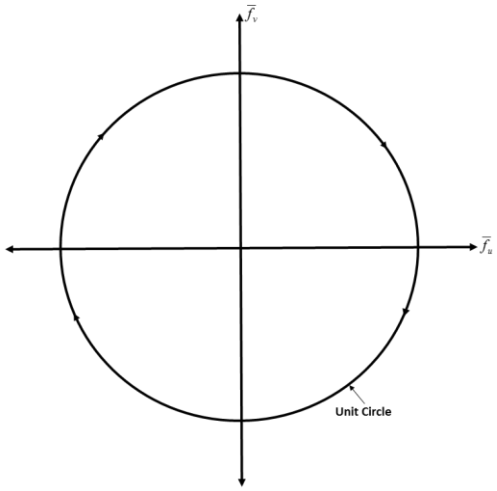

Fig. 15 Fully-slip trajectory

Once the steady state friction forces are found, Fourier Transform can be used to separate the forces into its sine and cosine components. Friction force can be written as;

$$\bar{f} = \begin{bmatrix} \bar{f}^z \\ \bar{f}^y \end{bmatrix} = \begin{bmatrix} \bar{f}_s^z \sin(\theta) + \bar{f}_c^z \cos(\theta) \\ \bar{f}_s^y \sin(\theta) + \bar{f}_c^y \cos(\theta) \end{bmatrix}. \tag{3.122}$$

Here force components in-phase with the input motion provide additional spring resistance, while components 90° out of phase add friction damping to the interface.

For the interface in fully-stuck state, friction force is;

$$\bar{f} = \begin{bmatrix} a\cos(\theta) \\ b\sin(\theta) \end{bmatrix}. \tag{3.123}$$

Employ one-term Fourier series expansion

$$\bar{f}_s^z = \frac{1}{\pi}\int_0^{2\pi} a\cos(\theta)\sin(\theta)\,d\theta, \tag{3.124}$$

$$\bar{f}^z = 0, \tag{3.125}$$

$$\overline{f}_c^z = \frac{1}{\pi}\int_0^{2\pi} a\cos(\theta)\cos(\theta)\,d\theta, \tag{3.126}$$

$$\overline{f}_c^z = a, \tag{3.127}$$

$$\overline{f}_s^y = \frac{1}{\pi}\int_0^{2\pi} b\sin(\theta)\sin(\theta)\,d\theta, \tag{3.128}$$

$$\overline{f}_s^y = b, \tag{3.129}$$

$$\overline{f}_c^y = \frac{1}{\pi}\int_0^{2\pi} b\sin(\theta)\cos(\theta)\,d\theta, \tag{3.130}$$

$$\overline{f}_c^y = 0. \tag{3.131}$$

For the interface in alternating slip-stick state,

$$\begin{aligned}\overline{f}_s^z = &\frac{1}{\pi}\int_0^{\theta_1}\left[\cos(\varphi)\right]\sin(\theta)\,d\theta + \frac{1}{\pi}\int_{\theta_1}^{\theta_2}\left[a\cos(\theta) - \overline{u}_0 + \overline{f}_0\right]\sin(\theta)\,d\theta \\ &+\frac{1}{\pi}\int_{\theta_2}^{\theta_3}\left[\cos(\varphi)\right]\sin(\theta)\,d\theta + \frac{1}{\pi}\int_{\theta_3}^{\theta_4}\left[a\cos(\theta) - \overline{u}_0 + \overline{f}_0\right]\sin(\theta)\,d\theta\end{aligned}, \tag{3.132}$$

$$\begin{aligned}\overline{f}_c^z = &\frac{1}{\pi}\int_0^{\theta_1}\left[\cos(\varphi)\right]\cos(\theta)\,d\theta + \frac{1}{\pi}\int_{\theta_1}^{\theta_2}\left[a\cos(\theta) - \overline{u}_0 + \overline{f}_0\right]\cos(\theta)\,d\theta \\ &+\frac{1}{\pi}\int_{\theta_2}^{\theta_3}\left[\cos(\varphi)\right]\cos(\theta)\,d\theta + \frac{1}{\pi}\int_{\theta_3}^{\theta_4}\left[a\cos(\theta) - \overline{u}_0 + \overline{f}_0\right]\cos(\theta)\,d\theta\end{aligned}, \tag{3.133}$$

$$\begin{aligned}\overline{f}_s^y = &\frac{1}{\pi}\int_0^{\theta_1}\left[\sin(\varphi)\right]\sin(\theta)\,d\theta + \frac{1}{\pi}\int_{\theta_1}^{\theta_2}\left[a\sin(\theta) - \overline{u}_0 + \overline{f}_0\right]\sin(\theta)\,d\theta \\ &+\frac{1}{\pi}\int_{\theta_2}^{\theta_3}\left[\sin(\varphi)\right]\sin(\theta)\,d\theta + \frac{1}{\pi}\int_{\theta_3}^{\theta_4}\left[a\sin(\theta) - \overline{u}_0 + \overline{f}_0\right]\sin(\theta)\,d\theta\end{aligned}, \tag{3.134}$$

$$\bar{f}_c^{\,y} = \frac{1}{\pi}\int_0^{\theta_1}\left[\sin(\varphi)\right]\cos(\theta)\,d\theta + \frac{1}{\pi}\int_{\theta_1}^{\theta_2}\left[a\sin(\theta) - \bar{u}_0 + \bar{f}_0\right]\cos(\theta)\,d\theta + \frac{1}{\pi}\int_{\theta_2}^{\theta_3}\left[\sin(\varphi)\right]\cos(\theta)\,d\theta + \frac{1}{\pi}\int_{\theta_3}^{\theta_4}\left[a\sin(\theta) - \bar{u}_0 + \bar{f}_0\right]\cos(\theta)\,d\theta \quad , (3.135)$$

where θ_1 ,θ_2 ,θ_3 and θ_4 are transition angles. While the first and third parts of the equations defined above represent slip state, second and fourth parts define stick state.

For the interface in fully-slip state,

$$\bar{f}_s^{\,z} = \frac{1}{\pi}\int_0^{2\pi}\left[\cos(\varphi)\right]\sin(\theta)\,d\theta, \tag{3.136}$$

$$\bar{f}_c^{\,z} = \frac{1}{\pi}\int_0^{2\pi}\left[\cos(\varphi)\right]\cos(\theta)\,d\theta, \tag{3.137}$$

$$\bar{f}_s^{\,y} = \frac{1}{\pi}\int_0^{2\pi}\left[\sin(\varphi)\right]\sin(\theta)\,d\theta, \tag{3.138}$$

$$\bar{f}_c^{\,y} = \frac{1}{\pi}\int_0^{2\pi}\left[\sin(\varphi)\right]\cos(\theta)\,d\theta. \tag{3.139}$$

After finding the force values back transformation should be practiced.

$$\begin{bmatrix}\bar{f}^{\,zb}\\ \bar{f}^{\,yb}\end{bmatrix} = \begin{bmatrix}\cos(\phi_u) & -\sin(\phi_u)\\ \sin(\phi_u) & \cos(\phi_u)\end{bmatrix}\begin{bmatrix}\bar{f}^{\,z}\\ \bar{f}^{\,y}\end{bmatrix}, \tag{3.140}$$

$$\begin{bmatrix}\bar{f}^{\,zb}\\ \bar{f}^{\,yb}\end{bmatrix} = \begin{bmatrix}\bar{f}_s^{\,zb}\sin(\theta) + \bar{f}_c^{\,zb}\cos(\theta)\\ \bar{f}_s^{\,yb}\sin(\theta) + \bar{f}_c^{\,yb}\cos(\theta)\end{bmatrix}. \tag{3.141}$$

3.3.1 Two-Dimensional Macroslip Friction Model for Circular Motion

In this part a macro slip model in which normal load is constant and relative motion is circular is studied. Studied model is developed by (Menq & Yang, 1998). Circular motion is the special case of the elliptical motion and for the convenience same formulation given in previous part is used. Unlike the elliptical motion, for the circular motion coordinate transformation is not needed.

$$w_z(x,t) = \sum_j \phi_j(x) q_{js} \sin(\omega t) + \sum_j \phi_j(x) q_{jc} \cos(\omega t), \tag{3.142}$$

$$w_y(x,t) = \sum_j \phi_j(x) r_{js} \sin(\omega t) + \sum_j \phi_j(x) r_{jc} \cos(\omega t), \tag{3.143}$$

$$w_z(x,t) = a\cos\left(\omega t + \psi_1 - \frac{\pi}{2}\right), \tag{3.144}$$

$$w_y(x,t) = a\cos(\omega t + \psi_2), \tag{3.145}$$

$$w_z(x,t) = a\cos(\theta), \tag{3.146}$$

$$w_y(x,t) = b\sin(\theta). \tag{3.147}$$

Assume

$$\bar{u} = \left[a\cos(\theta) \quad b\sin(\theta)\right]^T. \tag{3.148}$$

When the amplitudes of two input motions, a and b, become equal, elliptical motion becomes circular. If $a<1$ the contact is in fully stick state. For the values where $a \geq 1$ Eq.(3.120) and Eq.(3.121) become

$$\frac{d\varphi}{d\theta} = a\cos(\theta - \varphi), \tag{3.149}$$

$$c = -a\omega\sin(\theta - \varphi). \tag{3.150}$$

It is known that for the slip motion c value has to be positive, so the solutions of above two equations can be found analytically as;

$$\varphi = \theta + \cos^{-1}\left(1/a\right), \tag{3.151}$$

$$c = \omega\sqrt{a^2 - 1}. \tag{3.152}$$

From Eq.(3.152) it is seen that if the contact changes its behavior from stick to slip, it will continue in slip state because c value will be positive after the transition. So it can be said that for the frictional interface having circular motion, there are only two possible states whose trajectories are given in Fig. 16, fully-stuck and full-slip. From Eq.(3.151) it is seen that phase difference between the input relative motion and the friction force is $\cos^{-1}\left(1/a\right)$. When a equals to one, friction interface enters to slip state but due to zero phase, friction force behaves as pure spring constraint. When a gets larger, phase angle get closer to 90° and friction force behaves as damping force.

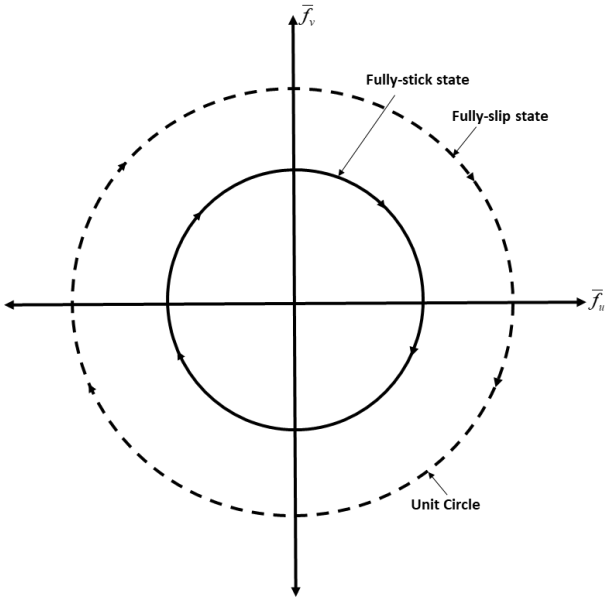

Fig. 16 Circular motion trajectories

Once the steady state friction forces are found, Fourier Transform can be used to separate the forces into its sine and cosine components. Friction force can be written as;

$$\bar{f} = \begin{bmatrix} \bar{f}^{z} \\ \bar{f}^{y} \end{bmatrix} = \begin{bmatrix} \bar{f}_s^{z} \sin(\theta) + \bar{f}_c^{z} \cos(\theta) \\ \bar{f}_s^{y} \sin(\theta) + \bar{f}_c^{y} \cos(\theta) \end{bmatrix}. \tag{3.153}$$

For the interface in fully-stuck state, friction force is;

$$\bar{f} = \begin{bmatrix} a\cos(\theta) \\ b\sin(\theta) \end{bmatrix}. \tag{3.154}$$

Employ one-term Fourier series expansion

$$\bar{f}_s^{z} = \frac{1}{\pi}\int_0^{2\pi} a\cos(\theta)\sin(\theta)\,d\theta, \tag{3.155}$$

$$\bar{f}_s^{z} = 0, \tag{3.156}$$

$$\bar{f}_c^{z} = \frac{1}{\pi}\int_0^{2\pi} a\cos(\theta)\cos(\theta)\,d\theta, \tag{3.157}$$

$$\bar{f}_c^{z} = a, \tag{3.158}$$

$$\bar{f}_s^{y} = \frac{1}{\pi}\int_0^{2\pi} \mathrm{a}\sin(\theta)\sin(\theta)\,d\theta, \tag{3.159}$$

$$\bar{f}_s^{y} = a, \tag{3.160}$$

$$\bar{f}_c^{y} = \frac{1}{\pi}\int_0^{2\pi} \mathrm{a}\sin(\theta)\cos(\theta)\,d\theta, \tag{3.161}$$

$$\bar{f}_c^{y} = 0. \tag{3.162}$$

For the interface in fully-slip state, friction force is

$$\bar{f} = \begin{bmatrix} \cos(\varphi) \\ \sin(\varphi) \end{bmatrix}, \tag{3.163}$$

$$\bar{f}_s^z = \frac{1}{\pi}\int_0^{2\pi} \left[\cos(\varphi)\right] \sin(\theta)\, d\theta, \tag{3.164}$$

$$\bar{f}_c^z = \frac{1}{\pi}\int_0^{2\pi} \left[\cos(\varphi)\right] \cos(\theta)\, d\theta, \tag{3.165}$$

$$\bar{f}_s^y = \frac{1}{\pi}\int_0^{2\pi} \left[\sin(\varphi)\right] \sin(\theta)\, d\theta, \tag{3.166}$$

$$\bar{f}_c^y = \frac{1}{\pi}\int_0^{2\pi} \left[\sin(\varphi)\right] \cos(\theta)\, d\theta. \tag{3.167}$$

By inserting Eq.(3.151) into Eq.(3.164)-(3.167);

$$\bar{f}_s^z = \frac{1}{\pi}\int_0^{2\pi} \left[\cos\left(\theta + \cos^{-1}(1/a)\right)\right] \sin(\theta)\, d\theta = -\sqrt{1-\left(\frac{1}{a}\right)^2}, \tag{3.168}$$

$$\bar{f}_c^z = \frac{1}{\pi}\int_0^{2\pi} \left[\cos\left(\theta + \cos^{-1}(1/a)\right)\right] \cos(\theta)\, d\theta = \left(\frac{1}{a}\right), \tag{3.169}$$

$$\bar{f}_s^y = \frac{1}{\pi}\int_0^{2\pi} \left[\sin\left(\theta + \cos^{-1}(1/a)\right)\right] \sin(\theta)\, d\theta = \left(\frac{1}{a}\right), \tag{3.170}$$

$$\bar{f}_c^y = \frac{1}{\pi}\int_0^{2\pi} \left[\sin\left(\theta + \cos^{-1}(1/a)\right)\right] \cos(\theta)\, d\theta = \sqrt{1-\left(\frac{1}{a}\right)^2}. \tag{3.171}$$

Same results given in Eq.(3.168)-(3.171) can be obtained directly by inserting Eq.(3.151) into Eq.(3.163).

CHAPTER 4

NONLINEAR SOLUTION METHOD

4.1 Harmonic Balance Method

The nonlinear ordinary differential equation set defined by Eq.(2.49) is converted into a set of nonlinear algebraic equations by using Harmonic Balance Method. For this purpose, by using a single harmonic representation, generalized coordinates can be expressed as follows

$$\{q\} = \{q_s\}\sin(\omega t) + \{q_c\}\cos(\omega t), \tag{4.1}$$

$$\{r\} = \{r_s\}\sin(\omega t) + \{r_c\}\cos(\omega t), \tag{4.2}$$

where $\{q_s\}$, $\{r_s\}$ and $\{q_c\}$, $\{r_c\}$ are the sine and cosine components of the vectors of generalized coordinates. Similarly, utilizing Fourier series, nonlinear forcing and external excitation force vectors can be written as;

$$\{F_{nz}(t)\} = \{F_{nzs}\}\sin(\omega t) + \{F_{nzc}\}\cos(\omega t), \tag{4.3}$$

$$\{F_{ny}(t)\} = \{F_{nys}\}\sin(\omega t) + \{F_{nyc}\}\cos(\omega t), \tag{4.4}$$

$$\{F_z(t)\} = \{F_{zs}\}\sin(\omega t) + \{F_{zc}\}\cos(\omega t), \tag{4.5}$$

$$\{F_y(t)\} = \{F_{ys}\}\sin(\omega t) + \{F_{yc}\}\cos(\omega t), \tag{4.6}$$

where $\{F_{nzs}\}$, $\{F_{nys}\}$ and $\{F_{nzc}\}$, $\{F_{nyc}\}$ are the sine and cosine components of the nonlinear internal forcing vectors and $\{F_{zs}\}$, $\{F_{ys}\}$ and $\{F_{zc}\}$, $\{F_{yc}\}$ are the sine and cosine components of external forcing vectors. After inserting Eq.(4.1)-(4.6) into Eq.(2.49) and separating sine and cosine components, the following nonlinear algebraic equations are obtained.

$$\begin{bmatrix} [\Omega]-\omega^2[I] & 0 & 0 & 0 \\ 0 & [\Omega]-\omega^2[I] & 0 & 0 \\ 0 & 0 & [\Omega]-\omega^2[I] & 0 \\ 0 & 0 & 0 & [\Omega]-\omega^2[I] \end{bmatrix} \begin{Bmatrix} q_s \\ q_c \\ r_s \\ r_c \end{Bmatrix} + \begin{bmatrix} 0 & -\omega[C_r] & 0 & 0 \\ \omega[C_r] & 0 & 0 & 0 \\ 0 & 0 & 0 & -\omega[C_r] \\ 0 & 0 & \omega[C_r] & 0 \end{bmatrix} \begin{Bmatrix} q_s \\ q_c \\ r_s \\ r_c \end{Bmatrix} + \begin{Bmatrix} F_{nzs} \\ F_{nzc} \\ F_{nys} \\ F_{nyc} \end{Bmatrix} = \begin{Bmatrix} F_{zs} \\ F_{zc} \\ F_{ys} \\ F_{yc} \end{Bmatrix}. \tag{4.7}$$

4.2 The Newton's Method and Newton's Method with Arc-Length Continuation

There are different approaches for the solution of nonlinear equations. Newton's Method is one of the methods used (Urroz, 2004) for the solution of nonlinear algebraic equation set. Consider the solution of system of equations with n unknowns.

$$R(x) = \begin{bmatrix} R_1(x_1, x_2, \ldots, x_n) \\ R_2(x_1, x_2, \ldots, x_n) \\ \vdots \\ R_n(x_1, x_2, \ldots, x_n) \end{bmatrix} = 0, \tag{4.8}$$

where

$$x = \begin{bmatrix} x_1 \\ x_2 \\ \vdots \\ x_n \end{bmatrix}. \tag{4.9}$$

Newly approximated root can be written as;

$$x_{n+1} = x_n - J^{-1} R(x_n), \tag{4.10}$$

where J is called Jacobian matrix and defined as;

$$J = \frac{\partial(R_1, \mathrm{R}_2, \cdots, \mathrm{R}_n)}{\partial(x_1, x_2, \cdots, x_n)} = \begin{bmatrix} \frac{\partial R_1}{\partial x_1} & \frac{\partial R_1}{\partial x_2} & \cdots & \frac{\partial R_1}{\partial x_n} \\ \frac{\partial R_2}{\partial x_1} & \frac{\partial R_2}{\partial x_2} & \cdots & \frac{\partial R_2}{\partial x_n} \\ \vdots & \vdots & \ddots & \vdots \\ \frac{\partial R_n}{\partial x_1} & \frac{\partial R_n}{\partial x_2} & \cdots & \frac{\partial R_n}{\partial x_n} \end{bmatrix}. \tag{4.11}$$

In the solution of the some systems, determinant of Jacobian matrix becomes zero or very small and because of that it is not possible to calculate the inverse of Jacobian. At these times Newton's Method becomes insufficient for the solution of these systems. In these situations Newton's Method with Arc-Length Continuation is preferred by many to solve the problem (Ender Cigeroglu & Samandari, 2012; Ewins, 2000; Ferreira & Serpa, 2005). In the Newton's Method with Arc-Length Continuation, instead of frequency arc-length denoted by s is added to non-linear equation set as a path following parameter. s is the radius of a hypothetical sphere in which the next solution point is searched.

$$q = \begin{Bmatrix} x \\ \omega \end{Bmatrix}. \tag{4.12}$$

Here q is the new vector of unknowns.

$$(x_k - x_{k-1})^2 + (\omega_k - \omega_{k-1})^2 = s^2, \tag{4.13}$$

$$\Delta x_k = x_k - x_{k-1}, \tag{4.14}$$

$$\Delta \omega_k = \omega_k - \omega_{k-1}, \tag{4.15}$$

$$\Delta q_k = \begin{Bmatrix} \Delta x_k \\ \Delta \omega_k \end{Bmatrix} = q_k - q_{k-1}, \tag{4.16}$$

$$h\left(x_k, \omega_k\right) = \Delta q_k{}^T \Delta q_k - s^2 = 0, \tag{4.17}$$

$$q_{i+1} = q_i - \begin{bmatrix} \dfrac{\partial R\left(x,\omega\right)}{\partial x} & \dfrac{\partial R\left(x,\omega\right)}{\partial \omega} \\ \dfrac{\partial h\left(x,\omega\right)}{\partial x} & \dfrac{\partial h\left(x,\omega\right)}{\partial \omega} \end{bmatrix}^{-1} \begin{Bmatrix} R\left(x,\omega\right) \\ h\left(x,\omega\right) \end{Bmatrix}. \tag{4.18}$$

In some cases it is possible to have convergence problems. In these cases at every iteration step relaxation is applied (Cigeroglu & Ozguven, 2006).

$$q^*_{i+1} = \lambda q_{i+1} + \left(1-\lambda\right) q_i, \tag{4.19}$$

where λ is weighting factor which have a value between 0 and 2. If a non-convergent system is desired to be made convergent the value of λ is employed between 0 and 1. If the convergence of already convergent system is desired to be accelerated, the value of λ is employed between 1 and 2.

CHAPTER 5

CASE STUDIES

5.1 Case Studies for One Dimensional Macro Slip Friction Model

In this part, case studies covers the shaft-damper assemblies in which dry friction dampers are modeled by using one dimensional macro slip friction model with constant normal load. Example assembly is given in Fig. 17 where the system is excited by the unbalance located on the shaft. Parameters used are given in Table 1.

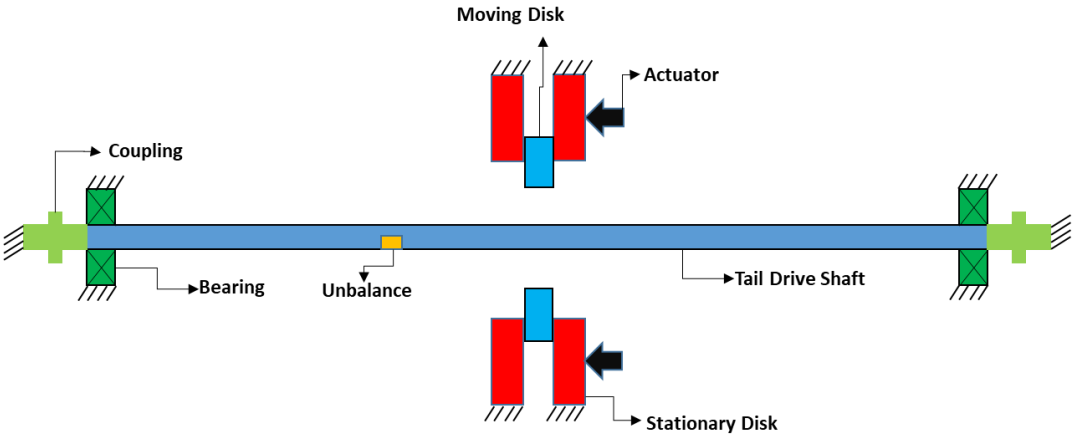

Fig. 17 Tail Shaft Assembly

Table 1 Parameters used

Parameter	Numerical Value
L [m]	3
D_o [m]	0.09
D_i [m]	0.07
E [GPa]	68.9
ρ [kg/m^3]	2700
k [N/m]	10^8
k_t [Nm/rad]	10^3
k_d [N/m]	10^6
ζ	0.02
me_1 [$kg \cdot m$]	10^{-3}
me_2 [$kg \cdot m$]	0.5×10^{-3}

where me_1 and me_2 are unbalances, D_o and D_i are outer and inner diameter of the shafts, k and k_t are the stiffness of bearings and couplings attached to shaft . External forcing is defined as $me\omega^2$. For this case study set, just one unbalance, me_1 , is used. In this case study external forcing is;

$$f_z(\mathrm{t}) = \mathrm{me}_1 w^2 \cos(wt) \qquad (5.1)$$

In the case study whose results are given in Fig. 18 both damper and unbalance are located on the midpoint of the shaft and effect of slip force, μN , on the maximum vibration amplitude of the shaft around its first critical speed is investigated. Obtained results are taken from the midpoint of the shaft. It is observed from the results that increasing slip load decreases the vibration amplitude until a certain point where further increase in the slip force results in an increase in the maximum vibration amplitude. Moreover, as the slip load increases, resonance frequency of the tail drive shaft system also increases which is due to the increased stiffness effect of the dry friction damper. After a point, friction damper system enters to fully stuck

state and it behaves like a permanent linear spring element and further increase of the slip force does not affect the vibration amplitude of the shaft. In Fig. 19 optimal curve and frequency shift curve of the same system is given in order to support the results of the previous study. From these results, it can be concluded that there is an optimum slip load which minimizes the vibration amplitude.

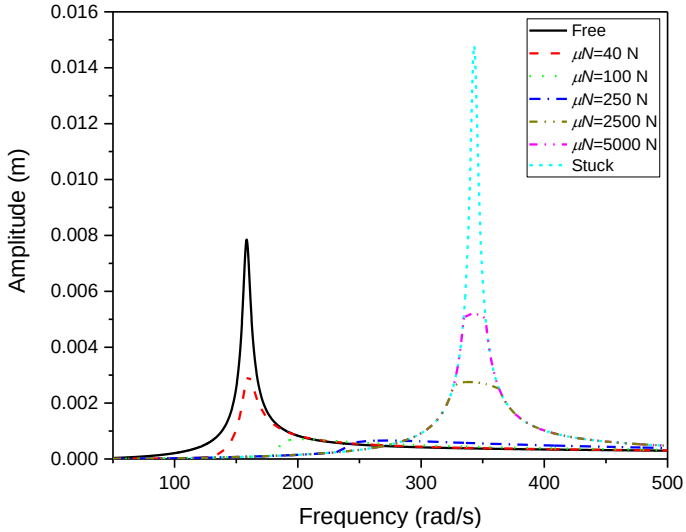

Fig. 18 Displacement amplitude of the midpoint vs. frequency plot as a function of slip force (μN)

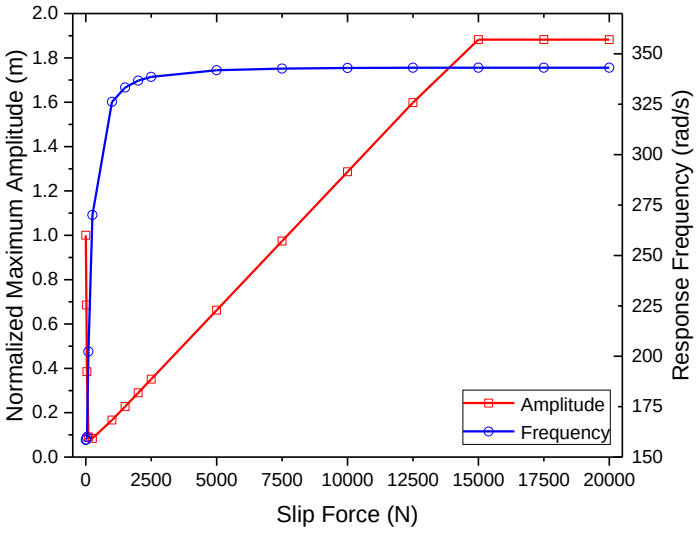

Fig. 19 Optimal and frequency shift curves

In the next case study whose results can be seen in Fig. 20 , in order to see the effect of damper location on the system response, dry friction damper is attached on different locations on the shaft with constant optimum slip load. Unbalance is located on the midpoint of the shaft and the results which consist of the maximum vibration amplitude normalized with respect to the maximum vibration amplitude of the no damper case are taken again from the midpoint of the shaft. It is clearly seen that the optimum damper location for the first vibration mode is the midpoint of the shaft where the highest amplitude of the first mode is expected. In addition to these, it should be noted that it is not possible to locate the damper on the exact middle section of the shaft but as can be seen from the graph small deviations does not affect the performance of the damper.

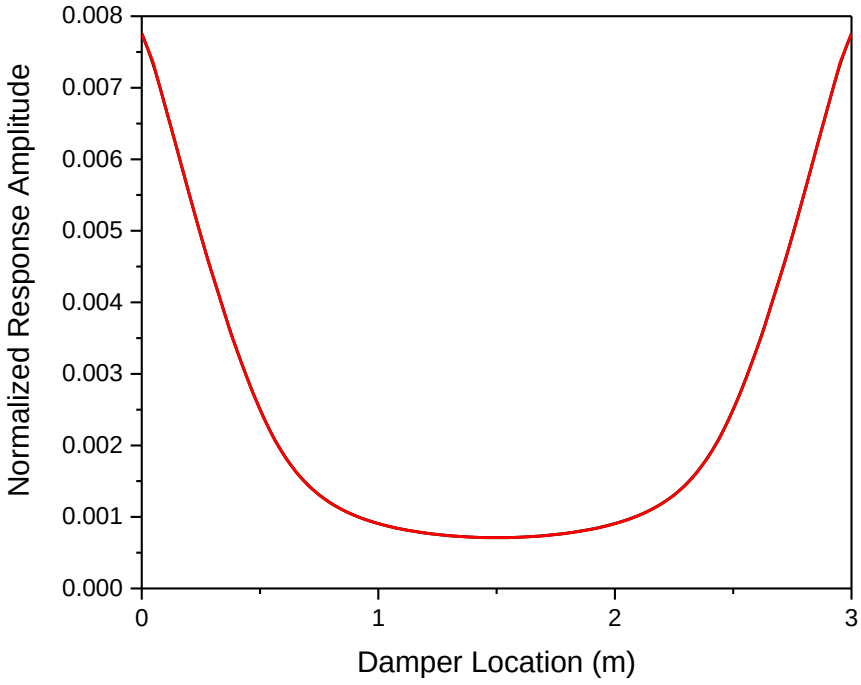

Fig. 20 Effect of damper location on the maximum vibration amplitude

In the next two case studies, it is assumed that shaft is rotating above the second natural frequency. In order to see the second mode, unbalance is moved to $0.25L$ and results are taken again from that point. In the case study presented in Fig. 21, damper is located at the midpoint of the shaft and it is seen that although the damper is able to damp vibrations around the first mode, it is ineffective around the second mode. This is due to the fact that the damper is located on the nodal point of the second mode. In the other case study presented in Fig. 22, damper is moved from the midpoint to $0.25L$. It is observed from these results that in this case, vibrations around the second mode are as well damped out. It can be concluded that if more than one mode is required to be damped, optimum damper location should be sought and nodal points should be avoided.

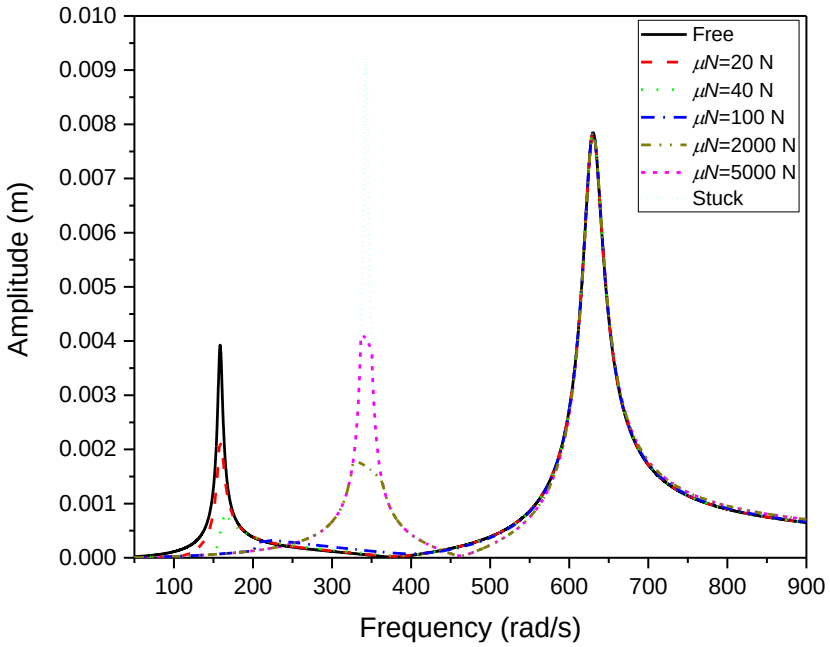

Fig. 21 Displacement amplitude of the midpoint vs. frequency plot as a function of slip force (μN)

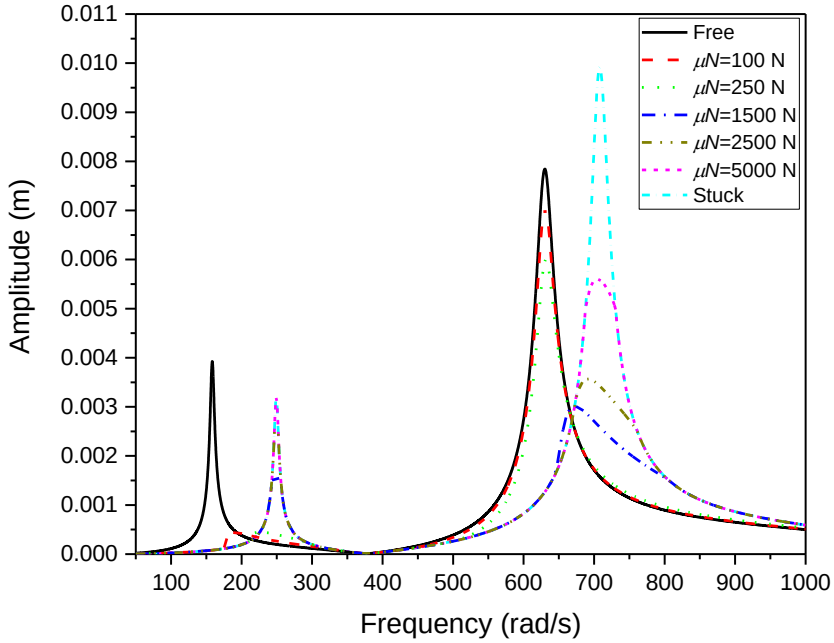

Fig. 22 Displacement amplitude of the midpoint vs. frequency plot as a function of slip force (μN)

In the next study given in Fig. 23, in order to see the importance of estimation of amount of unbalance, while holding the slip load constant, amount of unbalance is changed. Slip load is taken from the case study given in Fig. 18 as 250 N which is an optimum value for 10^{-3} N unbalance. In order to see the effect, maximum vibration amplitude normalized with respect to maximum vibration amplitude of the corresponding linear case is plotted. From the results, it is seen that for the other unbalance values efficiency of damper decreases and every slip load value is unique for its corresponding unbalance value. It can be said that effectiveness of the damper depends on the accurate estimation of the amplitude of external forcing which is unbalance.

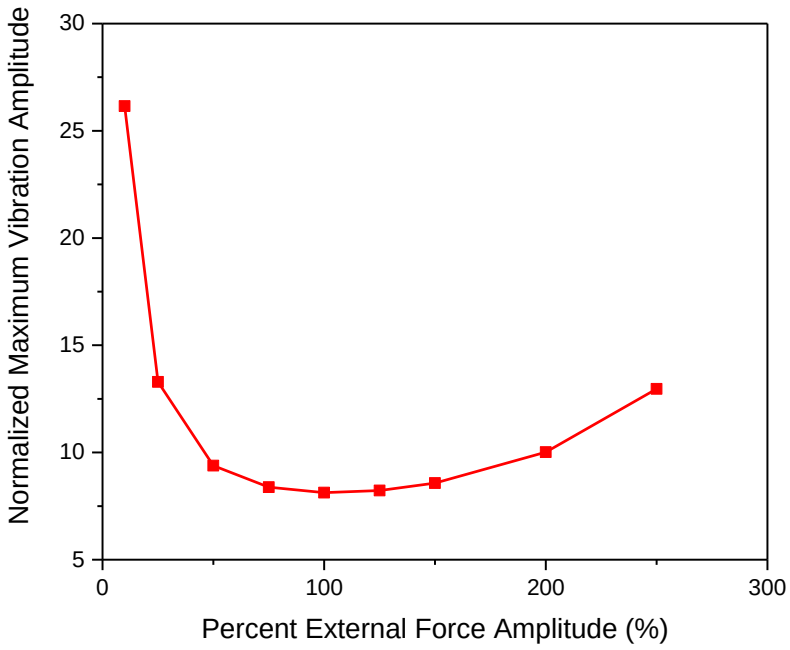

Fig. 23 Effect of amplitude variation of external forcing

5.2 Case Studies for One-Dimensional Macroslip Friction Model with Gap

In this part, case studies covers the shaft-damper assemblies in which dry friction dampers are modeled by using one dimensional dry friction macro slip model with gap. Example assembly is given in Fig. 24 where the system is excited by the unbalance located on the shaft. Used parameters are given in Table 1. Additionally $L_d = 0.5L$ and $L_f = 0.5L$. For this case study set, just one unbalance, me_1, is used. In this case study external forcing is;

$$f_z(\mathrm{t}) = \mathrm{me}_1 w^2 \cos(wt) \tag{5.2}$$

Dry friction damper with gap is attached on the helicopter tail shaft in order to suppress the vibrations resulting from passing from the resonance region. There are three main parameters affecting the behavior and the performance of the dry friction damper. These parameters are slip force, tangential contact stiffness and amount of gap. Several case studies are performed in order to examine the effects of these parameters.

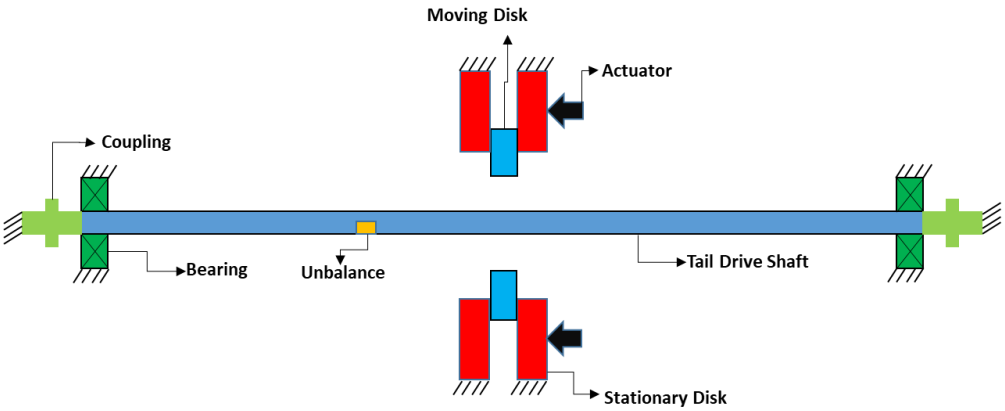

Fig. 24 Tail shaft assembly

In order to see the effect of slip force same system is run with different slip force values. From the results given in Fig. 25 and Fig. 26, it is seen that when the slip force is increased, amount of damping decreases until a point. After that optimum point extra increase in the slip force causes vibration amplitude to increase again. In addition to this, amount of slip force causes shift in the resonance frequency. The reason of the frequency shift is the increased stiffness effect of dry friction damper. After some time it becomes stuck and the damper behaves like a linear piece wise spring attached on the shaft. Further increase of the slip force does not affect the vibration amplitude anymore. From the optimal curve given in Fig. 26, it can be concluded that friction damper works properly at the right of the optimum slip force in order to eliminate the uncertainties in slip force and excitation amplitude.

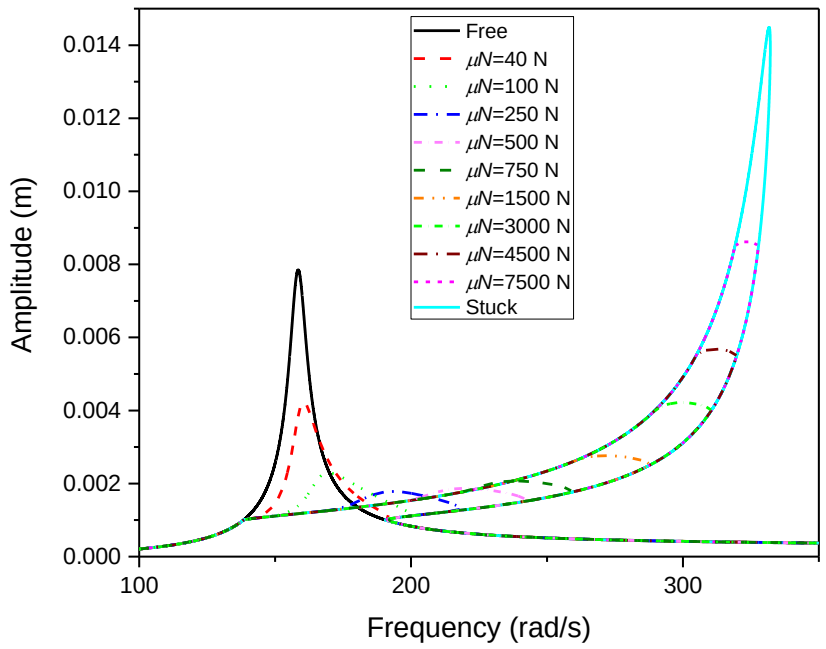

Fig. 25 Displacement amplitude of the midpoint vs. frequency plot as a function of slip force (μN) ($h = 0.001\,\text{m}$, $k_d = 10^6\,\text{N/m}$)

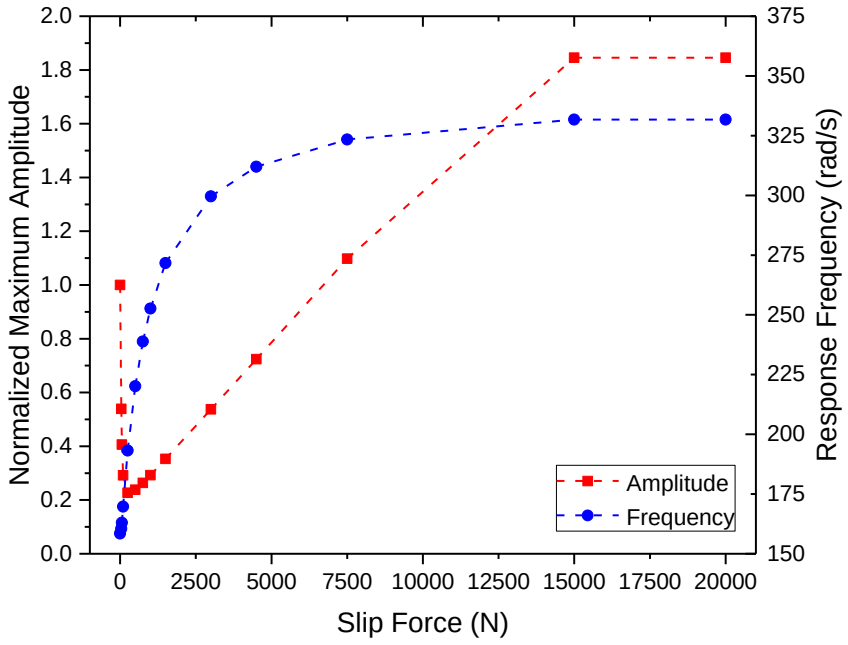

Fig. 26 Optimal and frequency shift curves ($h = 0.001\,\text{m}$, $k_d = 10^6\,\text{N/m}$)

In order to study the effect of tangential contact stiffness same system defined above is run with dry friction damper having different tangential contact stiffness values. Results are given in Fig. 27-Fig. 35. From the results it is seen that the biggest effect of the tangential contact stiffness change is on the amount of frequency shift. Larger k_d values cause larger frequency shifts. It is a fact that because of the unbalance, at higher speeds amplitude gets higher. In addition to these, optimum slip force region changes with k_d . For small k_d values optimum slip force region is relatively narrow while for the large k_d values region is wider. Sometimes during the operation it is not possible to provide constant slip force because of the factors like wear. So it is feasible to have larger optimum regions. However, excessive frequency shift can cause the operational speed to approach to the resonance frequency in the case of stuck.

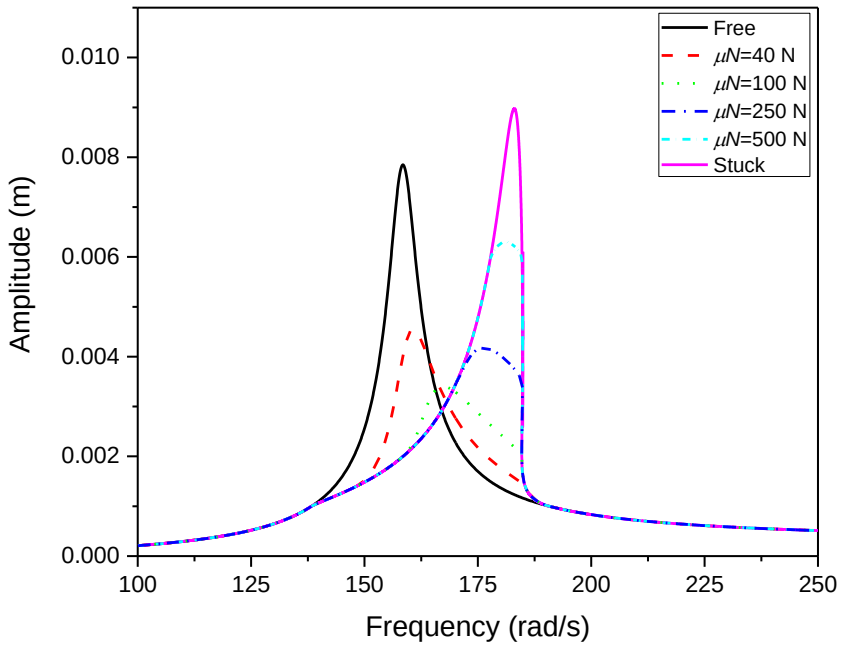

Fig. 27 Displacement amplitude of the midpoint vs. frequency plot as a function of slip force (μN) ($h = 0.001\,\text{m}$, $k_d = 10^5\,\text{N/m}$)

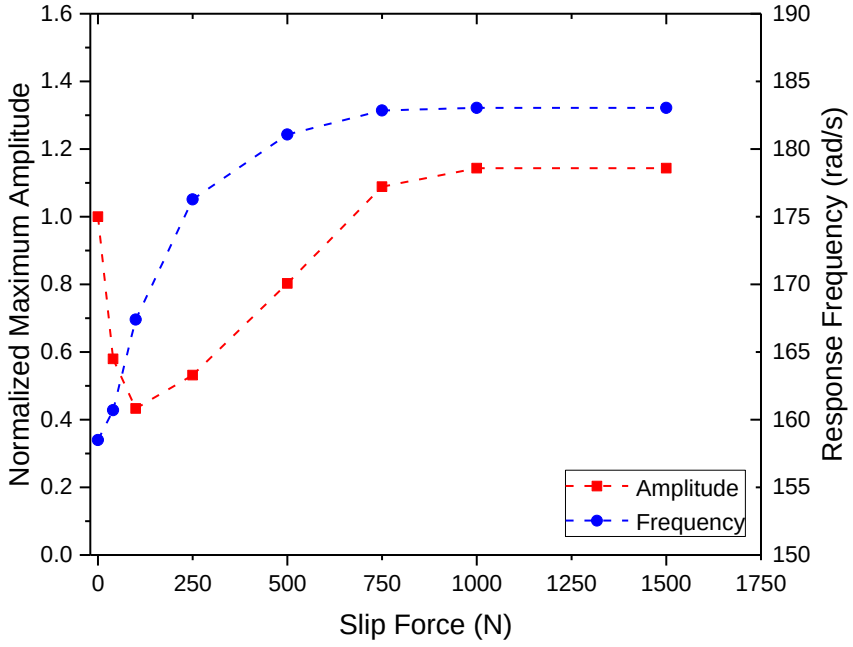

Fig. 28 Optimal and frequency shift curves ($h = 0.001\,\text{m}$, $k_d = 10^5\,\text{N/m}$)

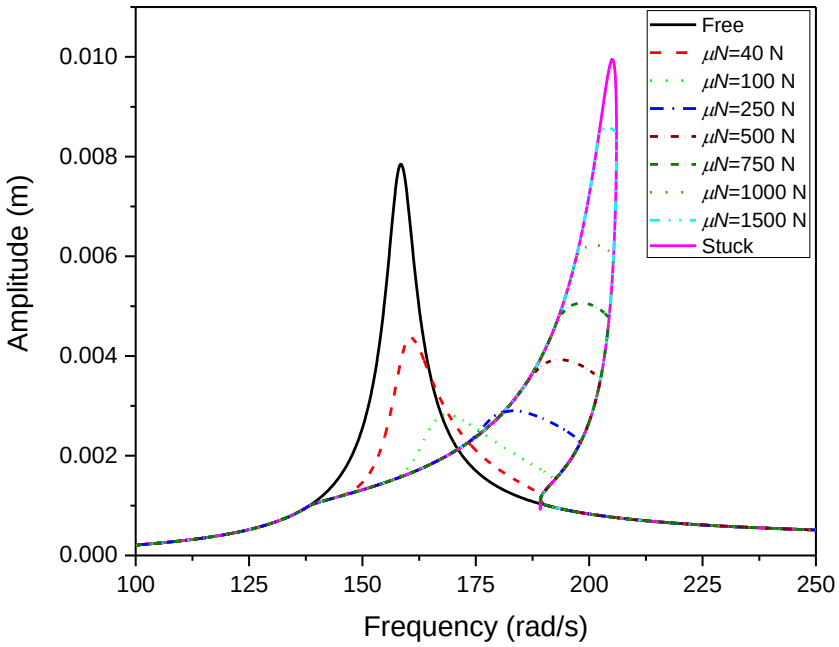

Fig. 29 Displacement amplitude of the midpoint vs. frequency plot as a function of slip force (μN) ($h = 0.001\,\text{m}$, $k_d = 2\times10^5\,\text{N/m}$)

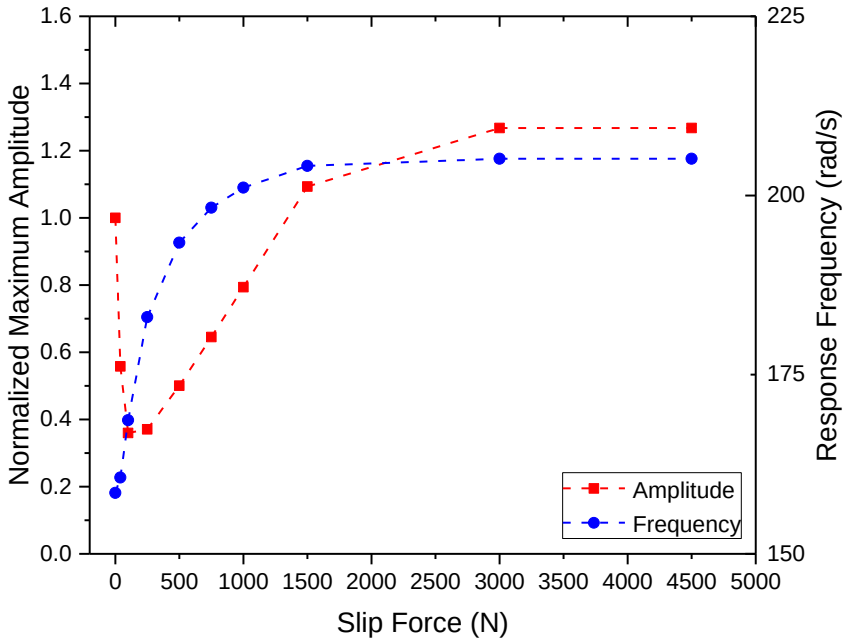

Fig. 30 Optimal and frequency shift curves ($h = 0.001\,\text{m}$, $k_d = 2\times10^5\,\text{N/m}$)

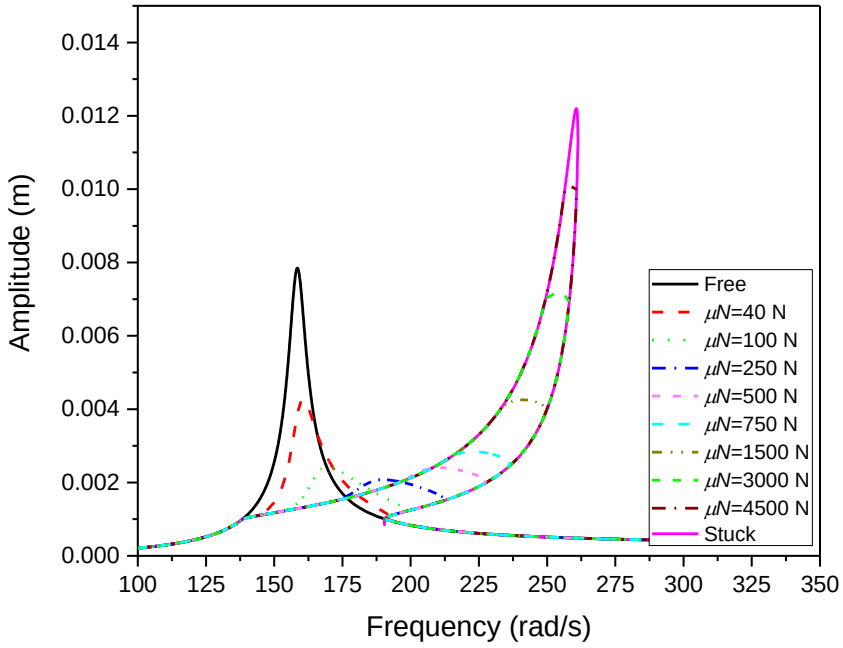

Fig. 31 Displacement amplitude of the midpoint vs. frequency plot as a function of slip force (μN) ($h = 0.001\,\text{m},\ k_d = 5\times10^5\,\text{N/m}$)

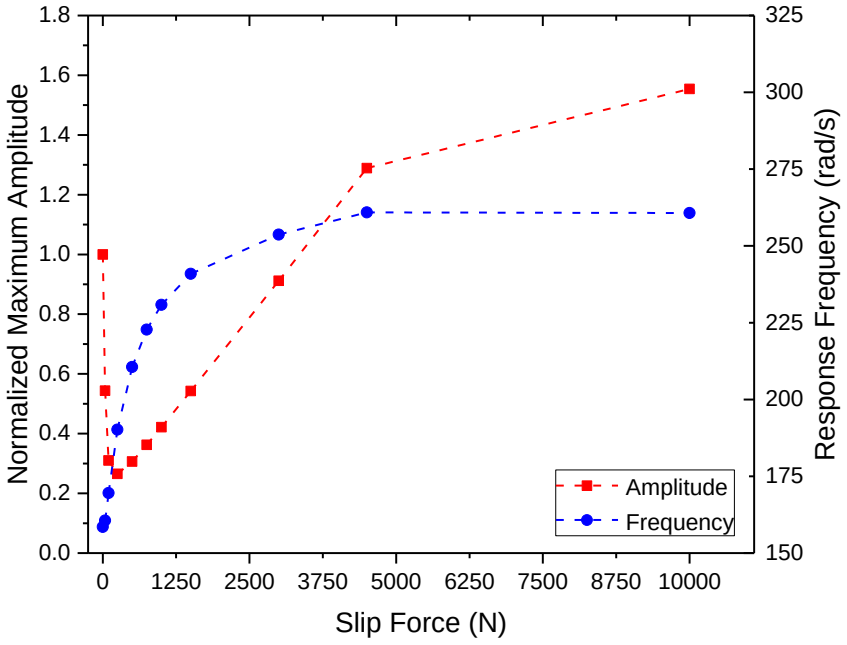

Fig. 32 Optimal and frequency shift curves ($h = 0.001\,\text{m},\ k_d = 5\times10^5\,\text{N/m}$)

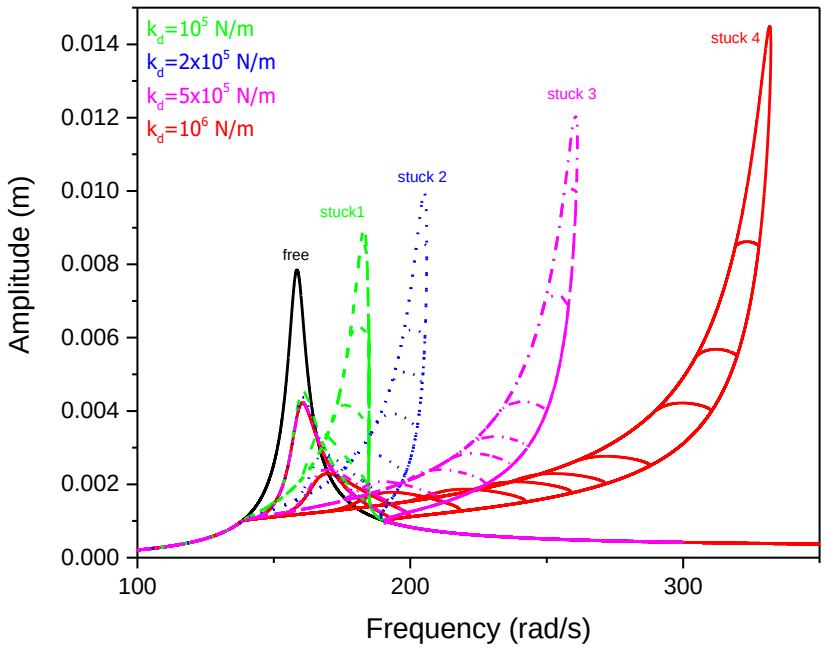

Fig. 33 Displacement amplitude of the midpoint vs. frequency - effect of tangential contact stiffness ($h = 0.001$ m)

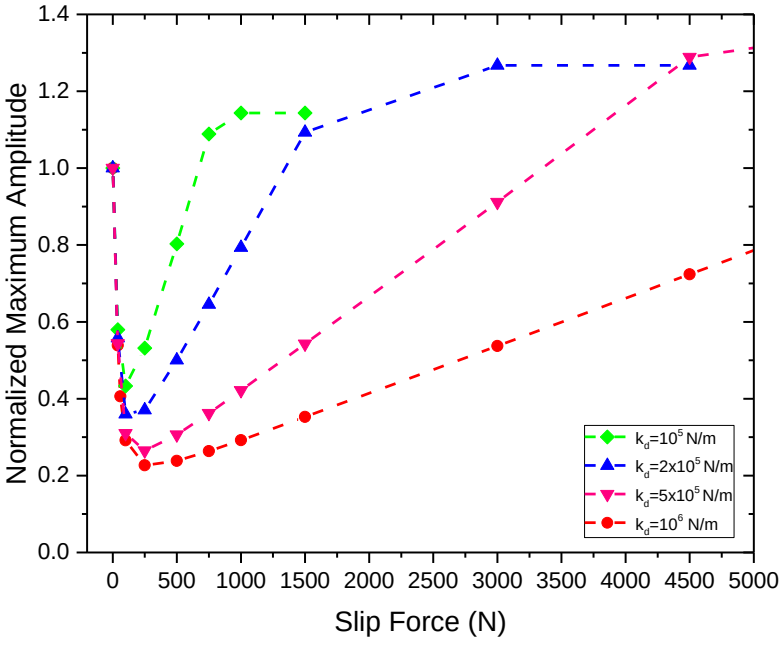

Fig. 34 Optimal curves ($h = 0.001$ m)

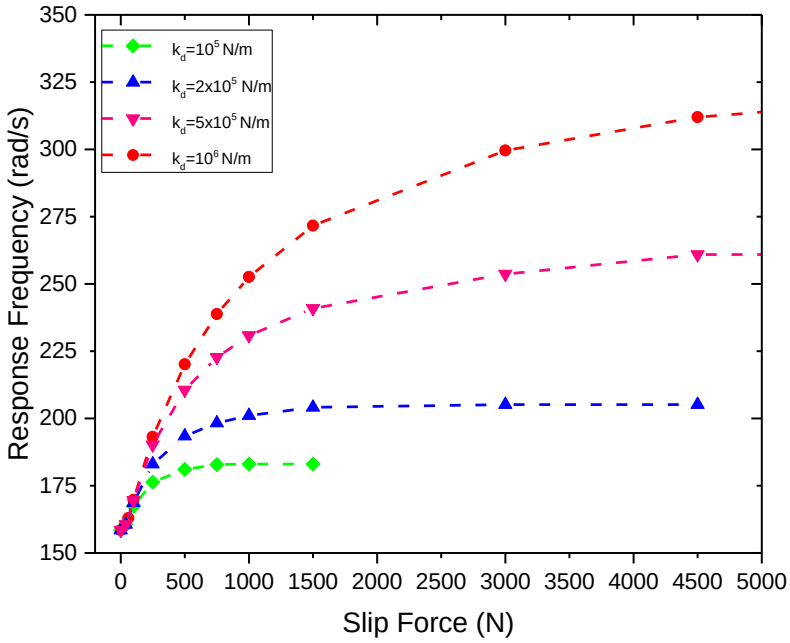

Fig. 35 Frequency shift curves ($h = 0.001$ m)

In the case study whose results are given in Fig. 36, vibration amplitudes of the shaft without any damper on it are compared with the vibration amplitudes of the shaft with damper on it. Amplitudes are taken for different external force values. It is seen that, change in the external forcing directly affect the damped vibration amplitudes, but for the system with higher k_d value this effect is lower. Performance of the damper is conserved for the high k_d value system. Although, higher k_d value seems more effective, it should be noted that higher k_d values causes higher frequency shift. This result supports the results of the previous case studies.

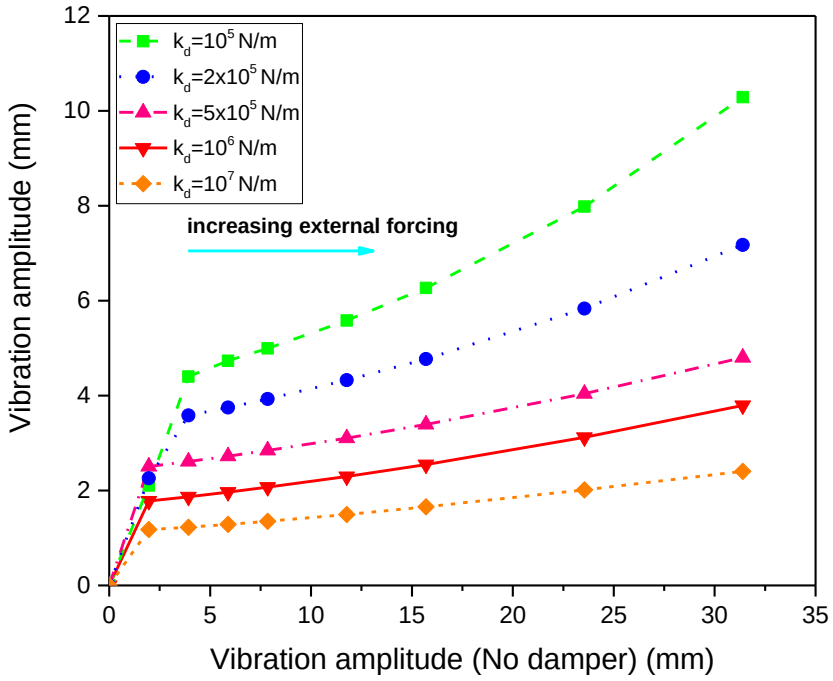

Fig. 36 Performance curve

In the third case study, the same system is studied for different values of gap. In Fig. 37, displacement amplitude of the midpoint of shaft as a function of frequency is given for system having a dry friction damper with and without a gap is given. It is seen that dry friction damper without a gap performs better than a friction damper with a gap, which is an expected result. However, reduction in vibration amplitude is not the only parameter that affects the design process. If a friction damper without a gap is used, it needs to work continuously during the operation which results in increased wear of the damper surfaces. This decreases the reliability of the damper and causes increased maintenance downtimes which is not preferred in aerospace applications. Moreover, since the damper works continuously, the shaft rotating inside the damper creates a friction torque which causes unnecessary energy loss. By introducing a gap to the damper it is possible to avoid all these negative effects and prevent excessive vibration amplitudes. It should also be noted that high vibration amplitudes are obtained when the shaft is speeding up or slowing down for supercritical shafts when the rotational speed is coincides with the critical speed

of the system. Therefore, friction dampers are not required to work continuously; instead, they are only necessary during the time short duration of time in speeding up or slowing down.

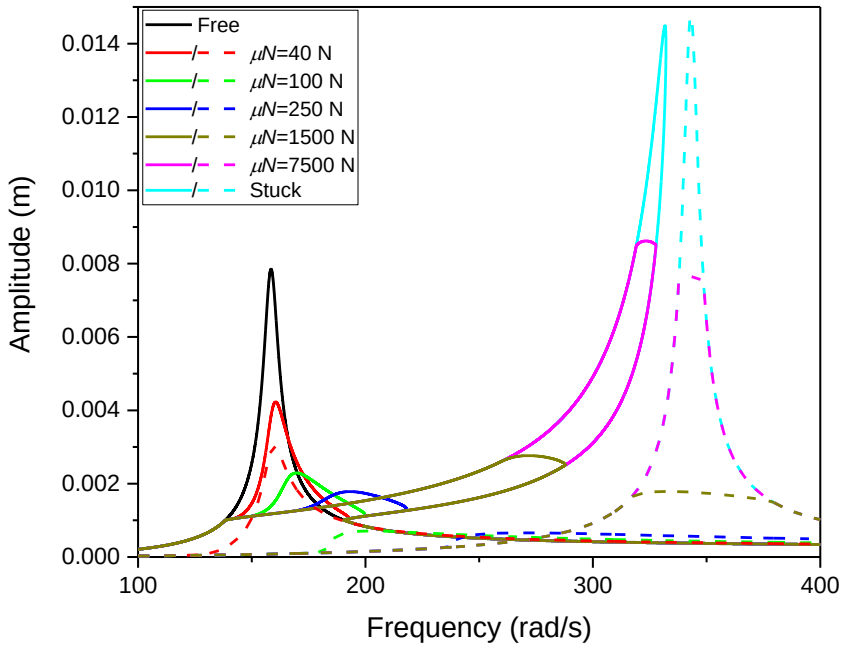

Fig. 37 Comparison of effect of amount of gap on displacement amplitude (solid lines: $h = 0.001\,\text{m}$; dashed lines: $h = 0\,\text{m}$, $k_d = 10^6\,\text{N/m}$)

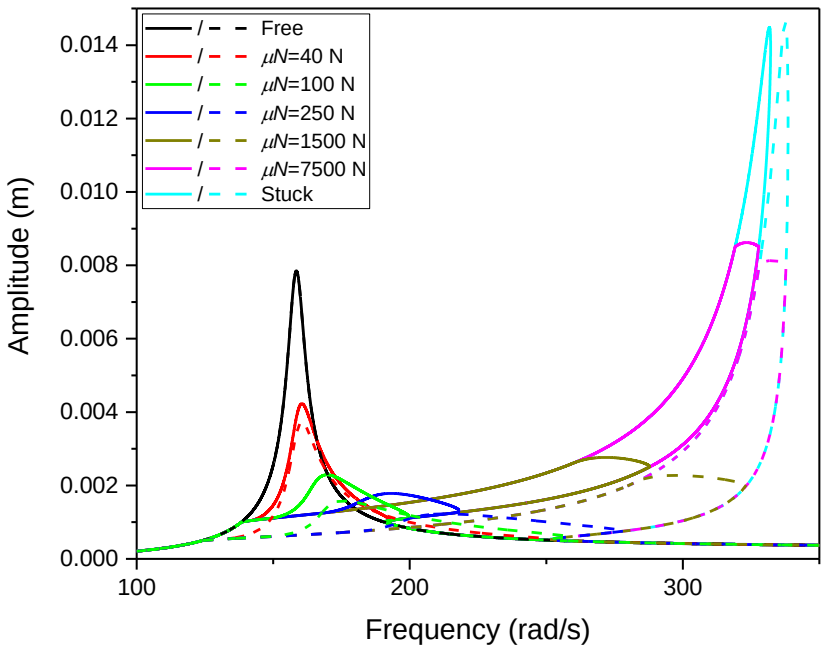

Fig. 38 Comparison of effect of amount of gap on displacement amplitude (solid lines: $h = 0.001\,\text{m}$; dashed lines: $h = 0.0005\,\text{m}$, $k_d = 10^6\,\text{N/m}$)

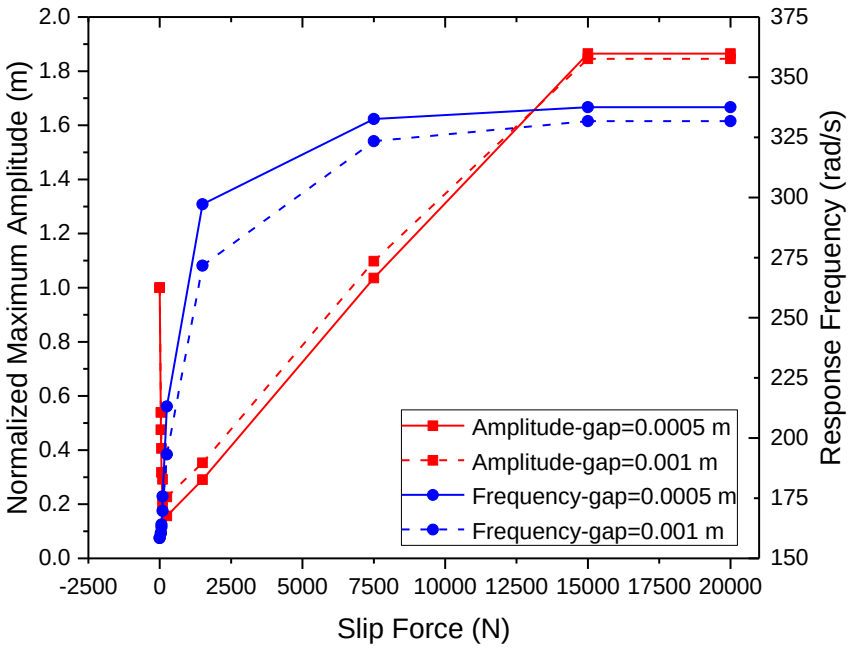

Fig. 39 Optimal and frequency shift curves ($k_d = 10^6\,\text{N/m}$)

In Fig. 38 two different gap values are considered. As expected, smaller gap value results in more reduction in the vibration amplitude but the difference is not significant. This can be easily observed in Fig. 39, where the optimal and frequency shift curves are given. Proper gap value can be obtained by considering the allowable vibration amplitude and maintenance requirements.

5.3 Case Studies for Two-Dimensional Macroslip Friction Model-Elliptical Motion

In this part case studies covers the shaft-damper assemblies in which dry friction dampers are modeled by using two dimensional macro slip model. Example assembly is given in Fig. 40. Parameters used are given in Table 1. In order to see elliptical motion, the system is excited by two unbalances located on the shaft with 90 degrees phase difference. In this case study external forcing is;

$$f_z(\mathrm{t}) = \mathrm{me}_1 w^2 \cos(wt) + me_2 w^2 \sin(wt) \tag{5.3}$$

$$f_y(\mathrm{t}) = \mathrm{me}_1 w^2 \sin(wt) + me_2 \mathrm{w}^2 \cos(wt) \tag{5.4}$$

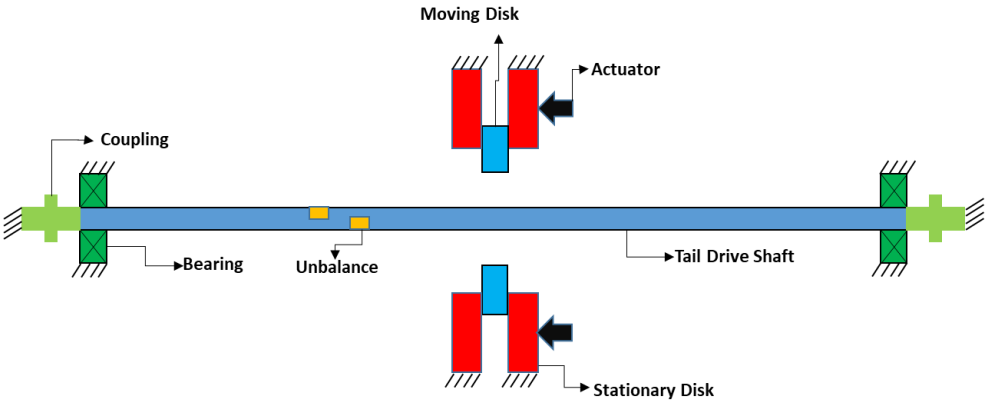

Fig. 40 Tail shaft assembly

In order to see the effect of dry friction damper on the first and second modes of the shaft, different case studies are performed. In the first case study whose results are given in Fig. 41, both damper and unbalance are located on the middle of the shaft. Two unbalances are located with phase difference in order to examine elliptical trajectory. In the second case study whose results are given in Fig. 42 both damper and unbalances are moved to $0.25L$ to be able to examine the second mode. From the results it is seen that when the slip force is increased, amount of damping decreases until a point. After that optimum point extra increase in the slip force causes vibration amplitude to increase again. In addition to this, amount of slip force causes shift in the resonance frequency. The reason of the frequency shift is the increased stiffness effect of dry friction damper. After some time it becomes stuck. Further increase of the slip force does not affect the vibration amplitude anymore. it can be concluded that friction damper works properly at the right of the optimum slip force in order to eliminate the uncertainties in slip force and excitation amplitude.

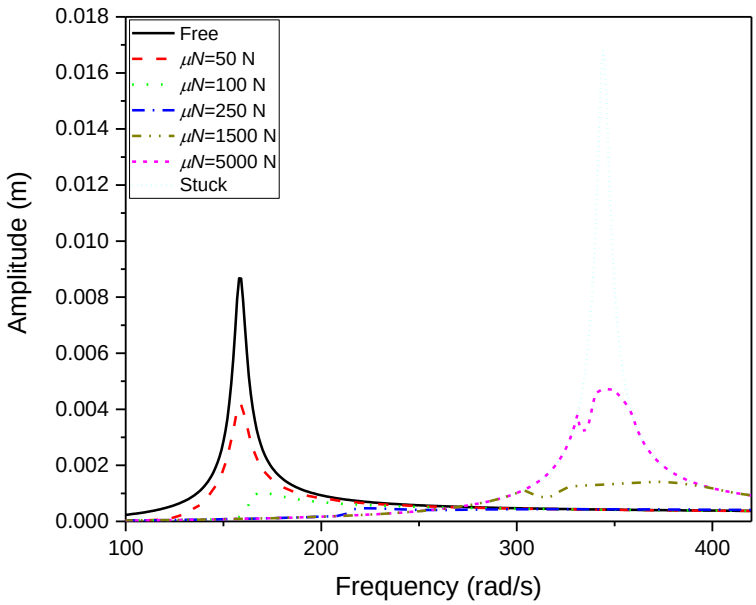

Fig. 41 Displacement amplitude vs. frequency plot as a function of slip force (μN)

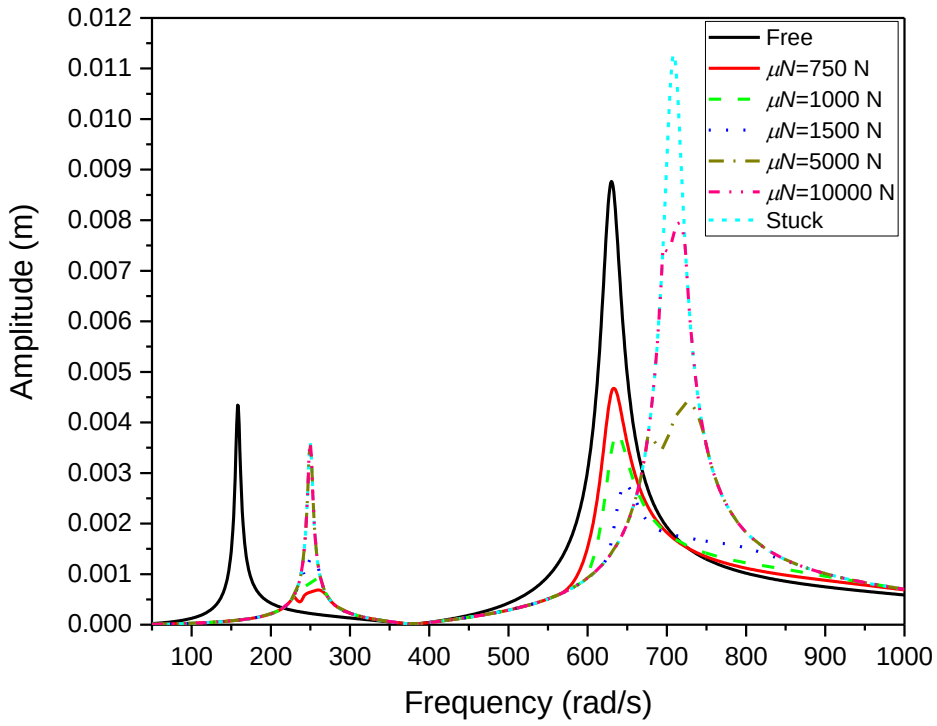

Fig. 42 Displacement amplitude vs. frequency plot as a function of slip force (μN)

Another case study is performed in order to compare the different models for the rotating shaft with dry friction damper attached on it. Both damper and unbalances are located onto the middle of the shaft and the results are taken from that point. There is a phase difference between the unbalances which creates the elliptical trajectory. First model is the two dimensional macro slip friction model. In the second one instead of using two dimensional model , two one dimensional friction elements are combined. In the third model, again two one dimensional friction elements are combined with additional coordinate transformation which is applied in the two dimensional macro slip friction model(E Cigeroglu et al., 2007; Cigeroglu et al., 2009). Illustration of third model and related coordinate transformation axis is given in Fig. 43. One of the main reasons of seeking alternative method for the two dimensional model is that it is computationaly expensive becasue of the

ordinary differential equations which are solved numerically. From the frequency vs amplitude graph given in Fig. 44 and from the optimal curve given in Fig. 45, it can be said that two alternative methods can be used instead of two dimensional model if the computation time is an important concern. However it is better use the two one dimensional friction element model with coordinate transformation because it gives closer results to the two dimensional model around optimum region.

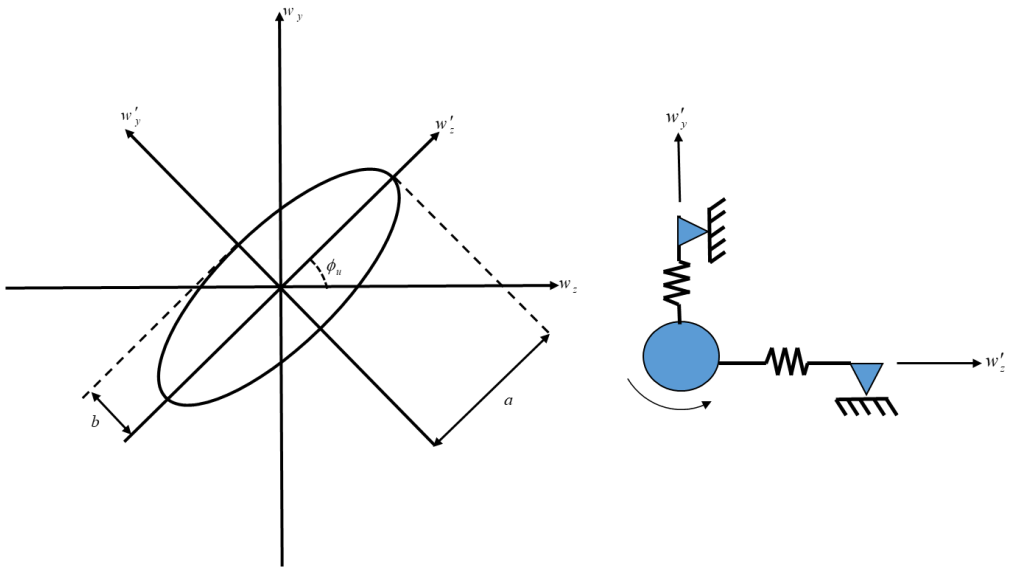

Fig. 43 Coordinate transformation axis and illustration of 2 1D friction elements with transformation

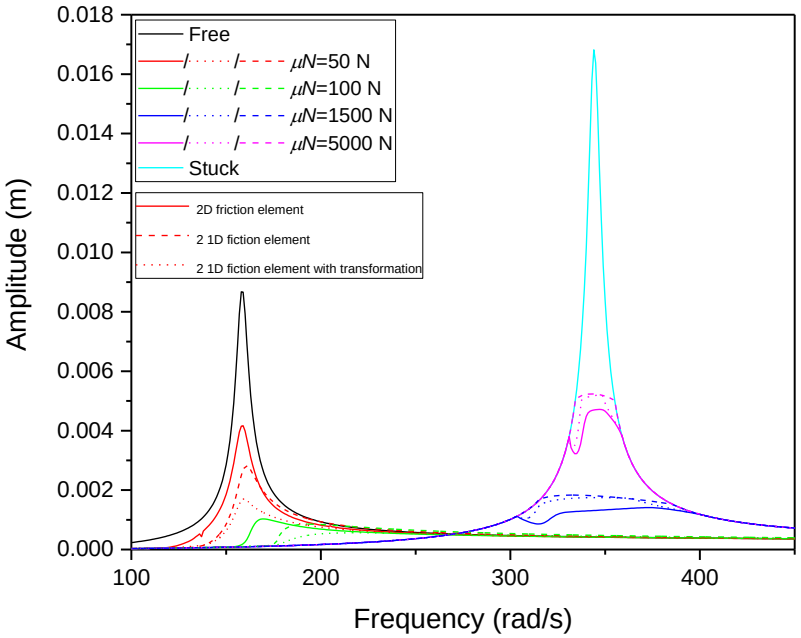

Fig. 44 Comparison of efficiency of different models

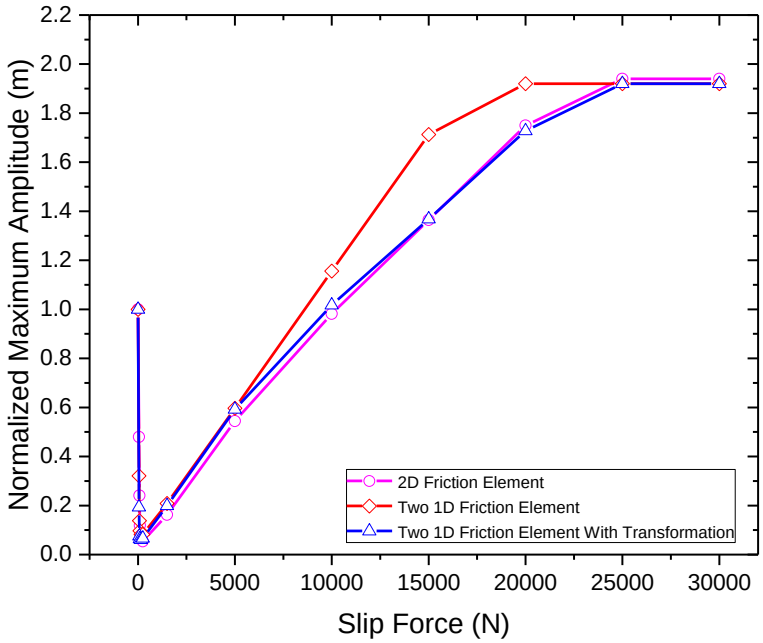

Fig. 45 Optimal curves

5.4 Case Studies for Two-Dimensional Macroslip Friction Model-Circular Motion

In this part case studies covers the shaft-damper assemblies in which dry friction dampers are modeled by using two dimensional macro slip model with circular motion. Example assembly is given in Fig. 46 where the system is excited by an unbalance located on the shaft. Parameters used are given in Table *1*. For this case study set, just one unbalance, me_1, is used. In this case study external forcing is;

$$f_z(\mathrm{t}) = \mathrm{me}_1 w^2 \cos(wt) \tag{5.5}$$

$$f_y(\mathrm{t}) = \mathrm{me}_1 w^2 \sin(wt) \tag{5.6}$$

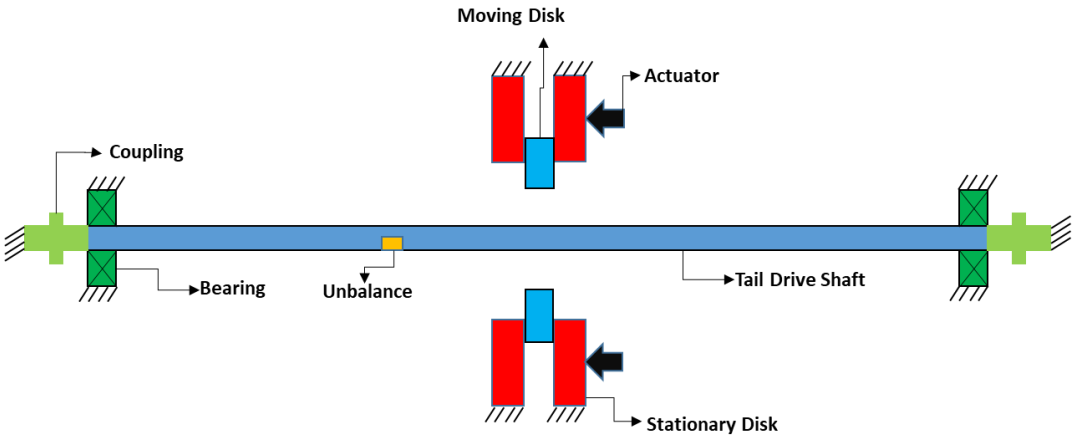

Fig. 46 Tail shaft assembly

In order to see the effect of dry friction damper on the first and second modes of the shaft following circular trajectory, different case studies are performed. In the first case study whose results are given in Fig. 47 and Fig. 48, both damper and unbalance are located on the middle of the shaft. Only one unbalance is attached in order to

examine circular trajectory. In the second case study whose results are given in Fig. 49, in order to examine the second mode and the effect of the damper on that mode both damper and unbalance is moved to $0.25L$. From the results it is seen that when the slip force is increased, amount of damping decreases until a point. After that optimum point extra increase in the slip force causes vibration amplitude to increase again. In addition to this, amount of slip force causes shift in the resonance frequency. The reason of the frequency shift is the increased stiffness effect of dry friction damper. After some time it becomes stuck and further increase of the slip force does not affect the vibration amplitude anymore. It can be said that with correct parameters dry friction dampers works properly.

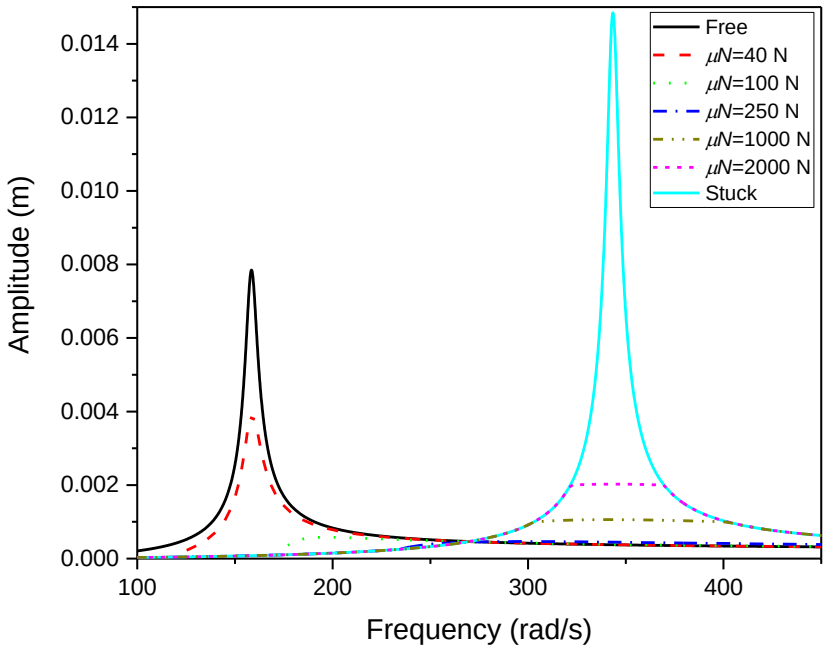

Fig. 47 Displacement amplitude vs. frequency plot as a function of slip force (μN)

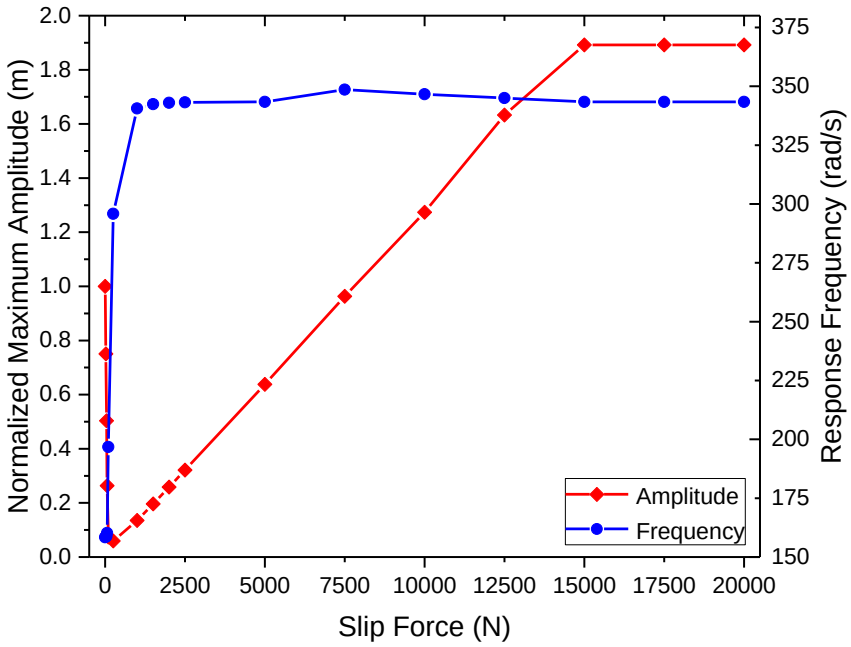

Fig. 48 Optimal and frequency shift curves

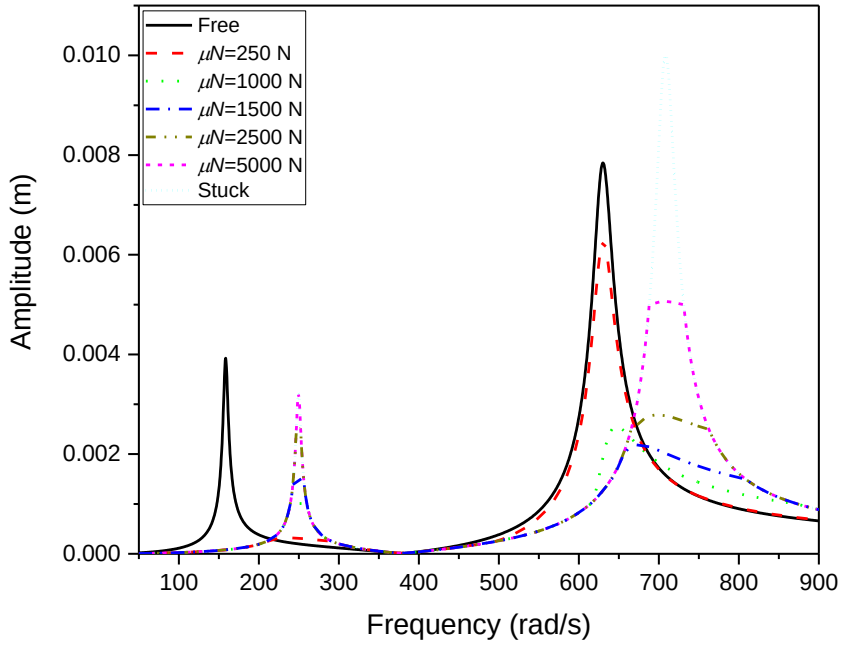

Fig. 49 Displacement amplitude vs. frequency plot as a function of slip force (μN)

Another case study is performed in order to compare the different models for the rotating shaft with dry friction damper attached on it. Both damper and unbalance are located on the middle of the shaft and the results are taken from that point. First model is the two dimensional macro slip friction model. As a second model instead of using two dimensional one, two one dimensional friction elements are combined. One of the main reasons of seeking alternative method for the two dimensional model is that it is computationaly more complex. From the frequency vs amplitude graph given in Fig. 50 both two models gives close results and it can be said that combination of two one dimensional friction elements can be used instead of two dimensional macro slip friction model.

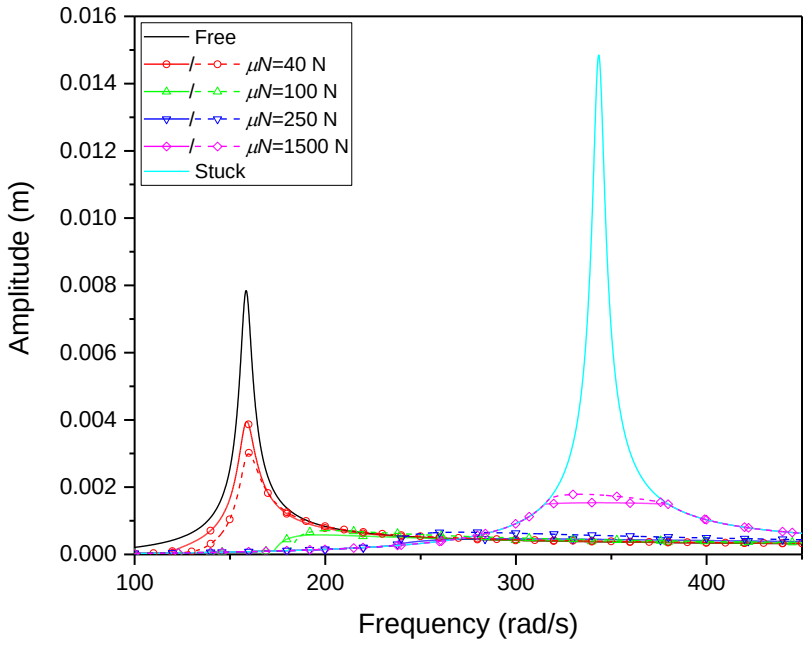

Fig. 50 Comparison of efficiency of different models (solid lines: 2D friction element; dashed lines: 2 1D friction element)

CHAPTER 6

DISCUSSION AND CONCLUSION

6.1 Conclusion

In this study, vibration reduction of supercritical helicopter tail drive shaft by utilizing dry friction dampers is studied. The tail drive shaft is modeled by Euler-Bernoulli beam theory supported by springs at both ends which represent the bearings and couplings used. . In order to derive the equation of motion Hamilton's Principle is used. The partial differential equation of motion obtained is discretized by using Galerkin's Method with multiple trial functions and the resulting nonlinear ordinary differential equations are converted into a set of nonlinear algebraic equations by using Harmonic Balance Method. These resulting nonlinear algebraic equations are solved by using Newton's Method and Newton's Method with Arc-Length Continuation.

In order to model dry friction dampers mathematically different friction models are used. Two models are taken from the literature; one dimensional macroslip friction model with constant normal load and two dimensional macroslip friction model with constant normal load. Moreover, In order to examine the systems having circular trajectory sub-model of the two dimensional macroslip friction model with constant normal load is used. Apart from these two models to be able to study the systems having gap between the interfaces, a new model, one-dimensional macroslip friction model with gap, is developed by adding gap element to one dimensional macroslip friction model. General conditions for stick, slip and contact and no contact states

are developed and transition angles for simple harmonic motion are obtained analytically

Several case studies are performed in order to see the effect of dry friction dampers on the helicopter tail shaft vibrations. As a general conclusion it can be said that with correct parameters dry friction dampers are able to damp the excessive vibrations of the tail shaft while passing from the resonance regions. Two important parameters are amount of slip force and the location of the damper. Increasing amount of slip force on the damper decreases the vibration amplitude, but after a point vibration amplitude increases again with additional frequency shift as a result of the increasing stiffening effect. It is obvious that with optimum slip force value, damper fulfills its duty successfully. In a practical way, considering the parameter uncertainties, it is concluded that optimum slip force value should defined at the right of optimum point in the optimal curves. It should be noted that, optimum slip force values are unique for specific external forcing value. Because of that estimation of the external forcing value is very important. Location of the damper is also crucial. If the shaft works just above the first natural frequency, it is better to locate the damper around the point where peak of the first mode is expected. If the shaft works above more than one natural frequencies, it is better to find the optimum location. In addition to this, if one specific mode is desired to be damped, nodal point of that mode must be avoided.

For the systems having dry friction dampers with gap, additional cases are studied. Amount of gap is an important parameter for these kind of systems. It is seen that adding gap to the damper decreases the performance of the damper. However, performance is not the only design parameter. Dampers with gap does not engage with the shaft continuously, they make contact with the shaft while passing from the resonance region. So it can be said that due to the gap introduced, life of the friction damper increases, unnecessary friction torque and shaft wear are eliminated, and maintenance downtimes are decreased. Due to the importance of maintenance in helicopter operations, it is feasible to use gapped dampers. It is observed that tangential contact stiffness is an important design parameter and according to the

optimal and performance curves obtained, dampers with higher contact stiffness values less sensitive to parameter uncertainties. Therefore, dry friction dampers with higher contact stiffness values should be preferred to have better friction damper performance.

Two dimensional macroslip models simulate the dampers successfully but they are computationally expensive. For the systems following elliptic trajectory, combination of two one dimensional friction elements with coordinate transformation can be used instead of two dimensional model if the computation time is an important concern. Both models give pretty close results around optimum region. Same results can be said for the systems following circular trajectory. Instead of two dimensional model, combination of two one dimensional elements can be used.

To sum up, it can be said that dry friction dampers are capable of reducing the vibrations of the tail shaft of a helicopter if correct parameters are chosen.

6.2 Future Works

In this study, reduction of vibrations of tail shaft systems of a helicopter by using dry friction dampers is examined. Dry friction dampers are modeled by using different friction models. While using Harmonic Balance Method single harmonic approach is used and in the future studies multi-harmonic approach can be used and effects of the harmonics can be examined.

In this study, in order to model the dry friction damper having gap, one dimensional macro slip friction model with gap is used. In the future, this model can be extended to two dimensional model.

REFERENCES

Al Sayed, B., Chatelet, E., Baguet, S., & Jacquet-Richardet, G. (2011). Dissipated energy and boundary condition effects associated to dry friction on the dynamics of vibrating structures. *Mechanism and Machine Theory*, *46*(4), 479–491. https://doi.org/10.1016/j.mechmachtheory.2010.11.014

Andersson, S., Söderberg, A., & Björklund, S. (2007). Friction models for sliding dry, boundary and mixed lubricated contacts. *Tribology International*, *40*(4), 580–587. https://doi.org/10.1016/j.triboint.2005.11.014

Bauchau, O. A., & Craig, J. I. (2009). *Structural Analysis With Applications to Aerospace Structures*. *Product Performance Evaluation with CAD/CAE* (Vol. 163). https://doi.org/10.1007/978-90-481-2516-6

Belash, T. (2015). Dry Friction Dampers in Quake-proof Structures of Buildings. *Procedia Engineering*, *117*, 397–403. https://doi.org/10.1016/j.proeng.2015.08.184

Bradfield, C. D., Roberts, J. B., & Karunendiran, R. (2016). Performance of an electromagnetic bearing for the vibration control of a supercritical shaft. In *Proceedings of the Institution of Mechanical Engineers, Part C: Journal of Mechanical Engineering Science* (Vol. 201, pp. 201–212).

Cameron, T. M., Griffin, J. H., Kielb, R. E., & Hoosac, T. M. (1990). An Integrated Approach for Friction Damper Design. *Journal of Vibration and Acoustics*, *112*(2), 175–182. https://doi.org/10.1115/1.2930110

Chen, J. J., & Menq, C. H. (2001). Periodic Response of Blades Having 3D Nonlinear Shroud Constraints. *Journal of Engineering for Gas Turbines and Power*, *123*(October), 901–909. https://doi.org/10.1115/99-GT-289

Chen, J. J., Yang, B. D., & Menq, C. H. (2000). Periodic Forced Response of Structures Having Three-Dimensional Frictional Constraints. *Journal of Sound and Vibration*, *229*(4), 775–792. https://doi.org/10.1006/jsvi.1999.2397

Cigeroglu, E., An, N., & Menq, C.-H. (2009). Forced Response Prediction of Constrained and Unconstrained Structures Coupled Through Frictional Contacts. *Journal of Engineering for Gas Turbines and Power*, *131*(2), 22505. https://doi.org/10.1115/1.2940356

Cigeroglu, E., An, N., & Menq, C. H. (2007). A microslip friction model with normal load variation induced by normal motion. *Nonlinear Dynamics*, *50*(3), 609–626. https://doi.org/10.1007/s11071-006-9171-4

Cigeroglu, E., An, N., & Menq, C. H. (2007). Wedge damper modeling and forced response prediction of frictionally constrained blades. In *Proceedings of the ASME Turbo Expo 2007, Vol 5* (pp. 519–528). https://doi.org/10.1115/GT2007-27963

Cigeroglu, E., Lu, W., & Menq, C. H. (2006). One-dimensional dynamic microslip friction model. *Journal of Sound and Vibration*, *292*(3–5), 881–898. https://doi.org/10.1016/j.jsv.2005.09.019

Cigeroglu, E., & Ozguven, H. N. (2006). Nonlinear vibration analysis of bladed disks with dry friction dampers. *Journal of Sound and Vibration*, *295*(3–5), 1028–1043. https://doi.org/10.1016/j.jsv.2006.02.009

Cigeroglu, E., & Samandari, H. (2012). Nonlinear free vibration of double walled carbon nanotubes by using describing function method with multiple trial functions. *Physica E: Low-Dimensional Systems and Nanostructures*, *46*, 160–173. https://doi.org/10.1016/j.physe.2012.09.016

Csaba, G. (1998). Forced Response Analysis in Time and Frequency Domains of a Tuned Bladed Disk With Friction Dampers. *Journal of Sound and Vibration*, *214*(3), 395–412. https://doi.org/10.1006/jsvi.1997.1513

Darlow, M. S., & Zorzi, E. S. (1978). Nonsynchronous Vibrations Observed in a Supercritical Power Transmission Shaft. In *Gas Turbine Conference & Exhibit& Solar Energy Conference* (pp. 1–8).

Den Hartog, J. P. (1930). Forced Vibrations with Combined Viscous and Coulomb Damping. *Philosophical Magazine Series 7*, *9*(59), 801–815.

Desmidt, H. A. (2009). Imbalance Vibration Suppression of a Supercritical Shaft

via an Automatic Balancing Device. *Journal of Vibration and Acoustics*, *131*(August 2009), 1–13. https://doi.org/10.1115/1.3025834

Ding, Q., & Chen, Y. (2008). Analyzing Resonant Response of a System with Dry Friction Damper Using an Analytical Method. *Journal of Vibration and Control*, *14*(8), 1111–1123. https://doi.org/10.1177/1077546307080246

Dostal, M., Roberts, J. B., & Holmes, R. (1977). THE EFFECT OF EXTERNAL DAMPING ON THE VIBRATION OF FLEXIBLE SHAFTS SUPPORTED ON OIL-FILM BEARINGS. *Journal of Sound and Vibration*, *51*, 69–87.

Dowell, E. H., & Schwartz, H. B. (1983). Forced response of a cantilever beam with a dry friction damper attached, part I: Theory. *Journal of Sound and Vibration*, *91*(2), 255–267. https://doi.org/10.1016/0022-460X(83)90901-X

Dutt, J. K., & Nakra, B. C. (1996). Stability Characteristics of Rotating Systems with Journal Bearings on Viscoelastic Support, *31*(6), 771–779.

Dzygadlo, Z., & Perkowski, W. (2000). Nonlinear Dnamic Model For Flexural Vibrations Analysis Of A Supercritical Helicopter's Tail Rotor Drive Shaft. In *ICAS 2000* (p. 183.1-183.9).

Dzygadlo, Z., & Perkowski, W. (2002). Research on dynamics of a supercritical propulsion shaft equipped with a dry friction damper. *Aircraft Engineering and Aerospace Technology*, *74*(5), 447–454. https://doi.org/10.1108/00022660210442290

Erisen, Z. E., & Cigeroglu, E. (2012). Frequency Domain Optimization of Dry Friction Dampers on Buildings Under Harmonic Excitation. *Conference Proceedings of the Society for Experimental Mechanics Series*, *1*, 389–400. https://doi.org/10.1007/978-1-4614-2413-0

Ewins, D. J. (2000). The harmonic balance method with arc-length continuation in rotor / stator contact problems. *Journal of Sound and Vibration*, (August).

Ferreira, J. V., & Serpa, A. L. (2005). Application of the arc-length method in nonlinear frequency response. *Journal of Sound and Vibration*, *284*(1–2), 133–149. https://doi.org/10.1016/j.jsv.2004.06.025

Ferri, A. A. (1995). Friction damping and isolation systems. *Journal of Vibration and Acoustics*, *117*(50), 196–206. https://doi.org/10.1115/1.2838663

Ferri, A. A., & Bindemann, A. C. (1992). Damping and Vibration of Beams with Various Types of Frictional Support Conditions. *Journal of Vibration and Acoustics*, *114*(3), 289–296. https://doi.org/10.1115/1.2930260

Ferri, A. A., & Dowell, E. H. (1988). Frequency domain solutions to multi-degree-of-freedom, dry friction damped systems. *Journal of Sound and Vibration*, *124*(2), 207–224. https://doi.org/10.1016/S0022-460X(88)80183-4

Ferri, A. A., Heck, B. S., & Development, M. (1998). Vibration Analysis of Dry Friction Damped Turbine Blades Using Singular Perturbation Theory. *Journal of Vibration and Acoustics*, *120*(April 1998), 588–595.

Filippi, S., Akay, A., & Gola, M. M. (2004). Measurement of Tangential Contact Hysteresis During Microslip. *Journal of Tribology*, *126*(3), 482. https://doi.org/10.1115/1.1692030

Griffin, J. H. (1980). Friction Damping of Resonant Stresses in Gas Turbine Engine Airfoils. *Journal of Engineering for Power*, *102*(2), 329–333. https://doi.org/10.1115/1.3230256

Griffin, J. H., & Menq, C.-H. (1991). Friction Damping of Circular Motion and its Implications to Vibration Control. *Journal of Vibration and Acoustics*, *113*(August 1989), 225–229.

He, S., Ren, X., & Qin, W. (2010). A new micro slip for analyzing vibration characteristic of dry friction damper under high normal force. In *ICIC 2010 - 3rd International Conference on Information and Computing* (Vol. 3, pp. 258–261). https://doi.org/10.1109/ICIC.2010.250

Kaiser, A. B., Cusumano, J. P., Gardner, J. F., & Cusumano, J. P. (2002). Modeling and Dynamics of Friction Wedge Dampers in Railroad Freight Trucks. *Vehicle System Dynamics*, *38*, 55–82. https://doi.org/10.1076/vesd.38.1.55.3519

Koh, K.-H. H., Griffin, J. H., Filippi, S., Akay, A., Griffin, J. H., Filippi, S., & Akay, A. (2005). Characterization of turbine blade friction dampers. *Journal of Engineering for Gas Turbines and Power*, *127*(4), 856–862.

https://doi.org/10.1115/1.1926312

Kuran, B., & Özgüven, H. N. (1996). A Modal Superposition Method for Non-Linear Structures. *Journal of Sound and Vibration*, *189*(3), 315–339. https://doi.org/10.1006/jsvi.1996.0022

Lee, Y. B., Kim, T. H., Kim, C. H., Lee, N. S., & Choi, D. H. (2004). Unbalance Response of a Super-Critical Rotor Supported by Foil Bearings — Comparison with Test Results. *Tribology Transactions*, *47*(October), 54–60. https://doi.org/10.1080/05698190490279038

Liao, M., Song, M., & Wang, S. (2014). Active Elastic Support/Dry Friction Damper with Piezoelectric Ceramic Actuator. *Shock and Vibration*, *2014*(4), 1–10. https://doi.org/10.1155/2014/712426

Menq, C.-H., Griffin, J. H., & Bielak, J. (1986). The Influence of a Variable Normal Load on the Forced Vibration of a Frictionally Damped Structure. *Journal of Engineering for Gas Turbines and Power*, *108*(2), 300–305. https://doi.org/10.1115/1.3239903

Menq, C., & Griffin, J. H. (1985). A Comparison of Transient and Steady State Finite Element Analyses of the Forced Response of a Friotionaily Damped Beam. *Journal of Vibration and Acoustics*, *107*(83), 19–25.

Menq, C. H., Chidamparam, P., & Griffin, J. H. (1991). Friction Damping of Two-Dimensional Motion and Its Application in Vibration Control. *Journal of Sound and Vibration*, *144*, 427–447.

Menq, C. H., Griffin, J. H., & Bielak, J. (1986a). The Forced Response of Shrouded Fan Stages. *Journal of Vibration, Acoustics, Stress, and Reliability in Design*, *108*(1), 50–55. https://doi.org/10.1115/1.3269303

Menq, C. H., Griffin, J. H., & Bielak, J. (1986b). The influence of microslip on vibratory response, Part I: A new microslip model. *Journal of Sound and Vibration*, *107*(2), 279–293. https://doi.org/10.1016/0022-460X(86)90239-7

Menq, C. H., Griffin, J. H., & Bielak, J. (1986c). the Influence of Microslip on Vibratory Response , Part II : a Comparison with Experimental Results. *Journal of Sound and Vibration*, *107*, 295–307.

Menq, C. H., & Yang, B. D. (1998). Non-linear spring resistance and friction damping of frictional constraint having two-dimensional motion. *Journal of Sound and Vibration*, *217*(1), 127–143. https://doi.org/10.1006/jsvi.1998.1739

Montagnier, O., & Hochard, C. (2007). Dynamic instability of supercritical driveshafts mounted on dissipative supports — Effects of viscous and hysteretic internal damping. *Journal of Sound and Vibration*, *305*, 378–400. https://doi.org/10.1016/j.jsv.2007.03.061

Montagnier, O., & Hochard, C. (2014). Dynamics of a supercritical composite shaft mounted on viscoelastic supports. *Journal of Sound and Vibration*, *333*(2), 470–484.

Mualla, I. H., & Belev, B. (2002). Performance of steel frames with a new friction damper device under earthquake excitation. *Engineering Structures*, *24*, 365–371.

Ostachowicz, W. M. (1990). A Discrete Linear Beam Model to Investigate the Nonlinear Effects of Slip Friction. *Computers and Structures*, *36*(4), 721–728.

Ozaydin, O., & Cigeroglu, E. (2017). Effect of Dry Friction Damping on the Dynamic Response of Helicopter Tail Shaft. In D. Di Maio & P. Castellini (Eds.), *Proceedings of the 35th IMAC, A Conference and Exposition on Structural Dynamics 2017* (pp. 23–30). Springer.

Peng, B., Zhu, R., Li, M., & Tang, Z. (2017). Bending Vibration Suppression of a Flexible Multispan Shaft Using Smart Spring Support. *Shock and Vibration*, *2017*, 1–12.

Petrov, E. P., & Ewins, D. J. (2003). Analytical formulation of friction interface elements for analysis of nonlinear multi-harmonic vibrations of bladed disks. *Proceedings of ASME TURBOEXPO*, *125*(April), 1–10. https://doi.org/10.1115/1.1539868

Petrov, E. P., & Ewins, D. J. (2004). Generic friction models for time-domain vibration analysis of bladed disks. *Journal of Turbomachinery*, *126*(1), 184–192. https://doi.org/10.1115/1.1644557

Pierre, C., Ferri, a. a., & Dowell, E. H. (1985). Multi-Harmonic Analysis of Dry

Friction Damped Systems Using an Incremental Harmonic Balance Method. *Journal of Applied Mechanics*, *52*(4), 958. https://doi.org/10.1115/1.3169175

Prasue, R. H., Meacham, H. ., & Voorhees, J. E. (1967). The Design and Evaluation of a Supercritical-Speed Helicopter Power-Transmission Shaft. *Journal of Engineering for Industry*, 719–727.

Putignano, C., Ciavarella, M., & Barber, J. R. (2011). Frictional energy dissipation in contact of nominally flat rough surfaces under harmonically varying loads. *Journal of the Mechanics and Physics of Solids*, *59*(12), 2442–2454. https://doi.org/10.1016/j.jmps.2011.09.005

Quinn, D. D., & Segalman, D. J. (2005). Using Series-Series Iwan-Type Models for Understanding Joint Dynamics. *Journal of Applied Mechanics*, *72*(5), 666. https://doi.org/10.1115/1.1978918

Sanliturk, K. Y., & Ewins, D. J. (1996). Modelling Two-Dimensional Friction Contact and Its Application Using Harmonic Balance Method. *Journal of Sound and Vibration*, *193*(2), 511–523. https://doi.org/10.1006/jsvi.1996.0299

Sanliturk, K. Y., Ewins, D. J., & Stanbridge, a. B. (2001). Underplatform Dampers for Turbine Blades: Theoretical Modeling, Analysis, and Comparison With Experimental Data. *Journal of Engineering for Gas Turbines and Power*, *123*(4), 919. https://doi.org/10.1115/1.1385830

Sanliturk, K. Y., Imregun, M., & Ewins, D. J. (1997). Harmonic Balance Vibration Analysis of Turbine Blades With Friction Dampers. *Journal of Vibration and Acoustics*, *119*(1), 96. https://doi.org/10.1115/1.2889693

Siewert, C., Panning, L., Wallaschek, J., & Richter, C. (2009). Multiharmonic forced response analysis of a turbine blading coupled by nonlinear contact forces. In *Proceedings of the ASME Turbo Expo* (Vol. 6). Orlando. https://doi.org/10.1115/GT2009-59201

Sorge, F. (2009). Damping of rotor conical whirl by asymmetric dry friction suspension. *Journal of Sound and Vibration*, *321*, 79–103. https://doi.org/10.1016/j.jsv.2008.09.009

Srinivasan, A. V, & Cutts, D. G. (1983). Dry Friction Damping Mechanisms in

Engine Blades. *Journal of Engineering for Power*, *105*(2), 332–341. https://doi.org/10.1115/1.3227420

Szénási, S., & Tóth, Á. (2015). Solving Multiple Quartic Equations on the GPU using Ferrari's Method. *IEEE 13th International Symposium on Applied Machine Intelligence and Informatics (SAMI2015)*, (7), 333–337. Retrieved from http://users.nik.uni-obuda.hu/sanyo/gpgpu/sami2015_submission_60.pdf

Tabeshpour, M. R., & Ebrahimmian, H. (2010). Seismic Retrofit of Existing Structures Using Friction Dampers. *Asian Journal of Civil Engineering*, *11*(4), 509–520.

Taylor, P., Wu, Q., Cole, C., Spiryagin, M., & Sun, Y. Q. (2014). A review of dynamics modelling of friction wedge suspensions. *Vehicle System Dynamics*. https://doi.org/10.1080/00423114.2014.943249

True, H., & Asmund, R. (2002). The Dynamics of a Railway Freight Wagon Wheelset With Dry Friction Damping. *Vehicle System Dynamics*, *38*, 149–163.

Urroz, G. E. (2004). *Solution of non-linear equations*. http://ocw.usu.edu/Civil_and_Environmental_Engineering/Numerical_Methods_in_Civil_Engineering/NonLinearEquationsMatlab.pdf

Von Groll, G., & Ewins, D. J. (2001). the Harmonic Balance Method With Arc-Length Continuation in Rotor/Stator Contact Problems. *Journal of Sound and Vibration*, *241*(2), 223–233. https://doi.org/10.1006/jsvi.2000.3298

Wang, J. H., & Chen, W. K. (1993). Investigation of the Vibration of a Blade With Friction Damper by HBM. *Journal of Engineering for Gas Turbines and Power*, *115*(2), 294–299. https://doi.org/10.1115/1.2906708

Whiteman, W. E., & Ferri, A. A. (1996). Displacement-Dependent Dry Friction Damping of a Beam-Like Structure. *Journal of Sound and Vibration*, *198*, 313–329. https://doi.org/10.1006/jsvi.1996.0572

Yang, B., Chu, M., & Menq, C. (1998). Stick–slip–separation analysis and non-linear stiffness and damping characterization of friction contacts having

variable normal load. *Journal of Sound and Vibration*, *210*, 461–481. https://doi.org/10.1006/jsvi.1997.1305

Yang, B. D., & Menq, C.-H. (1998a). Characterization of 3D contact kinematics and prediction of resonant response of structures having 3D frictional constraint. *Journal of Sound and Vibration*, *217*(5), 909–925. https://doi.org/10.1006/jsvi.1998.1802

Yang, B. D., & Menq, C. H. (1998b). Characterization of Contact Kinematics and Application to the Design of Wedge Dampers in Turbomachinery Blading: Part 1—Stick-Slip Contact Kinematics. *Journal of Engineering for Gas Turbines and Power*, *120*(April 1998), 410–417.

Yang, B. D., & Menq, C. H. (1998c). Characterization of Contact Kinematics and Application to the Design of Wedge Dampers in Turbomachinery Blading: Part 2—Prediction of Forced Response and Experimental Verification. *Journal of Engineering for Gas Turbines and Power*, *120*(2), 418. https://doi.org/10.1115/1.2818139

Zucca, S., Firrone, C. M., & Gola, M. (2012). Modeling underplatform dampers for turbine blades: a refined approach in the frequency domain. *Journal of Vibration and Control*, *19*(7), 1087–1102. https://doi.org/10.1177/1077546312440809

APPENDIX A

QUARTIC EQUATION SOLVER

In order to solve the quartic equations, solution of the Lodovico Ferrari who is known as the first person solving the quartic equations is used (Szénási & Tóth, 2015) .

$$Ax^4 + Bx^3 + Cx^2 + Dx + E = 0 \tag{A.1}$$

$$\alpha = -\frac{3B^2}{8A^2} + \frac{C}{A} \tag{A.2}$$

$$\beta = \frac{B^3}{8A^3} - \frac{BC}{2A^2} + \frac{D}{A} \tag{A.3}$$

$$\gamma = -\frac{3B^4}{256A^4} + \frac{CB^2}{16A^3} - \frac{BD}{4A^2} + \frac{E}{A} \tag{A.4}$$

if $\beta = 0$

$$x = -\frac{B}{4A} \pm \sqrt{\frac{-\alpha \pm \sqrt{\alpha^2 - 4\gamma}}{2}} \tag{A.5}$$

if $\beta \neq 0$

$$P = -\frac{\alpha^2}{12} - \gamma \tag{A.6}$$

$$Q = -\frac{\alpha^3}{108} + \frac{\alpha\gamma}{3} - \frac{\beta^2}{8} \tag{A.7}$$

$$R = -\frac{Q}{2} \pm \sqrt{\frac{Q^2}{4} + \frac{P^3}{27}} \tag{A.8}$$

$$U = \sqrt[3]{R} \tag{A.9}$$

$$y = \begin{cases} -\frac{5}{6}\alpha + U - \frac{P}{3U} \text{ if } U \neq 0 \\ -\frac{5}{6}\alpha + U - \sqrt[3]{Q} \text{ if } U = 0 \end{cases} \tag{A.10}$$

$$W = \sqrt{\alpha + 2y} \tag{A.11}$$

$$x = -\frac{B}{4A} + \frac{\pm W \mp \sqrt{-(3\alpha + 2y \pm \frac{2\beta}{W})}}{2} \tag{A.12}$$

APPENDIX B

PUBLISHED PAPERS

Effect of Dry Friction Damping on the Dynamic Response of Helicopter Tail Shaft*

Onur Ozaydin[a, b]

Ender Cigeroglu, Assoc. Prof. Dr. [a, †]

[a] *Department of Mechanical Engineering, Middle East Technical University, Universiteler Mahallesi, Dumlupinar Bulvari No:1 06800 Cankaya-Ankara / Turkey*

[b] *Turkish Aerospace Industries, Inc. (TAI), Fethiye Mahallesi Havacilik Bulvari No:17 06980 Kazan-Ankara/Turkey*

† *Corresponding Author*

ABSTRACT

Tail Drive Shaft of a helicopter transmits torque from the main gear box to the tail rotor and in most of the helicopter designs, tail shafts are designed to work in supercritical speeds. In order to limit resonance vibrations of the tail drive shaft, dry friction dampers can be used. Therefore, in order to study the effect of dry friction damping on the response of tail shaft drive, a mathematical model is developed. The tail drive shaft is modeled as a beam by using Euler-Bernoulli beam theory. Bearings supporting the shaft structure and couplings used are represented by linear and torsional springs, respectively. The dry friction damper is located at the middle section of the shaft which is modeled by using a one-dimensional macroslip friction model with constant normal load. The partial differential equation of motion obtained is discretized by using Galerkin's Method with multiple trial functions. The resulting nonlinear ordinary differential equations are converted into a set of nonlinear algebraic equations by using harmonic balance method utilizing single harmonic. Finally, the solution of the resulting set of nonlinear algebraic equations are obtained by using Newton's method. Using the model developed effects of parameters of the friction damper on the response of the tail drive shaft are studied.

Keywords

Helicopter tail drive shaft, Dry friction damper, Macroslip friction, Nonlinear vibrations, Harmonic balance method, Euler-Bernoulli beam theory

1. Introduction

Dynamics of the tail drive shaft of a helicopter is an important problem since excessive vibrations may result in a catastrophic failure. In the literature, there exits two different designs for tail drive shafts: subcritical design (operating below the first natural frequency) and supercritical design (operating above the first natural frequency). Using minimum number of long shafts working at supercritical speed is more advantageous than using many short shafts working at subcritical speed. On the other hand, in the supercritical design, in order to reach to the operating speed, shafts should pass through the resonance region where excessive vibrations can be observed which can be avoided by using proper dampers [1].

*Ozaydin O., Cigeroglu E. (2017) Effect of Dry Friction Damping on the Dynamic Response of Helicopter Tail Shaft. In: Di Maio D., Castellini P. (eds) Rotating Machinery, Hybrid Test Methods, Vibro-Acoustics & Laser Vibrometry, Volume 8. Conference Proceedings of the Society for Experimental Mechanics Series. Springer, Cham

Dry friction dampers are widely used in different applications such as turbomachinery [2], turbine or compressor blades [3, 4], buildings under seismic excitation [5, 6], and railway bogies [7] to reduce resonant vibrations. In this paper, a continuous dynamic model of a tail drive shaft of a helicopter with dry friction damper is developed. In order to discretize the partial differential equation of motion, Galerkin's Method with multiple trial functions is used. Due to the nonlinear behavior of dry friction, it is complicated to model and analyze systems including dry friction. In the literature, Harmonic Balance Method (HBM), a frequency domain solution method, is widely used instead of direct time integration, which requires high computational effort and computation time [8]. Therefore, in this study, HBM is used to convert the resulting nonlinear ordinary differential equations into a set of nonlinear algebraic equations. The resulting equations are solved by using Newton's method. Several case studies are performed in order to investigate the effects of dry friction damper on the response of tail drive shaft system.

2. Mathematical Model of the System

The tail drive shaft system shown in Fig. 1 consists of a shaft supported by two bearings at both ends and connected to two couplings. A dry friction damper is used in the middle of the shaft in order to decrease vibration amplitudes. The tail drive shaft is modeled by Euler-Bernoulli Beam theory and spring elements are used to represent the bearings and couplings as shown in Fig. 2. Equation of motion of an Euler Bernoulli beam can be written as follows

$$\rho A\frac{\partial^2 w(x,t)}{\partial t^2}+EI\frac{\partial^4 w(x,t)}{\partial y^4}+c\frac{\partial w(x,t)}{\partial t}=f(t)\delta(x-L_2)-f_n(w(x,t))\delta(x-L_1), \tag{1}$$

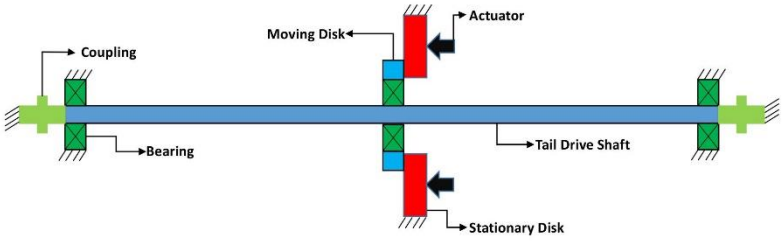

Fig. 1 Tail Drive Line

where $w(x,t)$ is transverse displacement, ρ is density, A is cross sectional area, E is Young's Modulus, I is moment of inertia, c is viscous damping coefficient, $f_n(w(x,t))$ is the nonlinear friction force , $f(t)$ is external forcing, L_1 is the location of dry friction damper and L_2 is location of external forcing.

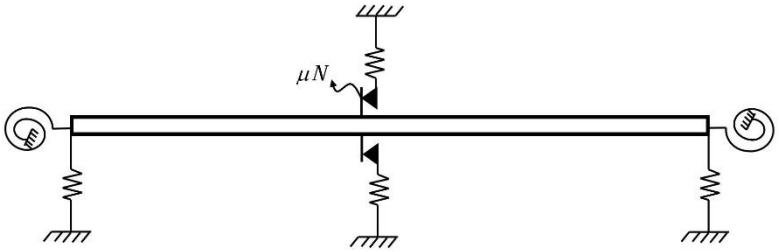

Fig. 2 Dynamic Model of Tail Drive Line

3. Solution Methodology

For the solution of the partial differential equation of motion given in Eq.(1) Galerkin's method is used. Utilizing expansion theorem transverse displacement of the shaft can be expressed as given below;

$$w(x,t) = \sum_j a_j(t)\phi_j(x), \tag{2}$$

where $a_j(t)$ and $\phi_j(x)$ are the j^{th} generalized coordinate and mass normalized eigenfunction of a beam with springs at the supports are included. Substituting Eq.(2) into Eq.(1) the following result is obtained.

$$\begin{aligned}&\rho A\sum_j \frac{d^2 a_j(t)}{dt^2}\phi_j(x) + EI\sum_j a_j(t)\frac{d^4\phi_j(x)}{dx^4} + c\sum_j \frac{da_j(t)}{dt}\phi_j(x) + f_n(t)\delta(x-L_1)\\ &= f(t)\delta(x-L_2)\end{aligned}. \tag{3}$$

Multiplying both side of Eq.(3) by $\phi_i(x)$ and integrating over the spatial domain, the following result is obtained

$$[I]\{\ddot{a}\} + [C_r]\{\dot{a}\} + [\Omega]\{a\} + \{F_n(\{a\})\} = \{F(t)\}. \tag{4}$$

Since mass normalized eigenfunctions are used in the expansion, $[I]$, $[C_r]$, $[\Omega]$, $\{F_n\}$ and $\{F\}$ are identity matrix, diagonal damping matrix, diagonal matrix of squares of natural frequencies, nonlinear modal forcing vector and external modal forcing vector, respectively. Elements of these matrices and vectors can be calculated as follows

$$\Omega_{ii} = \omega_i^2 = \int_0^L EI\frac{d^4\phi_i(x)}{dx^4}\phi_i(x)\,dx, \tag{5}$$

$$C_{r_{ii}} = \int_0^L c\phi_i(x)^2\,dx = 2\zeta_i\omega_i, \tag{6}$$

$$F_{n_i}(t) = f_n(t)\phi_i(L_1), \tag{7}$$

$$F_i(t) = f(t)\phi_i(L_2), \tag{8}$$

where ω_i and ζ_i are the natural frequency and damping ratio of the i^{th} mode.

4. Harmonic Balance Method

The nonlinear ordinary differential equation set defined by Eq.(4) is converted into a set of nonlinear algebraic equations by using Harmonic Balance Method. For this purpose, by using a single harmonic representation, generalized coordinate can be expressed as follows

$$\{a\} = \{a_s\}\sin(\omega t) + \{a_c\}\cos(\omega t), \tag{9}$$

where $a_{js}(t)$ and $a_{jc}(t)$ are the sine and cosine components of the j^{th} generalized coordinate. Similarly, utilizing Fourier series, nonlinear forcing and external excitation force vectors can be written as

$$\{F_n(t)\} = \{F_{ns}\}\sin(\omega t) + \{F_{nc}\}\cos(\omega t), \tag{10}$$

$$\{F(t)\} = \{F_s\}\sin(\omega t) + \{F_c\}\cos(\omega t) \tag{11}$$

where $\{F_{ns}\}$ and $\{F_{nc}\}$ are the sine and cosine components of the nonlinear internal forcing vector and $\{F_s\}$ and $\{F_c\}$ are the sine and cosine components of external forcing vector. After inserting Eq.(9)-(11) into Eq.(4) and separating sine and cosine components, the following nonlinear algebraic equations are obtained

$$\begin{bmatrix} [\Omega]-\omega^2[I] & 0 \\ 0 & [\Omega]-\omega^2[I] \end{bmatrix}\begin{Bmatrix} a_s \\ a_c \end{Bmatrix} + \begin{bmatrix} 0 & -\omega[C_r] \\ \omega[C_r] & 0 \end{bmatrix}\begin{Bmatrix} a_s \\ a_c \end{Bmatrix} + \begin{Bmatrix} F_{ns} \\ F_{nc} \end{Bmatrix} = \begin{Bmatrix} F_s \\ F_c \end{Bmatrix}, \tag{12}$$

Eq.(12) is a set of nonlinear algebraic equations, which can be solved by a nonlinear equation solver such as Newton's method.

Dry friction can be modeled in several different ways in dynamic analysis of systems. In this study, one dimensional macrolsip friction model [3, 9], shown in Fig. 3, is used. Here, k_d is the tangential contact stiffness, N is the normal load, μ is coefficient of friction, $u(t)$ is the tangential input motion and $v(t)$ is the slip motion. Fig. 4 shows the hysteresis curve for the friction element given in Fig. 3 for single harmonic motion.

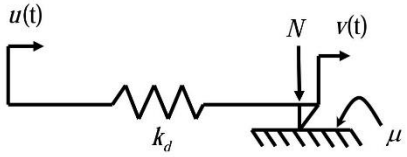

Fig. 3 Dry friction element

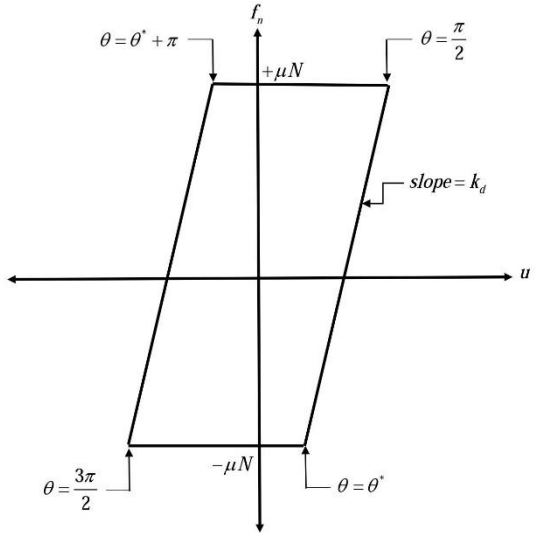

Fig. 4 Hysteresis curve for single harmonic motion

Hysteresis curve given in Fig. 4 can be defined as follows

$$f_n = \begin{cases} k_d\left(A\sin(\theta) - A\right) + \mu N \text{ when } \dfrac{\pi}{2} \le \theta \le \theta^* \\ -\mu N \text{ when } \theta^* \le \theta \le \dfrac{3\pi}{2} \\ k_d\left(A\sin(\theta) + A\right) - \mu N \text{ when } \dfrac{3\pi}{2} \le \theta \le \theta^* + \pi \\ \mu N \text{ when } \theta^* + \pi \le \theta \le \dfrac{5\pi}{2} \end{cases}, \tag{13}$$

$$\theta^* = \pi - a\sin\left(1 - \frac{2\mu N}{k_d A}\right) \tag{14}$$

where A is the amplitude of harmonic tangential motion and $\theta = \omega t$. The nonlinear dry friction force can be represented by using a single harmonic as

$$f_n(t) = f_{ns}\sin(\theta) + f_{nc}\cos(\theta), \tag{15}$$

$$f_{ns} = \frac{2}{\pi}\int_{\frac{\pi}{2}}^{\frac{3\pi}{2}} f_n(t)\sin(\theta)\, d\theta, \tag{16}$$

$$f_{nc} = \frac{2}{\pi}\int_{\frac{\pi}{2}}^{\frac{3\pi}{2}} f_n(t)\cos(\theta)\,d\theta\,, \tag{17}$$

where the sine and cosine components are given in [5] as follows

$$f_{ns} = \left(-\frac{4\mu N}{\pi} + \frac{2Ak_d}{\pi}\right)\cos(\theta^*) - \frac{Ak_d}{2\pi}\sin(2\theta^*) + \frac{Ak_d}{\pi}\theta^* - \frac{Ak_d}{2}, \tag{18}$$

$$f_{nc} = \left(\frac{4\mu N - 2Ak_d}{\pi}\right)\sin(\theta^*) + \frac{Ak_d}{\pi}\sin(\theta^*)^2 + \frac{Ak_d}{\pi}\,. \tag{19}$$

5. Case Studies

The parameters of an example helicopter tail shaft assembly with a dry friction damper are given in Table 1. Dry friction damper is characterized by two factors namely; slip force μN, contact stiffness k_d.

Table 1 Parameters of the example system

Parameter	**Numerical Value**
L [m]	3
D_o [m]	0.09
D_i [m]	0.07
E [GPa]	68.9
ρ [kg/m^3]	2700
k [N/m]	10^6
k_t [Nm/rad]	10^8
k_d [N/m]	10^6
ζ	0.02
F [N]	$60\sin(\omega t)$

where L, D_o and D_i are length, outer diameter and inner diameter of the tail drive shaft, respectively.

In the first case study given, dry friction damper is located at the midpoint of the shaft and effect of slip force, μN, on the maximum vibration amplitude of the shaft around its first critical speed is investigated. Displacement amplitude of the tail drive shaft obtained at the midpoint are given in Fig. 5 for an external forcing applied at the same point. It is observed from the results that increasing slip load decreases the vibration amplitude until a certain point where further increase in the slip force results in an increase in the maximum vibration amplitude. Moreover, as the slip load increases, resonance frequency of the tail drive shaft system also increases which is due to the increased stiffness effect of the dry friction damper. For a slip load of 3840 N, friction damper becomes fully stuck and behaves like a linear spring element. From these results, it can be concluded that there is an optimum slip load which minimizes the vibration amplitude. In the next study given, in order to see the effect of damper location on the system response, system given in previous case study with different damper locations are studied. Maximum vibration amplitude normalized with respect to the maximum vibration amplitude of the no damper case is given in Fig. 6. It is clearly seen that the optimum damper location for the first vibration mode is the midpoint of the shaft where the highest amplitude is seen.

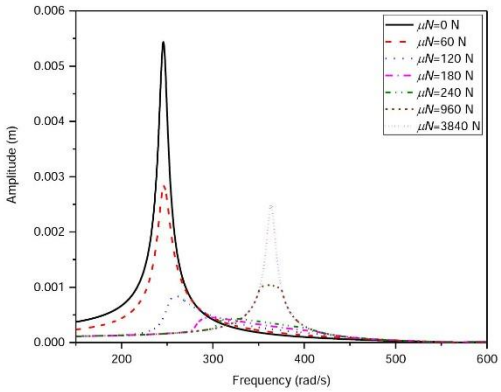

Fig. 5 Effect of slip force (μN) on the peak amplitude ($L_1 = 0.5L$ and $L_2 = 0.5L$)

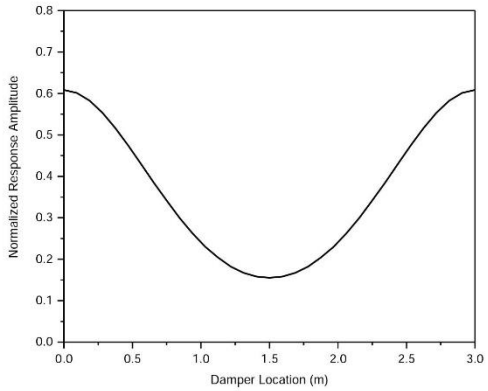

Fig. 6 Effect of damper location on the maximum vibration amplitude ($\mu N = 120$, $L_2 = 0.5L$)

In the next two case studies, external force is applied at $0.25L$ and results are taken from that point. In the first case study presented in Fig. 7, damper is located at the midpoint and it is seen that although the damper is able to damp vibrations around the first mode, it is ineffective around the second mode. This is due the fact that the damper is located on the nodal point for the second mode. In the second case study, damper location is moved to $0.25L$ the results obtained are given in Fig. 8. It is observed from these results that in this case, in addition to the first mode, vibrations around the second mode are as well damped out. - It can be concluded that if more than one mode is required to be damped, optimum damper location should be sought and nodal points should be avoided.

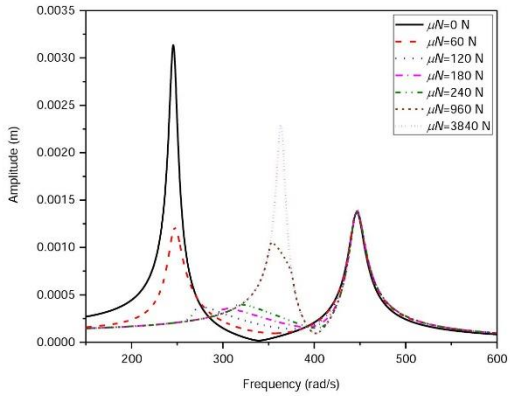

Fig. 7 Effect of slip force (μN) on the peak amplitude ($L_1 = 0.5L$ and $L_2 = 0.25L$)

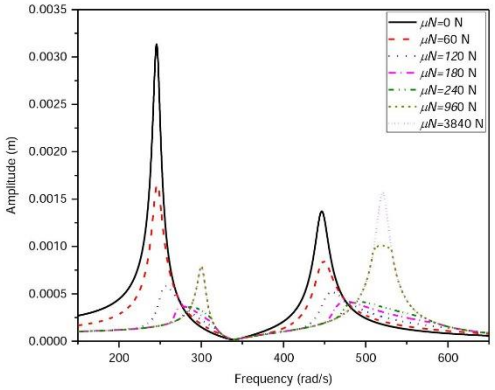

Fig. 8 Effect of slip force (μN) on the peak amplitude ($L_1 = 0.25L$ and $L_2 = 0.25L$)

In the final case study, while holding the slip force as constant at the optimal value, amplitude of the external force is varied. External forcing is applied at the midpoint and displacement amplitude of the shaft at the same point is considered. For this case, optimum slip force is determined to be 240N for 60N external force. Maximum vibration amplitude normalized with respect to the maximum vibration amplitude of the corresponding linear case is plotted in Fig. 9 as a function of percent external forcing amplitude. It can observed that, effectiveness of the damper depends on the accurate estimation of the amplitude of external forcing.

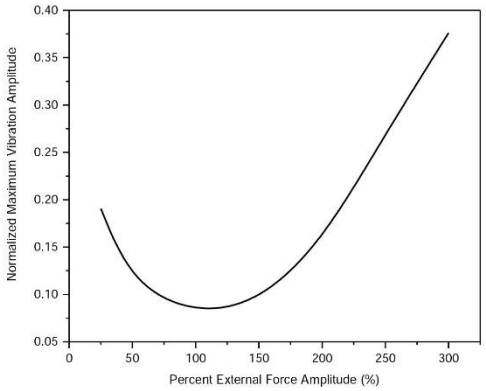

Fig. 9 Effect of amplitude variation of external forcing ($\mu N = 240\text{N}$, $L_1 = 0.5L$, $L_2 = 0.5L$)

6. Conclusion

In this study, effect of dry friction damping on vibration attenuation of helicopter tail shaft is studied. The tail drive shaft is modeled by Euler-Bernoulli model supported by springs which represent the bearings and couplings used. The partial differential equation of motion obtained is discretized by using Galerkin's Method and the resulting nonlinear ordinary differential equations are converted into a set of nonlinear algebraic equations by using Harmonic Balance Method. In order to model the dry friction damper one dimensional macroslip friction model with constant normal load is used. it is observed from the results obtained that dry friction dampers can be used to suppress excessive vibrations when the shaft is rotating around its critical speed. The amount of the slip load and the location of the friction damper are the two important parameters affecting the performance of the friction damper. Depending on the number of critical speeds to be considered in the vibration reduction an optimum damper location needs to be determined in addition to the slip force. However, in case of a single critical speed, location of the maximum vibration amplitude of is the best place for the friction damper. Moreover, since the performance of the friction damper decreases as the excitation amplitude varies, it is also important to accurately estimate the amplitude of the external forcing.

References

[1] Prause, R. H., Meacham, H. C., & Voorhees J. E., 1967, "The Design and Evaluation of a Supercritical-Speed Helicopter Power-Transmission Shaft," Journal of Engineering for Industry, *89*, pp. 719-727.
[2] Childs, D. W., & Bhattacharya, A., 2007, "Prediction of Dry-Friction Whirl and Whip between a Rotor and a Stator," Journal of Vibration and Acoustics, *129*, pp. 355-362.
[3] Wang, J. H., & Chen, W. K., 1993, "Investigation of the Vibration of a Blade with Friction Damper by HBM," Journal of Engineering for Gas Turbines and Power, *115*, pp. 294-299.
[4] Pust, L., Pesek, L., Radolfova, A., 2015, "Blade couple with dry friction connection," Applied and Computational Mechanics, 9, pp. 31-40.
[5] Erisen, Z.E, Cigeroglu, E., 2012, "Frequency Domain Optimization of Dry Friction Dampers on Buildings Under Harmonic Excitation," IMAC XXX: Conference & Exposition on Structural Dynamics, January 30-February 02, 2012, Jacksonville, Florida, USA.

[6] Belash, T., 2015, "Dry friction dampers in quake-proof structures of buildings," Procedia Engineering, *117*, 397-403
[7] True, H., Asmund, R., 2003, "The dynamics of a railway freight wagon wheelset with dry friction damping," Vehicle System Dynamics, 38, pp. 149-13.
[8] Mingfu, L., Mingbo, S., & Wang, S., 2014, "Active Elastic Support/ Dry Friction Damper with Piezoelectric Ceramic Actuator," Shock and Vibration, *2014*, pp. 1-10.
[9] Ciğcroğlu, E., & Özgüvcn, N., 2006, "Nonlinear Vibration Analysis of Bladed Disks with Dry Friction Dampers," Journal of Sound and Vibration, *295*, pp. 1028-1043.